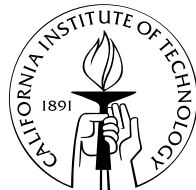


Modeling, Simulation, and Control of Cavity Flow Oscillations

Thesis by
Clarence W. Rowley

Technical Report
for the
Department of Mechanical Engineering



California Institute of Technology
Pasadena, California

2002

(Thesis defended August 8, 2001)

Acknowledgements

I cannot heap enough praise on my two advisors, Tim Colonius and Richard Murray, who have contributed immeasurably both to this thesis and to my overall happiness at Caltech these past years. I also thank Jerry Marsden, who has served almost as a third advisor to me, and Tony Leonard, for serving on my thesis committee and for offering many helpful comments. Doug MacMartin helped with the linear modeling and control design, and Dave Williams and Drazen Fabris generously allowed me to participate in their experiments.

In the course of my studies, it was my great pleasure to return to Princeton University for two months and work with Phil Holmes and Yannis Kevrekidis, who offered their great insight into modeling and model reduction. I would also like to thank Gigi Martinelli for generously sharing his time, his flow solver, and his expertise, and Troy Smith for generously sharing his office and its furnishings.

Countless other friends have made the past few years absolutely delightful. My hiking partner Chris Brennen has become like a father to me, and I cannot thank him enough for the many adventures we have enjoyed together. Allan Acosta shared several wonderful weekends on his boat, which I will always remember. The many friends and colleagues who have helped me out are too numerous to mention, but I must especially thank my dear friends Jeff Eldredge and Martha Gallivan.

This thesis is dedicated to my mother, for her constant love and support.

Abstract

This thesis involves the modeling of self-sustained oscillations in the flow past a rectangular cavity. The emphasis is on developing low-dimensional models that are suitable for analysis using tools from dynamical systems and control theory.

Two-dimensional direct numerical simulations are performed, and indicate the presence of a “wake mode,” which has been observed previously in experiments, but which is much less well understood than the “shear-layer mode” usually observed. We characterize the flow in both shear-layer mode and wake mode, and provide a criterion for predicting the onset of wake mode, as a function of the various geometrical and flow-related parameters.

We focus on the modeling of shear-layer mode, and employ two distinct modeling approaches: first, we use the method of Proper Orthogonal Decomposition (POD) and Galerkin projection to reduce the Navier-Stokes equations to a low-dimensional system of ordinary differential equations (ODEs). We extend the method to compressible flows, using approximations that are valid for cold flows at moderate Mach number. In a compressible flow, both the kinematic and thermodynamic variables contribute to the total energy, and an inner product is introduced which respects this, and allows one to use vector-valued POD modes for the Galerkin projection. We obtain models in the form of ODEs with between 2 and 60 states, and compare models based on scalar-valued and vector-valued POD modes. All of the models work well for short times (a few periods of oscillation), but the models based on scalar-valued modes deviate for longer times, while in general the models based on vector-valued modes retain qualitatively correct dynamical behavior.

In the second modeling approach, we model the underlying physical mechanisms separately (shear-layer amplification, acoustic scattering, acoustic propagation), and obtain linear models that are suitable for control design and analysis. We design a controller which stabilizes the model, and implement a similar control law on an experiment, demonstrating significant reduction in the amplitude of the oscillations, but revealing some limitations of feedback control.

Contents

| | | |
|----------|--|-----------|
| 1 | Introduction | 1 |
| 1.1 | Motivation | 1 |
| 1.2 | Historical perspective | 2 |
| 1.2.1 | Cavity oscillations | 2 |
| 1.2.2 | Model reduction | 3 |
| 1.3 | Overview of contributions | 4 |
| 2 | Linear Stability of Parallel Shear Flows | 7 |
| 2.1 | Equations of motion | 7 |
| 2.2 | Mean profiles and boundary conditions | 9 |
| 2.3 | Method of solution: spatial vs. temporal | 10 |
| 2.4 | Number of unstable eigenvalues | 12 |
| 2.5 | Singularity at the critical layer | 13 |
| 2.6 | Adjoint equations | 15 |
| 2.7 | Biorthogonality relation | 16 |
| 3 | Physics of Cavity Oscillations | 19 |
| 3.1 | Numerical method | 19 |
| 3.1.1 | Equations of motion | 20 |
| 3.1.2 | Numerical scheme | 21 |
| 3.1.3 | Validation | 22 |
| 3.2 | Shear-layer mode | 24 |
| 3.2.1 | Acoustic field | 25 |
| 3.2.2 | Frequencies of oscillation | 28 |
| 3.2.3 | Shear-layer spreading rate | 31 |
| 3.2.4 | Convection and amplification by the shear layer | 33 |
| 3.3 | Wake mode | 37 |
| 3.3.1 | Flow features | 37 |
| 3.3.2 | Frequency of vortex shedding | 41 |
| 3.3.3 | Parametric dependence of the transition to wake mode | 41 |
| 3.3.4 | Convective and absolute instability | 42 |
| 3.4 | Prediction of the oscillation regimes | 44 |
| 3.4.1 | The role of nonlinearities | 45 |
| 3.4.2 | Shear layer | 49 |
| 3.4.3 | Scattering | 49 |

| | | |
|----------|---|------------|
| 3.4.4 | Loop gain | 50 |
| 3.4.5 | Parametric dependence | 51 |
| 3.5 | Concluding remarks | 53 |
| 4 | Model Reduction for Fluids | 55 |
| 4.1 | Proper Orthogonal Decomposition | 55 |
| 4.1.1 | The main theorem | 55 |
| 4.1.2 | Properties of the POD | 59 |
| 4.1.3 | Computation: method of snapshots | 60 |
| 4.1.4 | Affine subspaces | 61 |
| 4.2 | Galerkin projection | 62 |
| 4.2.1 | Example: Quadratic equations | 63 |
| 4.3 | Incompressible fluids | 64 |
| 4.4 | Compressible fluids | 66 |
| 4.4.1 | Governing equations | 66 |
| 4.4.2 | Scalar-valued POD modes | 68 |
| 4.4.3 | Inner products for compressible flow | 70 |
| 4.4.4 | Vector-valued POD modes | 72 |
| 5 | Low-order Models of Cavity Oscillations | 75 |
| 5.1 | Scalar-valued modes | 75 |
| 5.1.1 | POD modes | 76 |
| 5.1.2 | Galerkin models | 86 |
| 5.2 | Vector-valued modes | 88 |
| 5.2.1 | POD modes | 91 |
| 5.2.2 | Galerkin models | 93 |
| 5.2.3 | Parameter variation | 99 |
| 5.3 | Conclusions | 102 |
| 6 | Control Design and Experimental Results | 105 |
| 6.1 | Experimental setup | 105 |
| 6.1.1 | Sensors | 107 |
| 6.1.2 | Actuator | 107 |
| 6.1.3 | Control implementation | 108 |
| 6.2 | Linear model | 108 |
| 6.2.1 | Shear layer | 110 |
| 6.2.2 | Acoustics | 110 |
| 6.2.3 | Scattering and Receptivity | 112 |
| 6.2.4 | Overall cavity model | 113 |
| 6.3 | Control design | 114 |
| 6.3.1 | LQG design | 114 |
| 6.3.2 | Stabilizing controller for the cavity model | 115 |
| 6.4 | Experimental results | 116 |
| 6.4.1 | Analog controller | 116 |
| 6.4.2 | Digital controller | 117 |

| | | |
|----------|-----------------------------|------------|
| 6.4.3 | Performance limitations | 120 |
| 7 | Conclusions | 123 |
| 7.1 | Summary | 123 |
| 7.2 | Suggestions for future work | 124 |

List of Figures

| | | |
|------|---|----|
| 1.1 | Basic configuration of a cavity flow. | 1 |
| 2.1 | Branch points of solution of the Rayleigh equation. | 14 |
| 2.2 | Domain of the tanh velocity profile. | 14 |
| 3.1 | Schematic diagram of cavity configuration and computational domain. | 22 |
| 3.2 | Validation of boundary position, grid resolution, run L4. | 24 |
| 3.3 | Validation of boundary placement, run L2. | 25 |
| 3.4 | Vorticity contours in shear-layer mode. | 26 |
| 3.5 | Comparison of simulation results with schlieren photographs. | 27 |
| 3.6 | Sound pressure level (SPL) for run L2. | 28 |
| 3.7 | Discrete Fourier Transform of density, run L2. | 29 |
| 3.8 | Spectrum of normal velocity, run 2M7. | 30 |
| 3.9 | Frequencies of oscillation, vs. Mach number. | 31 |
| 3.10 | Vorticity thickness along the shear layer. | 32 |
| 3.11 | Mean streamwise velocity profiles. | 33 |
| 3.12 | Comparison of DFT with linear stability, run L2. | 35 |
| 3.13 | Phase of vortical and acoustic disturbances, run L2. | 36 |
| 3.14 | Amplitude of normal velocity fluctuations, run L2. | 37 |
| 3.15 | Vorticity contours in wake mode. | 38 |
| 3.16 | Time traces of normal velocity, runs L1–L5. | 39 |
| 3.17 | Streamlines and C_p for mean flow, runs L2 and L4. | 39 |
| 3.18 | Mean streamwise velocity profiles, runs L2 and L4. | 40 |
| 3.19 | Instantaneous vorticity contours, run TK4b. | 42 |
| 3.20 | Simple model of nonlinearities. | 45 |
| 3.21 | Describing function for saturation nonlinearity. | 48 |
| 3.22 | Correlation of β with mode of oscillations. | 51 |
| 3.23 | Shear-layer amplification vs. L/θ_0 , varying D/θ_0 | 52 |
| 3.24 | Shear-layer amplification vs. L/θ_0 , varying M | 53 |
| 5.1 | Snapshots used for scalar-valued POD. | 77 |
| 5.2 | Eigenvalues of scalar-valued POD, run L2. | 77 |
| 5.3 | Mean from run L2. | 79 |
| 5.4 | Scalar-valued POD mode 1, run L2. | 80 |
| 5.5 | Scalar-valued POD mode 2, run L2. | 81 |
| 5.6 | Scalar-valued POD mode 3, run L2. | 81 |

| | | |
|------|---|-----|
| 5.7 | Scalar-valued POD mode 4, run L2. | 82 |
| 5.8 | Eigenvalues of scalar-valued POD, run H2. | 82 |
| 5.9 | Mean from run H2. | 83 |
| 5.10 | Scalar-valued POD mode 1, run H2. | 84 |
| 5.11 | Scalar-valued POD mode 2, run H2. | 84 |
| 5.12 | Scalar-valued POD mode 3, run H2. | 85 |
| 5.13 | Scalar-valued POD mode 4, run H2. | 85 |
| 5.14 | Comparison of POD modes from runs H2 and TK4b. | 86 |
| 5.15 | Comparison of linear stability, DFT, and POD modes | 87 |
| 5.16 | Galerkin simulation, scalar-valued modes, short time | 89 |
| 5.17 | Galerkin simulation, scalar-valued modes, long time | 90 |
| 5.18 | Galerkin simulation, scalar-valued modes, with and without viscosity | 91 |
| 5.19 | Snapshots used for vector-valued POD. | 92 |
| 5.20 | Eigenvalues of vector-valued POD, run H2. | 93 |
| 5.21 | Vector-valued POD modes: snapshots from fully developed flow. | 94 |
| 5.22 | Vector-valued POD modes: snapshots from transient region. | 95 |
| 5.23 | Galerkin simulation, fully-developed modes, time 70,000. | 96 |
| 5.24 | Galerkin simulation, fully-developed modes, time 0. | 97 |
| 5.25 | Galerkin simulation, varying α in inner product. | 98 |
| 5.26 | Galerkin simulation, transient modes, time 70,000. | 100 |
| 5.27 | Galerkin simulation, transient modes, time 0. | 101 |
| 5.28 | Eigenvalues of linearized Galerkin model, as M varies. | 102 |
| 5.29 | Frequencies predicted by Galerkin model, as M varies. | 103 |
| 6.1 | Photograph of cavity, from downstream and above. | 106 |
| 6.2 | Photograph of cavity assembly from outside wind tunnel. | 106 |
| 6.3 | Diagram of experimental apparatus. | 107 |
| 6.4 | Block diagram of cavity model. | 109 |
| 6.5 | Block diagram of cavity model with disturbances. | 109 |
| 6.6 | Velocity profiles for the cavity shear layer. | 110 |
| 6.7 | Bode plot of shear layer transfer function $G(s)$ | 111 |
| 6.8 | Block diagram of transfer function $A(s)$ for cavity acoustics. | 111 |
| 6.9 | Frequency response of acoustic transfer function, $M = 0.6$ | 112 |
| 6.10 | Poles and zeros of cavity transfer function $P(s)$ | 114 |
| 6.11 | Bode plot of controller transfer function $C(s)$ | 116 |
| 6.12 | Poles and zeros of closed-loop transfer function. | 117 |
| 6.13 | Bode plot of analog controller. | 118 |
| 6.14 | Power spectra with analog controller. | 118 |
| 6.15 | Bode plot of filters used in digital controllers. | 119 |
| 6.16 | Power spectra with different digital filters. | 120 |
| 6.17 | Power spectra with digital controllers, showing sidebands. | 120 |

List of Tables

| | | |
|-----|---|-----|
| 3.1 | Parameters for the different computer runs. | 23 |
| 5.1 | Snapshots used for scalar-valued POD. | 76 |
| 5.2 | Fraction of energy captured by each POD mode, run L2. | 78 |
| 5.3 | Fraction of energy captured by each POD mode, run H2. | 79 |
| 6.1 | Parameters of digital Butterworth filters used. | 117 |

Chapter 1

Introduction

1.1 Motivation

Self-sustained oscillations occur in a wide variety of applications, from the flow past a sunroof in an automobile, to landing gear wells and weapons bays in aircraft, to musical instruments such as flutes and organ pipes. In all of these flows, acoustics play an important role: sometimes the acoustic radiation is desirable, as in a musical instrument, but in most engineering applications, sound production is undesirable, as in the car sunroof, or aircraft applications, where pressure fluctuations can be so intense that they can lead to fatigue and structural failure of the aircraft. Furthermore, acoustics often play an integral role in the physical mechanisms underlying self-sustained oscillations. This is the case for the cavity flows we study here.

The basic configuration of a cavity flow is shown in figure 1.1. The main features of this flow are the formation of a shear layer, which amplifies flow disturbances, and the subsequent scattering of these disturbances into acoustic waves at the downstream corner. These acoustic waves propagate upstream, and excite further disturbances in the shear layer, creating a feedback loop, which often leads to self-sustained oscillations at discrete resonant frequencies.

In the incompressible limit, a similar mechanism exists, but instead of producing acoustic waves, vortical disturbances moving past the downstream corner produce an irrotational field which excites further shear layer disturbances. This irrotational field is analogous to the acoustic field generated at higher Mach numbers, only the propagation speed is effectively infinite.

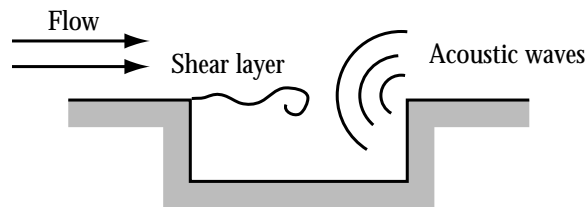


Figure 1.1: Basic configuration of a cavity flow.

The focus of this thesis is to develop tractable dynamical models of these phenomena, motivated by the desire to use active control to reduce or eliminate the self-sustained oscillations, for instance by moving a flap or injecting mass into the flow periodically. Modern control theory provides many powerful tools both for designing feedback control systems, and for analyzing limitations of control. To use these tools most effectively, one first needs a model of the system, typically in the form of a system of ordinary differential equations (ODEs). The motion of fluids is described very accurately by the Navier-Stokes equations, which are a system of nonlinear partial differential equations (PDEs) which are not solvable analytically for any but the simplest flows. To apply existing methods of control theory, it is necessary first to reduce the complexity of the system, preferably to a low-dimensional system of ODEs. The goal is not to describe every detail of the flow, but rather to eliminate unimportant details, and obtain the simplest possible mathematical model, while retaining just enough of the details to be able to accurately describe the general flow features one cares about, such as the size and frequency of the oscillations, and the deflection of the shear layer.

1.2 Historical perspective

Historically, the study of self-sustained oscillations began with studies on *edge tones* [Brown, 1937; Powell, 1953, 1961], in which a jet emerges from an orifice and impinges on a sharp edge.¹ The mechanism for edge tones is similar to the mechanism for cavity oscillations described above: disturbances are amplified by a shear layer, and scattered into acoustic waves by the sharp edge; the acoustic waves excite further instabilities, closing the feedback loop. The edge tone is the canonical problem which describes sound production in flue-type musical instruments such as flutes and organ pipes, and is a close relative of the cavity flow discussed in this thesis.

1.2.1 Cavity oscillations

Cavity flows have been studied as early as the 1950s, with the measurements of Roshko [1955] and the thesis of Krishnamurty [1956], who points out the connection with edge tones. The first description of the acoustic resonance phenomenon governing cavity oscillations (illustrated in figure 1.1) is usually attributed to Rossiter [1964], who provided a semi-empirical formula to predict the frequencies of oscillation (this formula is discussed later, in chapter 3). This description of the acoustic feedback mechanism was known earlier for edge tones (e.g., Powell [1953, 1961]), but Rossiter was the first to explicitly apply this mechanism to the cavity flow, and provide a formula for the resonant frequencies. Many enhancements to the basic theory have been given over the years, and are described in chapter 3.

Another mode of cavity oscillation has been observed, but has received much less attention, and is relatively poorly understood. In incompressible experiments

¹As Powell [1961] points out, an early description of self-sustained oscillations is also given by Lord Rayleigh, in his description of the bird-call [Rayleigh, 1945, §371].

for an axisymmetric cavity, Gharib & Roshko [1987] observed a *wake mode*, where the oscillating flow over the cavity resembles the wake behind a bluff body, rather than a free shear layer. Flow features in this wake mode were qualitatively very different from those in the *shear-layer mode* described by Rossiter, and wake mode was accompanied by a large increase in drag. Similar dramatic increases in drag had been previously observed by Fox [1968] as the cavity length was increased, in flows with thin, laminar upstream boundary layers, and Roshko [1955] observed an intermittency “analogous to the large fluctuations of drag which occur on a bluff cylinder in the critical range of Reynolds number,” where the flow may be switching between shear-layer mode and a type of wake mode. Recent experiments and numerical studies by Kriesels et al. [1995] for a flow past closed branches of a pipe (with both circular and 2D cross sections) also demonstrate flow structures that closely resemble wake mode.

More details about cavity oscillations in general may be found in review articles [e.g., Rockwell & Naudascher, 1978; Blake & Powell, 1986; Colonius, 2001]; see also the recent analytical work by Howe [1997] for very low Mach number cavity flows, and Crighton [1992] for edge tones.

Research in cavity flows has been renewed in recent years, largely because of the possibility of using active control to reduce the amplitude of oscillations. The idea of controlling cavity oscillations is not new, and goes back to Sarohia & Massier [1977] and Gharib [1987]. Most of the recent approaches to control have been either open-loop (no feedback) [Vakili & Gauther, 1991; Sarno & Franke, 1994; Stanek et al., 2000], or have involved phase-locked loops or adaptive controllers [Cattafesta et al., 1999; Shaw & Northcraft, 1999; Williams & Fabris, 2000b] which do not incorporate models of the cavity physics. The results of active control have not been completely successful: often, greater benefits are obtained by using passive techniques such as fixed spoilers [Vakili & Gauther, 1991], and often when active control is used to reduce the amplitude of one unstable frequency, the amplitude increases at another frequency [Williams & Fabris, 2000b]. In order to understand these effects, and the limitations and potential benefits of active control, one first needs a tractable model of the system. Modeling the cavity flow is the focus of this thesis.

1.2.2 Model reduction

In order to obtain low-order models for the cavity flow, we use some tools of dynamical systems theory, most notably the method of Proper Orthogonal Decomposition (POD) and Galerkin projection. Galerkin projection is a method for obtaining approximations to a high-dimensional (even infinite-dimensional) dynamical system by projecting the dynamics onto a low-dimensional subspace. Proper orthogonal decomposition is a method which uses data from simulations or experiments to determine a subspace which is optimal in a certain sense.

Also known as Karhunen-Loëve expansion, the POD was originally developed in the context of probability theory [Loëve, 1978], but the method has been used subsequently as a model-reduction tool, particularly for fluids and other systems

described by PDEs. In the fluids context, the major contributions are from Lumley [1970], Sirovich [1987], and Aubry et al. [1988], who used the method primarily to study the turbulent boundary layer. More recently, the method has been used to study other flows (e.g., Khibnik et al. [1998]), but so far all of the flows studied have been incompressible. (Several researchers have computed POD modes for compressible flows [Ukeiley et al., 2000], but have used the POD modes only to identify coherent structures in data, not to develop dynamical models.) One of the major contributions of this thesis is to establish a framework for applying the POD/Galerkin method to compressible flows.

1.3 Overview of contributions

The main contributions of this thesis are as follows:

- Direct Numerical Simulations (DNS) of the two-dimensional, compressible, subsonic flow past a rectangular cavity, along with the radiated acoustic field.
- Investigation of the *wake mode* of cavity oscillations, and criteria for predicting the onset of wake mode.
- Extension of the POD/Galerkin method to compressible flows, valid for cold flows at moderate Mach number.
- Comparison of reduced-order models obtained from scalar-valued POD modes and vector-valued POD modes.
- Development of a controller to reduce cavity oscillations, based on linear conceptual models of the cavity physics.
- Implementation of controllers on an experiment, demonstrating noise reduction, and some limitations of control.

In chapter 2, we give an overview of linear stability analysis of parallel flows, which will be used throughout this thesis. Chapter 3 gives a description of the numerical method used to compute the flow past a cavity, and describes characteristics of the flow in detail, including both shear-layer mode and wake mode. We propose that wake mode arises when the amplitude of oscillations exceeds a certain threshold, possibly creating a region of absolute instability in the shear layer.

Chapter 4 contains the model-reduction methods developed in this thesis: an overview of the standard POD/Galerkin procedure is presented, along with a brief description of the existing methods for incompressible flow. One of the main contributions of this thesis is the extension of these methods to compressible flows, presented at the end of this chapter.

In chapter 5, we apply these methods to the cavity flow, and compare models obtained from scalar-valued POD modes to those obtained from vector-valued modes.

Chapter 6 presents a conceptual modeling approach, based on the Rossiter mechanism, where we model each component of the flow separately (e.g., shear-layer amplification, acoustic propagation). These models are linear, and we use them to design controllers using the Linear Quadratic Gaussian (LQG) design technique. We implement these controllers on an experiment, and discuss the results in chapter 6.

Chapter 2

Linear Stability of Parallel Shear Flows

Since the late 19th century, linear stability theory has played an important role in modeling of shear flows. The first theoretical contributions appear in the famous paper of von Helmholtz [1868], who established the appropriate boundary conditions at a discontinuity between two streams with different velocities. The stability of this boundary was first addressed by Kelvin [1871], who looked at the motion of a free surface of water as wind blows over it, and to this day the instability of a flow with two parallel streams bears the name Kelvin-Helmholtz instability.

The foundations of the modern linear stability theory were laid by Rayleigh [1880], who used his new framework to prove remarkable results about the stability of jet profiles. Rayleigh's theory persists today, virtually unchanged, and this theory, with some modern accoutrements, forms the subject of the present chapter.

Linear stability theory will be used frequently in subsequent chapters, to describe the behavior of the shear layer spanning a rectangular cavity. The developments here will be from this perspective, considering the appropriate flow assumptions and boundary conditions. Most of the results are well known, but scattered throughout the literature, so here we collect them in one place, along with a few recent results, such as the adjoint equations and biorthogonality relation developed in sections 2.6 and 2.7. We describe a locally parallel theory, for inviscid flows. We develop the compressible Rayleigh equation, along with the corresponding adjoint equations, and discuss a biorthogonality condition which is useful for expanding arbitrary flow disturbances in terms of eigenfunctions of the Rayleigh problem.

2.1 Equations of motion

We assume that the flow is *two-dimensional*, *compressible*, and *isentropic*, and is thus described by the Euler equations for an ideal fluid, written in Cartesian

coordinates as

$$\frac{D\rho}{Dt} + \rho \operatorname{div} \mathbf{u} = 0 \quad (2.1)$$

$$\rho \frac{D\mathbf{u}}{Dt} + \nabla p = 0 \quad (2.2)$$

$$\frac{Dp}{Dt} + \gamma p \operatorname{div} \mathbf{u} = 0, \quad (2.3)$$

where $D/Dt := \partial/\partial t + \mathbf{u} \cdot \nabla$ denotes the material derivative. The density ρ and velocity $\mathbf{u} = (u, v)$ are nondimensionalized by the freestream quantities ρ_∞ and U_∞ , the pressure p is nondimensionalized by $\rho_\infty U_\infty^2$, and lengths are nondimensionalized by a length D , as yet unspecified. In writing the energy equation in the form (2.3), we assume the fluid is an *ideal gas* with *constant specific heats*, that there is *no heat addition*, and that *no body forces* act on the fluid.

Next, we linearize equations (2.1)–(2.3) about a parallel mean flow, writing

$$u(x, y, t) = \bar{U}(y) + \delta u(x, y, t) \quad (2.4)$$

$$v(x, y, t) = \delta v(x, y, t) \quad (\text{parallel flow}) \quad (2.5)$$

$$\rho(x, y, t) = \bar{\rho}(y) + \delta \rho(x, y, t) \quad (2.6)$$

$$p(x, y, t) = \bar{p} + \delta p(x, y, t). \quad (2.7)$$

We obtain the linearized equations by inserting (2.4)–(2.7) into equations (2.1)–(2.3) and neglecting products of fluctuations:

$$\begin{aligned} \left(\frac{\partial}{\partial t} + \bar{U} \frac{\partial}{\partial x} \right) \delta \rho + \bar{\rho}' \delta v + \bar{\rho} \left(\frac{\partial}{\partial x} \delta u + \frac{\partial}{\partial y} \delta v \right) &= 0 \\ \bar{\rho} \left(\frac{\partial}{\partial t} + \bar{U} \frac{\partial}{\partial x} \right) \delta u + \bar{\rho} \bar{U}' \delta v + \frac{\partial}{\partial x} \delta p &= 0 \\ \bar{\rho} \left(\frac{\partial}{\partial t} + \bar{U} \frac{\partial}{\partial x} \right) \delta v + \frac{\partial}{\partial y} \delta p &= 0 \\ \left(\frac{\partial}{\partial t} + \bar{U} \frac{\partial}{\partial x} \right) \delta p + \frac{1}{M^2} \left(\frac{\partial}{\partial x} \delta u + \frac{\partial}{\partial y} \delta v \right) &= 0, \end{aligned}$$

where primes denote differentiation, and $M = U_\infty/a_\infty$ is the free-stream Mach number. Here we have used $\bar{p} = 1/(\gamma M^2)$, which follows from the equation of state for an ideal gas ($a_\infty^2 = \gamma p_\infty / \rho_\infty$). Note that the density equation decouples, so we need only consider the last three equations.

Next, we write the fluctuations as *normal modes*

$$\delta f(x, y, t) = \hat{f}(y) e^{i(\alpha x + \omega t)}, \quad \text{where } f = u, v, \text{ or } p, \quad (2.8)$$

where $\alpha, \omega \in \mathbb{C}$. Since the equations are linear, a linear combination of solutions is also a solution, so by superposing normal modes we may construct more complicated solutions.

By inserting the normal modes into the linearized equations, we obtain the

system of ordinary differential equations (ODEs)

$$L_{\omega,\alpha}\varphi = 0, \quad (2.9)$$

where $\varphi = (\hat{u}, \hat{v}, \hat{p})^T$ and

$$L_{\omega,\alpha} = \begin{pmatrix} \bar{\rho}(i\omega + i\alpha\bar{U}) & \bar{\rho}\bar{U}' & i\alpha \\ 0 & \bar{\rho}(i\omega + i\alpha\bar{U}) & \frac{d}{dy} \\ i\alpha & \frac{d}{dy} & M^2(i\omega + i\alpha\bar{U}) \end{pmatrix}. \quad (2.10)$$

From these equations, straightforward Gaussian elimination yields a single ODE in \hat{p} , known as the *compressible Rayleigh equation*:

$$\frac{d^2\hat{p}}{dy^2} - \left(\frac{2\alpha\bar{U}'}{\omega + \alpha\bar{U}} + \frac{\bar{\rho}'}{\bar{\rho}} \right) \frac{d\hat{p}}{dy} - (\alpha^2 - \bar{\rho}M^2(\omega + \alpha\bar{U})^2) \hat{p} = 0. \quad (2.11)$$

The incompressible Rayleigh equation is recovered by setting $M = 0$, $\bar{\rho} = 1$, and is usually written in terms of \hat{v} , as originally derived by Rayleigh [1880]:

$$\left(\frac{\omega}{\alpha} + \bar{U} \right) \left(\frac{d^2\hat{v}}{dy^2} - \alpha^2\hat{v} \right) - \bar{U}''\hat{v} = 0. \quad (2.12)$$

Note that both of these forms of Rayleigh's equation are singular when $\bar{U} = -\omega/\alpha$. This case can be important, and is addressed in section 2.5.

2.2 Mean profiles and boundary conditions

Later, we shall use the above equations to describe the shear layer over a rectangular cavity. Here we discuss the mean profiles and boundary conditions appropriate for this problem.

For the shear layer spanning the cavity, we shall use two different velocity profiles: actual mean profiles measured from simulations, and a hyperbolic tangent profile given by

$$\bar{U}(y) = \frac{1}{2} \left(1 + \tanh \frac{2y}{\delta_\omega} \right) \quad (2.13)$$

which describes a free shear layer with (nondimensional) speed 1 in the upper stream, zero velocity in the lower stream, and with vorticity thickness δ_ω . Recall that the *vorticity thickness* of a shear layer is defined by

$$\delta_\omega = \frac{U_2 - U_1}{\max_y \bar{U}'(y)} \quad (2.14)$$

where $\bar{U}(y)$ is the mean velocity profile of the shear layer, and U_2 and U_1 are the speeds in the upper and lower streams, respectively [Brown & Roshko, 1974].

(Here, $U_2 = 1$, $U_1 = 0$.) Another quantity frequently used is the *momentum thickness*

$$\theta = \int_{-\infty}^{\infty} \bar{U}(1 - \bar{U}) dy. \quad (2.15)$$

For the velocity profile (2.13), the two are related by $\delta_{\omega} = 4\theta$. As we discuss in chapter 3, the vorticity thickness is more appropriate for describing shear layers over cavities.

Throughout, we will assume the mean density is uniform, $\bar{\rho} = 1$. This assumption is good for cold flows at the moderate subsonic speeds we consider.

The developments in the preceding section assume that the flow is uniform in the streamwise direction, so in modeling a shear layer over a cavity, we necessarily neglect the presence of the upstream and downstream cavity walls. We may include the effect of the cavity floor, however, by imposing a wall boundary condition. We denote the cavity depth by D , and use this D as the length scale in the nondimensionalization. The wall boundary condition is then

$$\hat{v} = 0, \quad \text{i.e.} \quad \frac{d\hat{p}}{dy} = 0, \quad \text{at } y = -1. \quad (2.16)$$

The remaining boundary condition is that the pressure be bounded as $y \rightarrow \infty$. Far from the cavity, the mean profiles are uniform, and so the governing equation (2.11) reduces to

$$\frac{d^2\hat{p}}{dy^2} - (\alpha^2 - M^2(\omega + \alpha)^2)\hat{p} = 0 \quad (2.17)$$

which has solution

$$\hat{p} = c_1 e^{-\lambda y} + c_2 e^{\lambda y} \quad (2.18)$$

where $\lambda^2 = \alpha^2 - M^2(\omega + \alpha)^2$. Since the pressure must remain bounded as $y \rightarrow \infty$, this implies $c_2 = 0$ (where we choose the standard branch of the square root for λ). The farfield boundary condition is then

$$\hat{p} = c_1 e^{-\lambda y} \quad \text{as } y \rightarrow \infty. \quad (2.19)$$

2.3 Method of solution: spatial vs. temporal

The governing equation (2.11) together with the boundary conditions (2.16) and (2.19) determine a linear homogeneous boundary value problem, and hence an eigenvalue problem.¹ Nontrivial solutions for \hat{p} exist only for certain values of the

¹Strictly speaking, in an eigenvalue problem the parameter must appear linearly, which is not true for either ω or α in (2.11). However, both ω and α do appear linearly in (2.9), so this equation should be thought of as the true eigenvalue problem, and (2.11) a convenient representation of it.

parameters ω and α , satisfying a particular relation of the form

$$F(\omega, \alpha) = 0 \quad (2.20)$$

for some function F (which is not known explicitly). This equation is called the *dispersion relation*, and relates frequencies of waves to their corresponding wavenumbers.

In fluid mechanics, we often look for solutions of (2.20) such that either $\text{Im}(\omega) = 0$ or $\text{Im}(\alpha) = 0$. Consider the former case first. If the dispersion relation (2.20) has a solution with $\text{Im}(\omega) = 0$ and $\text{Im}(\alpha) < 0$, the corresponding normal mode (2.8) will be oscillating at a particular frequency in time, but exponentially growing in space. Such a situation is called *spatial instability*. Next consider solutions of (2.20) with $\text{Im}(\alpha) = 0$. If there is a solution with $\text{Im}(\omega) < 0$, then the corresponding normal mode will be sinusoidal in space, and exponentially growing in time. This situation is called *temporal instability*. If \hat{p} is an eigenfunction with either $\text{Im}(\alpha) < 0$ (with $\omega \in \mathbb{R}$) or $\text{Im}(\omega) < 0$ (with $\alpha \in \mathbb{R}$), we call \hat{p} an *unstable mode*. Correspondingly, if \hat{p} is an eigenfunction with either $\text{Im}(\alpha) > 0$ or $\text{Im}(\omega) > 0$, we call \hat{p} a *stable mode* (or *damped mode*). If both $\omega, \alpha \in \mathbb{R}$, then \hat{p} is a *neutrally stable mode*. We consider only the cases when at least one of ω, α is real.

In modeling spatially developing shear layers, the spatial approach is more appropriate, and results from spatial stability analysis agree well with experiment [Michalke, 1984], so it is the approach we take here. The general procedure is, given a frequency $\omega \in \mathbb{R}$, to look for a value of $\alpha \in \mathbb{C}$ such that the boundary value problem (BVP) given by (2.11), (2.16), (2.19) has a solution. This procedure is made systematic as follows.

We start by choosing an initial guess for α , and attempting to solve the linear two-point BVP by shooting. We write equation (2.11) in first-order form

$$\frac{d\hat{p}}{dy} = \hat{p}' \quad (2.21)$$

$$\frac{d\hat{p}'}{dy} = (\alpha^2 - \bar{\rho}M^2(\omega + \alpha\bar{U})^2) \hat{p} + \left(\frac{2\alpha\bar{U}'}{\omega + \alpha\bar{U}} + \frac{\bar{\rho}'}{\bar{\rho}} \right) \hat{p}' \quad (2.22)$$

with boundary conditions

$$\hat{p}(-1) = c \quad \hat{p}(y \rightarrow \infty) = de^{-\lambda y} \quad (2.23)$$

$$\hat{p}'(-1) = 0 \quad \hat{p}'(y \rightarrow \infty) = -\lambda de^{-\lambda y} \quad (2.24)$$

where c and d are constants, now arbitrary. To solve the BVP, we integrate the equation from $y = -1$ to an arbitrary point $y = y_0$, and call this half of a solution $p_1(y)$. We then integrate the equation from $y = \infty$ (in a real computation, from some large value where the mean fields are approximately constant) to $y = y_0$, and call this part of the solution $p_2(y)$. For the BVP to have a continuous solution, we must choose the constants c and d such that $p_1(y_0) = p_2(y_0)$ and

$p'_1(y_0) = p'_2(y_0)$. These two conditions are simultaneously possible only when $p_1/p'_1 = p_2/p'_2$ at y_0 , or when

$$G(\alpha) = (p_1 p'_2 - p_2 p'_1) \big|_{y_0} = 0. \quad (2.25)$$

Note that, holding c , d , and ω constant, the value of G depends only on α . If G is analytic, then we may use Newton-Raphson iteration to solve the algebraic equation $G(\alpha) = 0$ for the eigenvalue α . The normalization of the eigenfunctions is arbitrary, and we choose the normalization $\max_y \hat{v} = 1$.

2.4 Number of unstable eigenvalues

For typical shear profiles \bar{U} that we use in this thesis, there is only one unstable eigenvalue α for each frequency ω . Many important compressible flows (e.g., high-speed jets) have several unstable modes that may be important [Sandham & Reynolds, 1989], and it is desirable to be able to characterize when multiple unstable modes might arise.

Unfortunately, for the compressible Rayleigh equation, no general results are known—the number of unstable modes is usually determined empirically, by solving the equations numerically and searching for eigenvalues. However, for the temporal stability analysis of the incompressible Rayleigh equation, some strong results are available, and it is plausible that for the low Mach numbers we are interested in, similar results are true for the compressible equation. We briefly summarize the most important of these results for the incompressible Rayleigh equation (2.12). Except where noted, these results concern the *temporal* stability analysis, where we fix $\alpha \in \mathbb{R}$, and search for eigenvalues $\omega \in \mathbb{C}$. In particular, we focus on unstable eigenvalues (for which $\text{Im}(\omega) < 0$).

In his landmark paper, Rayleigh [1880] demonstrated that a necessary condition for unstable eigenvalues is that \bar{U}'' must change sign over the range of integration—i.e., the velocity profile must have an inflection point. Minor refinements to this necessary condition had been made (see Drazin & Reid [1981] for the details), but the next major advance was not until 80 years later, with *Howard's circle theorem* [Howard, 1961]. Letting $c = -\omega/\alpha$, this theorem states that unstable eigenvalues c must lie within the semicircle with diameter equal to the range of the velocity profile \bar{U} . A few years later, Howard [1964] proved the following powerful result:

Theorem 2.1 *For a class of velocity profiles, the number of unstable modes cannot exceed the number of inflection points. The class of velocity profiles $\bar{U}(y)$ satisfies $\bar{U}''(y) = -K(y)(\bar{U}(y) - c_s)$ for some piecewise continuous non-negative function $K(y)$ and for some number c_s .*

The tanh velocity profile we consider falls into this category (with $c_s = 1/2$), and possesses only one inflection point, so for the incompressible, temporal analysis, we are guaranteed only one unstable eigenvalue.

These results were further generalized by Sattinger [1967], who proved that under fairly general conditions on the velocity profile, there are at most a finite number of complex eigenvalues (thus the continuous spectrum is real), and who also generalized Howard's circle theorem to show that all points in the spectrum (not just unstable discrete eigenvalues) lie within the circle with diameter equal to the range of \bar{U} .

More recent results for the incompressible Orr-Sommerfeld equation (which includes viscous effects) were given by Salwen and Gorsch, who showed that both temporal and spatial problems have a continuous spectrum [Gorsch & Salwen, 1978], and who gave a biorthogonality relation for the adjoint problem [Salwen & Gorsch, 1981]. We discuss the biorthogonality relation for the compressible equations in section 2.6.

2.5 Singularity at the critical layer

It was mentioned in section 2.1 that the governing equation (2.11) has a singular point where $\bar{U}(y) = -\omega/\alpha$. Although this singularity lies on the integration path (in the complex y -plane) only when ω and α are both real, we must still be very careful about the treatment of this singularity when we compute damped modes (with $\text{Im}(\alpha) > 0$), as we describe below. The idea is to construct a damped-mode solution that is the analytic continuation of an unstable-mode solution, following the approach of Tam & Morris [1980].

Suppose that $\omega + \alpha\bar{U}(y_c) = 0$, but $\bar{U}'(y_c) \neq 0$, so that y_c is a regular singular point of equation (2.11). (This locus of points in the fluid where $y = y_c$ is usually called the *critical layer* [Drazin & Reid, 1981].) We first examine the type of singularity of the solution $\hat{p}(y)$ at y_c . A standard Frobenius series analysis [Coddington & Levinson, 1955] shows that the indicial equation has two solutions which differ by an integer, and so the solution \hat{p} has a logarithmic singularity at y_c . For the velocity profile (2.13), with $\omega > 0$ and $\text{Im}(\alpha) < 0$ (an unstable mode), the singularity y_c lies in the lower half y -plane. Thus, since the solution is valid for real y , the branch cut of the logarithmic function must extend from y_c to infinity in the lower half y -plane, as shown in figure 2.1.

If we increase the frequency ω , the locus of y_c moves toward the real axis of the y -plane, and eventually crosses it (when $\text{Im}(\alpha) > 0$, thus becoming a stable mode). Once y_c crosses the real axis into the upper-half plane, we must be careful not to integrate through the branch cut which extends from y_c into the lower-half plane. For this damped-mode solution to be the analytic continuation of the unstable-mode solution, we must deform the integration contour into the upper-half plane to avoid crossing the branch cut (see figure 2.1).

When deforming the contour in the complex y -plane, we must pay close attention to the domain of the velocity profile $\bar{U}(y)$, to avoid inadvertently integrating around a branch point of the map $\bar{U} \mapsto y$. For the tanh profile (2.13), the function $\bar{U} \mapsto y$ is multiple-valued, and has two branch points, the points 0 and 1 on the real axis, as shown in figure 2.2. The usual integration contour (on the real y -axis)

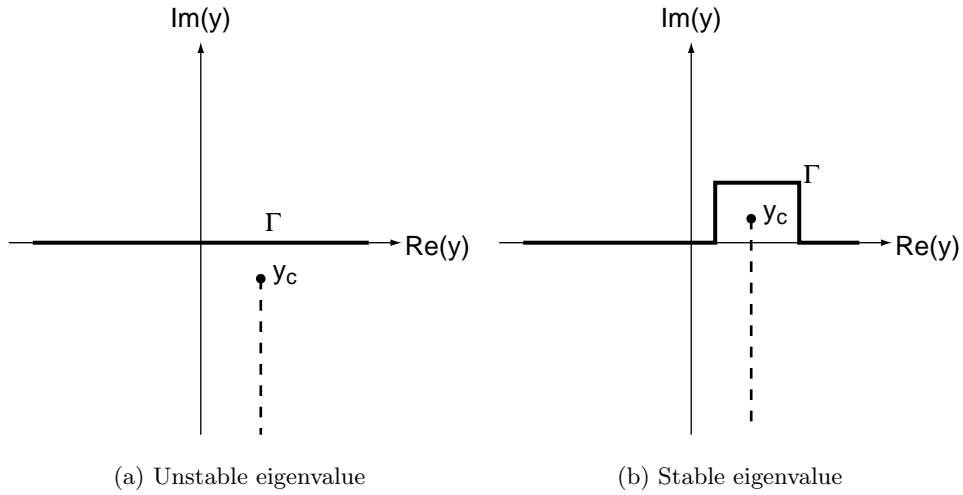


Figure 2.1: Location of branch points of the solution $\hat{p}(y)$, and integration contours for the Rayleigh equation.

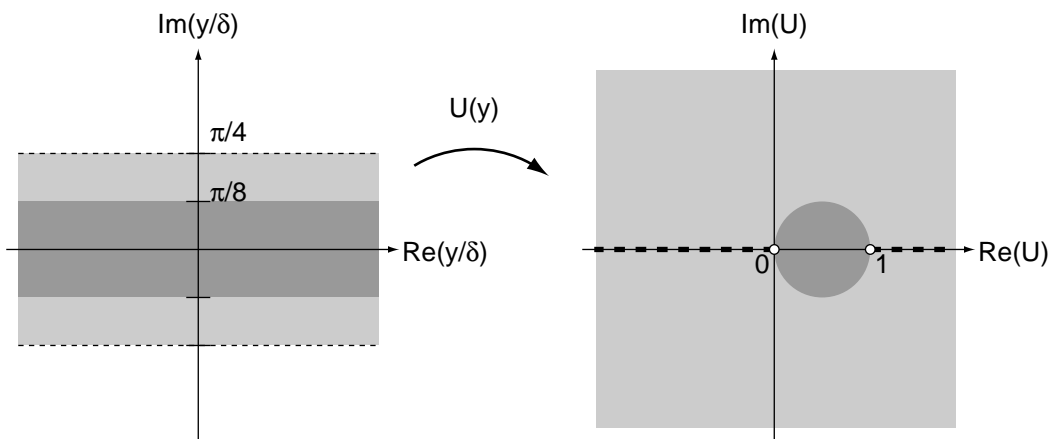


Figure 2.2: Domain of velocity profile $\bar{U}(y)$, with branch cuts indicated in the \bar{U} -plane. Howard's circle theorem states that eigenvalues $-\omega/\alpha$ must lie within the dark shaded circle in the \bar{U} -plane, which maps to the dark shaded strip in the y -plane.

maps to the interval $(0, 1)$ in the \bar{U} -plane, so we choose branch cuts from $(-\infty, 0]$ and $[1, \infty)$ in the \bar{U} -plane, as shown. The range of this branch of the function $\bar{U} \mapsto y$ is the strip $-\pi/4 < \text{Im}(y/\delta_\omega) < \pi/4$. One must be careful not to deform the integration contour outside this strip, or the corresponding contour in the \bar{U} -plane will go through the branch cuts, and go the wrong way around the branch points, changing the value of the integral. Note also that by Howard's circle theorem, eigenvalues $-\omega/\alpha$ (and therefore critical points where $\bar{U}(y_c) = -\omega/\alpha$) must lie within the circle indicated, which maps to the strip $-\pi/8 < \text{Im}(y/\delta_\omega) < \pi/8$ in the y -plane.

Profiles from data. Sometimes it is desirable to use a velocity profile determined from data, either experimental or numerical. In this case, in order to indent the contour into the complex plane, one must fit an analytic function to the data, and verify that the integration contour does not leave the region of convergence of the function. In this thesis, whenever we have stable (or nearly stable) eigenvalues, we fit our measured profiles to tanh profiles, to avoid these difficulties.

2.6 Adjoint equations

To determine how disturbances are amplified by the shear layer, we shall want to expand an arbitrary disturbance as a sum of eigenfunctions of the Rayleigh problem. (It is shown in Salwen & Grosch [1981] that the temporal eigenfunctions form a complete set, but their result does not hold for the spatial eigenfunctions.) In order to obtain the coefficients in this expansion, it is useful to have a set of functions which are orthogonal to the eigenfunctions. We may obtain such a set of functions by solving the adjoint problem.

We begin by defining the inner product on complex vector-valued functions $\langle \cdot, \cdot \rangle : L^2(\Gamma) \times L^2(\Gamma) \rightarrow \mathbb{C}$ by

$$\langle f, g \rangle = \int_{\Gamma} g^* f \, dy, \quad (2.26)$$

where $*$ denotes Hermitian transpose, and Γ is the domain of the ODE we are considering. Here, we take $\Gamma = [-1, \infty)$, but the extension to contours off the real axis is trivial. Under this inner product, the formal adjoint of $L_{\omega, \alpha}$ is

$$\tilde{L}_{\omega, \alpha} = \begin{pmatrix} -\bar{\rho}(i\omega^* + i\alpha^* \bar{U}) & 0 & -i\alpha^* \\ \bar{\rho}\bar{U}' & -\bar{\rho}(i\omega^* + i\alpha^* \bar{U}) & -\frac{d}{dy} \\ -i\alpha^* & -\frac{d}{dy} & -M^2(i\omega^* + i\alpha^* \bar{U}) \end{pmatrix}. \quad (2.27)$$

Writing $\tilde{\varphi} = (\tilde{u}, \tilde{v}, \tilde{p})^T$, the *Lagrange identity* then gives

$$\tilde{\varphi}^* L_{\omega, \alpha} \varphi - (\tilde{L}_{\omega, \alpha} \tilde{\varphi})^* \varphi = \frac{d}{dy} (\tilde{v}^* p + \tilde{p}^* v), \quad (2.28)$$

for any $\varphi, \tilde{\varphi}$ (see Coddington & Levinson [1955] or Stakgold [2000] for a general description of the Lagrange identity). Integrating over the domain Γ , we obtain

$$\langle L_{\omega,\alpha}\varphi, \tilde{\varphi} \rangle - \langle \varphi, \tilde{L}_{\omega,\alpha}\tilde{\varphi} \rangle = (\tilde{v}^*p + \tilde{p}^*v) \Big|_{-1}^{\infty}. \quad (2.29)$$

Note that the boundary terms vanish if we impose the boundary conditions

$$\tilde{v}(-1) = 0, \quad (2.30)$$

$$\tilde{p} \rightarrow 0 \quad \text{as } y \rightarrow \infty. \quad (2.31)$$

Gaussian elimination on the equation $\tilde{L}_{\omega,\alpha}\tilde{\varphi} = 0$, again yields a single equation for the adjoint pressure

$$\frac{d^2\tilde{p}^*}{dy^2} - \frac{\bar{\rho}'}{\bar{\rho}} \frac{d\tilde{p}^*}{dy} - \tilde{p}^* \left(\alpha^2 - \bar{\rho}M^2(\omega + \alpha\bar{U})^2 + \frac{\bar{\rho}'}{\bar{\rho}} \frac{\alpha\bar{U}'}{\omega + \alpha\bar{U}} + 2 \left(\frac{\alpha\bar{U}'}{\omega + \alpha\bar{U}} \right)^2 - \frac{\alpha\bar{U}''}{\omega + \alpha\bar{U}} \right) = 0 \quad (2.32)$$

as well as the expressions

$$\tilde{u}^* = \frac{-\alpha}{\bar{\rho}(\omega + \alpha\bar{U})} \tilde{p}^* \quad (2.33)$$

$$\tilde{v}^* = \frac{-1}{\bar{\rho}(i\omega + i\alpha\bar{U})} \left(\bar{\rho}\bar{U}'\tilde{u}^* - \frac{d\tilde{p}^*}{dy} \right). \quad (2.34)$$

Using (2.34), the boundary condition (2.30) becomes

$$\frac{d\tilde{p}^*}{dy} = -\frac{\alpha\bar{U}'}{\omega + \alpha\bar{U}} \tilde{p}^* \quad \text{at } y = -1. \quad (2.35)$$

The farfield boundary condition is the same as (2.19), with p replaced by \tilde{p}^* . The resulting two-point BVP is solved as described in section 2.3 for the Rayleigh equation.

2.7 Biorthogonality relation

We now establish the following relation between solutions of the Rayleigh equation and adjoint solutions.

Theorem 2.2 (Biorthogonality) *If $L_{\omega_1,\alpha_1}\varphi_1 = 0$ and $\tilde{L}_{\omega_2,\alpha_2}\tilde{\varphi}_2 = 0$, then*

$$(\omega_1 - \omega_2) \langle\langle \varphi_1, \tilde{\varphi}_2 \rangle\rangle + (\alpha_1 - \alpha_2) [\![\varphi_1, \tilde{\varphi}_2]\!] = 0, \quad (2.36)$$

where $\langle\langle f, g \rangle\rangle = \langle Af, g \rangle$ and $\llbracket f, g \rrbracket = \langle Bf, g \rangle$, with

$$A(y) = \begin{pmatrix} \bar{\rho} & 0 & 0 \\ 0 & \bar{\rho} & 0 \\ 0 & 0 & M^2 \end{pmatrix}, \quad B(y) = \begin{pmatrix} \bar{\rho}\bar{U} & 0 & 1 \\ 0 & \bar{\rho}\bar{U} & 0 \\ 1 & 0 & M^2\bar{U} \end{pmatrix}. \quad (2.37)$$

Proof: We have

$$\begin{aligned} 0 &= \langle L_{\omega_1, \alpha_1} \varphi_1, \tilde{\varphi}_2 \rangle - \langle \varphi_1, \tilde{L}_{\omega_2, \alpha_2} \tilde{\varphi}_2 \rangle \\ &= \langle (L_{\omega_1, \alpha_1} - L_{\omega_2, \alpha_2}) \varphi_1, \tilde{\varphi}_2 \rangle \\ &= i(\omega_1 - \omega_2) \langle A\varphi_1, \tilde{\varphi}_2 \rangle + i(\alpha_1 - \alpha_2) \langle B\varphi_1, \tilde{\varphi}_2 \rangle \\ &= i(\omega_1 - \omega_2) \langle\langle \varphi_1, \tilde{\varphi}_2 \rangle\rangle + i(\alpha_1 - \alpha_2) \llbracket \varphi_1, \tilde{\varphi}_2 \rrbracket, \end{aligned}$$

which establishes the result. ■

Strictly speaking, the term ‘‘orthogonal’’ is not entirely appropriate here: although $\langle\langle \cdot, \cdot \rangle\rangle$ is indeed an inner product (assuming $\bar{\rho}, M > 0$), on the contrary $\llbracket \cdot, \cdot \rrbracket$ is typically not positive definite (e.g., for $|\bar{\rho}\bar{U}| < 1$ and $|M^2\bar{U}| < 1$), and thus is not truly an inner product. However, we retain the terminology to be consistent with the literature [Salwen & Gorsch, 1981; Colonius et al., 1998].

The two biorthogonality relations follow immediately:

Corollary 2.3 *If $L_{\omega_1, \alpha} \varphi_1 = 0$ and $\tilde{L}_{\omega_2, \alpha} \tilde{\varphi}_2 = 0$, with $\omega_1 \neq \omega_2$, then $\langle\langle \varphi_1, \tilde{\varphi}_2 \rangle\rangle = 0$.*

Corollary 2.4 *If $L_{\omega, \alpha_1} \varphi_1 = 0$ and $\tilde{L}_{\omega, \alpha_2} \tilde{\varphi}_2 = 0$, with $\alpha_1 \neq \alpha_2$, then $\llbracket \varphi_1, \tilde{\varphi}_2 \rrbracket = 0$.*

Example: expansion in spatial eigenfunctions. Suppose we are given a sinusoidal disturbance, imposed at a fixed streamwise location x_0 , with some known frequency ω , and we wish to determine how this disturbance evolves as it propagates downstream. Specifically, write the disturbance as $(u, v, p)(x_0, y, t) = f(y)e^{i\omega t}$, where $f(y) = (u, v, p)(x_0, y, 0)$. To solve this problem, we expand $f(y)$ in terms of (spatial) eigenfunctions of the Rayleigh problem. We can then easily determine how the disturbance evolves, since we know how the eigenfunctions evolve.

Assuming the spatial eigenfunctions form a complete set, we expand $f(y)$ as a sum of eigenfunctions with different values of α :

$$f(y) = \sum_{j=1}^{N(\omega)} a_j \varphi_{\omega, \alpha_j}(y) + \int_{\sigma(\omega)} a(\nu) \varphi_{\omega, \nu}(y) d\nu, \quad (2.38)$$

where $N(\omega)$ is the number of discrete eigenvalues for the given ω , $\sigma(\omega)$ is the continuous spectrum of $L_{\omega, \alpha}$, and

$$L_{\omega, \alpha_j} \varphi_{\omega, \alpha_j} = 0, \quad j = 1, \dots, N(\omega) \quad (2.39)$$

$$L_{\omega, \nu} \varphi_{\omega, \nu} = 0, \quad \nu \in \sigma(\omega). \quad (2.40)$$

Suppose α_1 is the only unstable eigenvalue, and we are interested in the coefficient a_1 of the corresponding eigenfunction, to see how this disturbance will grow as it propagates downstream. Then, to obtain the coefficient of the eigenfunction $\varphi_{\omega,\alpha_1}$, we find the corresponding *adjoint* eigenfunction $\tilde{\varphi}_{\omega,\alpha_1}$, which satisfies $\tilde{L}_{\omega,\alpha_1} \tilde{\varphi}_{\omega,\alpha_1} = 0$. Then, applying theorem 2.2, we obtain

$$a_1 \llbracket \varphi_{\omega,\alpha_1}, \tilde{\varphi}_{\omega,\alpha_1} \rrbracket = \llbracket f, \tilde{\varphi}_{\omega,\alpha_1} \rrbracket, \quad (2.41)$$

which is easily solved for a_1 (provided the coefficient on the left-hand side is non-zero, which is the generic case).

Chapter 3

Physics of Cavity Oscillations

This chapter presents a detailed study of the physical mechanisms underlying oscillations in the flow past a cavity. Direct numerical simulations are used to study the flow, and reveal two distinct types of oscillations: a *shear-layer* mode, which resembles most cavity flows which have been studied in the past, and a *wake mode*, which is less well understood. We present a model of the scaling laws governing the oscillations, and use the model to predict transitions between the flow regimes.

3.1 Numerical method

Flows with self-sustained oscillations are inherently difficult to model computationally, because of their sensitivity to disturbances. In the cavity flow, for instance, the shear layer spanning the cavity amplifies flow disturbances, so small numerical errors at the cavity leading edge will be amplified exponentially as they travel downstream. If these numerical errors arise from artificial reflections at a computational boundary, for instance, they may be indistinguishable from physical disturbances, and may even cause the flow to resonate at non-physical frequencies. Furthermore, in the cavity flow, the governing feedback mechanism is acoustic, so a high-order, low-dissipative numerical method is necessary to accurately resolve acoustic waves, which are usually many orders of magnitude smaller than hydrodynamic flow disturbances.

3.1.1 Equations of motion

We solve the fully compressible Navier-Stokes equations in two dimensions, written in conservative form as follows:

$$\begin{aligned} \frac{\partial \rho}{\partial t} + \frac{\partial}{\partial x_j}(\rho u_j) &= 0 \\ \frac{\partial \rho u_i}{\partial t} + \frac{\partial}{\partial x_j}(\rho u_i u_j + p \delta_{ij}) &= \frac{1}{\text{Re}} \frac{\partial}{\partial x_j} \left(\frac{\partial u_i}{\partial x_j} + \frac{\partial u_j}{\partial x_i} - \frac{2}{3} \frac{\partial u_k}{\partial x_k} \delta_{ij} \right) \\ \frac{\partial e}{\partial t} + \frac{\partial}{\partial x_j}((e + p)u_j) &= \frac{1}{\text{Re}} \frac{\partial}{\partial x_j} \left(u_i \left(\frac{\partial u_i}{\partial x_j} + \frac{\partial u_j}{\partial x_i} - \frac{2}{3} \frac{\partial u_k}{\partial x_k} \delta_{ij} \right) \right) + \frac{1}{\text{Re} \text{Pr}} \frac{\partial^2 T}{\partial x_k \partial x_k} \end{aligned} \quad (3.1)$$

together with the equation of state

$$p = \frac{\gamma - 1}{\gamma} \rho T.$$

Here, ρ is the density, u_i the velocity in the direction of coordinate x_i , p the pressure, T the temperature, γ the ratio of specific heats, and e the energy, defined by $e = \rho(E + |u|^2/2)$, where E is the internal energy per unit mass. These equations have been nondimensionalized according to the usual compressible nondimensionalization

$$\begin{aligned} \rho &= \frac{\rho^d}{\rho_\infty} & x_i &= \frac{x_i^d}{D} & t &= \frac{t^d a_\infty}{D} \\ u_i &= \frac{u_i^d}{a_\infty} & p &= \frac{p^d}{\rho_\infty a_\infty^2} & T &= \frac{T^d c_p}{a_\infty^2} \\ e &= \frac{e^d}{\rho_\infty a_\infty^2} & \text{Re} &= \frac{\rho_\infty a_\infty D}{\mu} & \text{Pr} &= \frac{c_p \mu}{k}, \end{aligned}$$

where the superscript $(\cdot)^d$ denotes the dimensional quantity. Here, c_p is the specific heat at constant pressure, k the thermal conductivity, Re the Reynolds number, and Pr the Prandtl number. The length scale D is the cavity depth. In this thesis, we will usually refer to the Reynolds number based on velocity U_∞ and momentum thickness θ_0 at the cavity leading edge, defined by

$$Re_\theta = \frac{\rho_\infty U_\infty \theta}{\mu} = \frac{M}{L/\theta_0} \text{Re}.$$

As temperature differences are small, we assume constant transport properties. We take $\text{Pr} = 0.7$ and $\gamma = 1.4$, the values for air. These equations are solved directly, meaning we use no turbulence model, and resolve all of the scales of the flow.

3.1.2 Numerical scheme

The equations (3.1) are solved using a sixth-order compact finite-difference scheme, described in Lele [1992], with a fourth-order Runge-Kutta time advancement. This combination of schemes results in very low dispersion and numerical dissipation, which allows for accurate wave propagation. The scheme has been used previously to study sound generation in mixing layers and jets, and is capable of resolving acoustic fields with velocity fluctuations five orders of magnitude smaller than near-field fluctuations [Colonius et al., 1997]. The method relies solely on physical viscosity for stability. A Cartesian grid is used, with clustering of grid points near the walls, and in the shear layer spanning the cavity. Analytical error function mappings are used for the grid stretching.

Boundary conditions play a key role in aeroacoustic computations. Artificial boundaries (inflow/outflow/normal) must allow vortical and acoustic waves to pass freely with minimal reflection. The exact nonreflecting boundary conditions for multidimensional problems are nonlocal in both space and time (i.e., one must solve convolution integrals), so in practice one typically uses local approximations, which take the form of partial differential equations to be solved at the boundaries, and errors in these approximations lead to reflections. Furthermore, another type of reflections arises from dispersive effects of the finite-difference scheme used. These errors are usually referred to as “spurious” numerical reflections, and are poorly resolved on the grid, while the former reflections are well resolved, and are referred to as “smooth” reflections. For linear equations, it is possible to derive local boundary conditions that are nonreflecting to arbitrary high order of accuracy, for both types of reflections [Rowley & Colonius, 2000], but for nonlinear equations the methods fail. At inflow and normal boundaries, one might be able to linearize the boundary conditions about the mean flow, since the fluctuations are small, but at the outflow, flow disturbances are large, severely limiting the accuracy of the linear boundary conditions [Colonius et al., 1993]. For nonlinear problems, recent techniques involve using a robust but low-order boundary condition (e.g., Thompson [1987], Poinsot & Lele [1992]), in conjunction with a *buffer zone* near the computational boundary, to attenuate the reflections. These buffer zone methods involve combinations of grid stretching and filtering [Colonius et al., 1993], and the addition of forcing terms to the equations [Freund, 1997].

The present method uses the boundary conditions of Poinsot & Lele [1992] for inflow, outflow, and normal boundaries, along with the buffer zone method of Freund [1997]. In the buffer zone, forcing terms of the form $\sigma(\mathbf{q} - \mathbf{q}_{\text{target}})$ are added to the right-hand side of the equations (3.1), where $\mathbf{q} = (\rho, \rho u, \rho v, e)$ is the vector of conservative variables, and $\mathbf{q}_{\text{target}}$ is the desired mean flow. The gain σ varies smoothly from a constant value at the boundary, to zero at the edge of the buffer (i.e., the edge of the “physical” portion of the computational domain). The wall boundary conditions are isothermal, at the same temperature as the freestream, using the formulation recommended by Poinsot & Lele [1992]. Since temperature variations are small, transport properties are assumed constant, and the Prandtl number is taken as 0.7, its value for air.

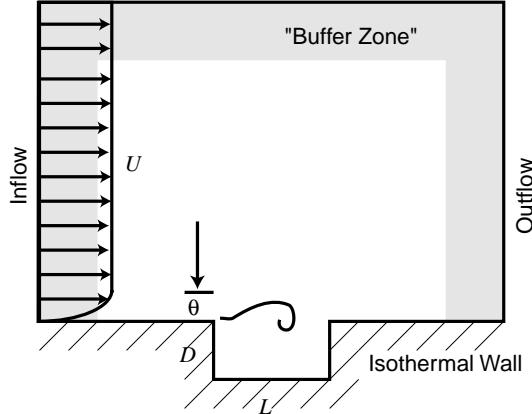


Figure 3.1: Schematic diagram of cavity configuration and computational domain.

A schematic diagram of the computational diagram is shown in figure 3.1. Typical grids (see captions of figures 3.2 and 3.3) contain about half a million grid points. The code is parallelized using a domain decomposition method, and has been run on 8 to 32 nodes of an IBM SP2.

The initial condition for all simulations is a (laminar) flat-plate boundary layer along the wall, and spanning the cavity. We use the (incompressible) Blasius profile and spreading rate [White, 1991]. The following parameters may be varied independently: the cavity length, relative to the initial momentum thickness at the cavity leading edge, L/θ_0 ; the Reynolds number $Re_\theta = \rho_\infty U \theta_0 / \mu$; the freestream Mach number $M = U/a_\infty$; and the cavity aspect ratio L/D . Because of the expense, only a small portion of parameter space may be investigated, and table 3.1 gives the parameters for the runs performed.

Note that the quoted values of θ_0 correspond to the momentum thickness of the boundary layer at the upstream edge, for the *initial condition*. For the runs in shear-layer mode, the variation from this initial value is small, but for the runs in wake mode, the variation is substantial. We use the initial momentum thickness because it is a parameter which is well defined a priori.

3.1.3 Validation

For flows with self-sustained oscillations, it is particularly important to verify that results are independent of the location of the boundaries, and the boundary treatment. As mentioned in the previous section, if boundaries are not treated properly, repeated non-physical reflections of waves can lead to self-forcing of the flow, in a process that is ultimately indistinguishable from physical instability. We have run several cases with variable boundary locations and grid spacings, to determine appropriate boundary locations and demonstrate grid convergence. The results of two of these tests are shown in figure 3.2 and 3.3.

Figure 3.2 shows the normal velocity at a single point in the shear layer ($x =$

| Run | L/D | L/θ_0 | M | Re_θ | Mode | St_D (wake mode) | C_D |
|------------|-------|--------------|-----|-------------|------|--------------------|-------|
| L1 | 1 | 20.3 | 0.6 | 73.9 | NO | - | 0.002 |
| L2 | 2 | 52.8 | 0.6 | 56.8 | SL | - | 0.008 |
| L3 | 3 | 75.0 | 0.6 | 60.0 | M | - | 0.031 |
| L4 | 4 | 102.1 | 0.6 | 58.8 | W | 0.064 | 0.227 |
| L5 | 5 | 123.3 | 0.6 | 60.8 | W | 0.054 | 0.404 |
| 4M2 | 4 | 102 | 0.2 | 58.8 | SL | - | |
| 4M3 | 4 | 102 | 0.3 | 58.8 | M | - | |
| 4M4 | 4 | 102 | 0.4 | 58.8 | W | 0.064 | |
| 4M5 | 4 | 102 | 0.5 | 58.8 | W | 0.064 | |
| 4M6 (L4) | 4 | 102 | 0.6 | 58.8 | W | 0.064 | |
| 4M7 | 4 | 102 | 0.7 | 58.8 | W | 0.061 | |
| 4M8 | 4 | 102 | 0.8 | 58.8 | W | 0.061 | |
| 2M2 | 2 | 52.8 | 0.2 | 56.8 | NO | - | |
| 2M3 | 2 | 52.8 | 0.3 | 56.8 | NO | - | |
| 2M4 | 2 | 52.8 | 0.4 | 56.8 | SL | - | |
| 2M5 | 2 | 52.8 | 0.5 | 56.8 | SL | - | |
| 2M6 (L2) | 2 | 52.8 | 0.6 | 56.8 | SL | - | |
| 2M7 | 2 | 52.8 | 0.7 | 56.8 | SL | - | |
| 2M8 | 2 | 52.8 | 0.8 | 56.8 | SL | - | |
| H1 | 1 | 23.2 | 0.6 | 86.3 | NO | - | |
| H2 | 2 | 58.4 | 0.6 | 68.5 | SL | - | |
| H3 | 3 | 84.9 | 0.6 | 70.6 | M | - | |
| H4 | 4 | 116.7 | 0.6 | 68.5 | W | 0.063 | |
| LG6a | 6 | 45.18 | 0.6 | 58.57 | NO | - | |
| LG6b | 6 | 90.36 | 0.6 | 29.28 | SL | - | |
| LG8 | 8 | 60.24 | 0.6 | 58.57 | NO | - | |
| TK4a | 4 | 30.12 | 0.6 | 58.6 | NO | - | |
| TK4b | 4 | 60.24 | 0.6 | 58.8 | SL | - | |
| TK4c | 4 | 75.30 | 0.6 | 58.8 | M | - | |
| TK4d (L4) | 4 | 102.1 | 0.6 | 58.8 | W | 0.064 | |
| R4a | 4 | 86.06 | 0.6 | 45.8 | SL | - | |
| R4b (TK4b) | 4 | 60.24 | 0.6 | 58.8 | SL | - | |
| R4c | 4 | 74.55 | 0.6 | 80.5 | W | 0.063 | |

Table 3.1: Parameters for the different computer runs. Abbreviations for modes are: NO = No oscillations, SL = Shear Layer, W = Wake, M = Mixed. Strouhal numbers of vortex shedding (based on cavity depth and freestream velocity) are given for wake mode runs, and the computed drag coefficient is given for run series L (see section 3.3).

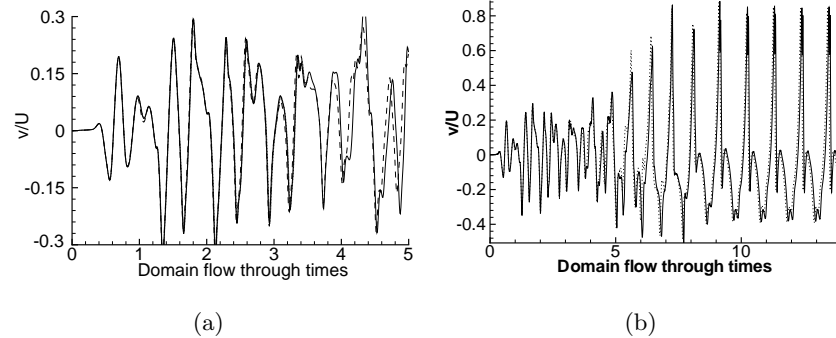


Figure 3.2: Effect of boundary position and grid resolution on the normal velocity at $y = 0$ and $x = 3.13D$. (a) shows reference case L4 (—) compared with a finer grid case (---) and larger domain case (····); (b) shows only the larger domain case, for longer time. Reference case L4 has downstream boundary: $10.6D$, upstream: $-4.3D$, normal: $9.2D$. Grid has 1152×384 points above the cavity in the streamwise and spanwise directions, respectively, and 384×94 points in the cavity. Finer grid case has same boundaries as run L4, but 50% more grid points (in each direction). Larger domain case extends to $15D$ downstream and $15D$ in the normal direction. Note that the dotted line falls nearly directly on top of the solid line in (a).

$3.13D$, $y = 0$), for different grid resolutions and boundary locations, but otherwise using the same parameters as run L4. Other probe locations yielded similar results. Note that time is normalized by the freestream velocity and the total length of the computational domain for the reference case. The larger-domain case is run for longer than the finer-grid case, as the domain size is more likely to cause low frequency errors, arising from nonphysical reflections at boundaries. Figure 3.3 shows a similar test for run L2, and the spectra are compared.

Over 3 to 4 flow-through times, the results are nearly identical, independent of grid resolution and boundary location. Small differences are apparent at later times, which is not unexpected given the sensitive dependence on initial conditions. For run L2, greater differences are observed after about 10 flow-through times, but the spectra are almost identical. We conclude that the boundary locations and grid resolutions for runs L2 and L4 are adequate, and similar locations and resolutions were used in the other runs in table 3.1.

3.2 Shear-layer mode

The shear-layer mode is characterized by the feedback process described in the introduction: the roll-up of vorticity in the shear layer, impingement and scattering of acoustic waves at the downstream cavity edge, upstream acoustic wave propagation, and receptivity of the shear layer to acoustic disturbances. The

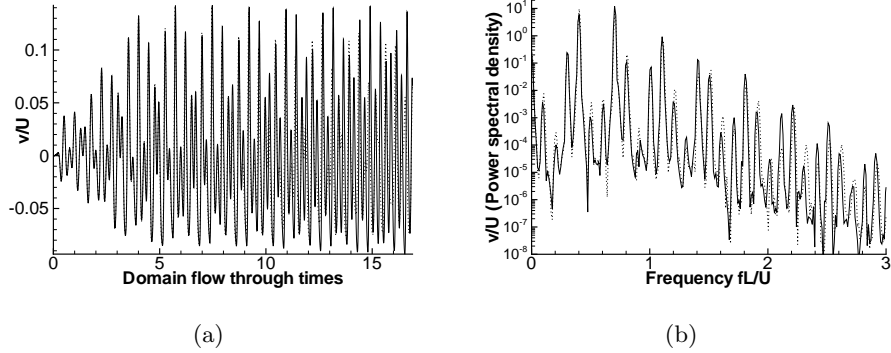


Figure 3.3: Effect of boundary placement on the normal velocity at $y = 0$ and $x = 1.57D$, for run L2. (a) shows the time trace for the reference case (—) and for a larger domain case (····); (b) shows the spectra of the data in (a). Reference case L2 has downstream boundary $7.6D$, upstream: $-3.9D$, normal: $9.2D$. Grid has 1008×384 gridpoints above the cavity, and 240×96 gridpoints in the cavity. Larger domain case extends to $11.8D$ downstream and $15.6D$ in the normal direction.

process is clearly born out by the computational results. Figure 3.4 shows vorticity contours at three different times for run L2, and these are indicative of all the runs in shear-layer mode of oscillation. Vortical disturbances propagate and grow along the shear layer, while the flow inside the cavity is relatively quiescent. A weak, relatively steady vortex occupies the downstream half of the cavity, as found by Roshko [1955]. The steady vortex induces vorticity of the opposite sign (to boundary-layer vorticity) along the cavity walls. The steadiness of the vortex suggests that the interaction of the flow inside the cavity with the shear layer is relatively weak. The shear layer will be examined in more detail in sections 3.2.3 and 3.2.4.

3.2.1 Acoustic field

In general, it is not possible to distinguish objectively between acoustic and hydrodynamic fluctuations in a complex, vortical flow. In this section, we examine the *acoustic field* produced by the cavity, where we loosely define the acoustic field as the irrotational field generated as vorticity is swept past the trailing corner of the cavity. For very low Mach numbers, these disturbances are essentially incompressible, and the propagation speed becomes arbitrarily large as the Mach number goes to zero. Here we consider Mach numbers from 0.2 to 0.8, and simply refer to the scattered field as “acoustic.”

The density fluctuations produced by the self-sustained oscillations is shown in figure 3.5, where we compare the present results to schlieren photographs taken by Krishnamurty [1956] for Mach numbers 0.64, 0.7, and 0.8, and $L/D = 2$. The experimental conditions are similar, in that the incoming boundary layer is lami-

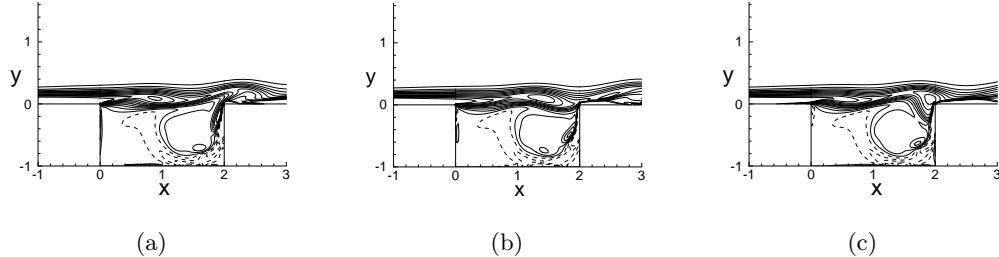


Figure 3.4: Instantaneous vorticity contours for run L2 (shear-layer mode) at 3 different times (a–c), corresponding to approximately one-third phase intervals of the dominant mode of oscillation (2nd Rossiter mode). 15 equi-spaced contours between $\omega D/U = -5$ and 1.67 are shown; positive contours are dashed. Only a small portion of the computational domain near the cavity is shown.

nar, but the Reynolds number in the experiment is higher by a factor of about 5. The cavity in the experiment had a transverse width of 4 inches, compared to the depth of 0.1 inch, and it is expected under these conditions that the instabilities are approximately two-dimensional. There is a very good qualitative agreement between experiment and computation. The greyscale contour levels in the simulation were chosen to provide the best visual comparison with the experiment. Note from the figure that the frequencies of oscillation (and hence wavelength of the acoustic field) are quite close at $M = 0.7$ and $M = 0.8$. At $M = 0.6$ (0.64 for the experiment), it appears that the frequency of oscillation is substantially lower in the simulation, and the experiment at these conditions is dominated by Rossiter mode 2 while the computation is dominated by Rossiter mode 1 (see section 3.2.2).

Also note from figure 3.5 that the radiation is intense enough that there is significant steepening of the compressions as the waves propagate, especially at the higher Mach numbers.

Figure 3.6 shows the sound pressure levels (SPL) for the acoustic field above the cavity, for $M = 0.6$. The maximum SPL is very high, about 180 dB, at a point near the downstream edge, and peak radiation to the far field occurs at an angle of about 135 degrees from the flow direction. In this direction, sound pressure levels still reach 170 dB at a distance of 3 cavity depths. These numbers are quite high, but Krishnamurty [1956] estimated sound pressure levels for the case of laminar boundary layers in excess of 163 dB for a variety of geometries. These estimates were based on deflections from finite-fringe interferometry, but no detailed mapping to SPL was performed. Krishnamurty [1956] found that flows with laminar boundary layers produce higher SPLs than flows with turbulent boundary layers, and that the $L/D = 2$ cavity was louder than longer cavities.

Figure 3.7 illustrates the separate contributions to the acoustic field, when two resonant frequencies are present simultaneously. Density fluctuations are plotted for run L2, which has two strong resonant frequencies, at $St = fL/U = 0.4$ and 0.7.

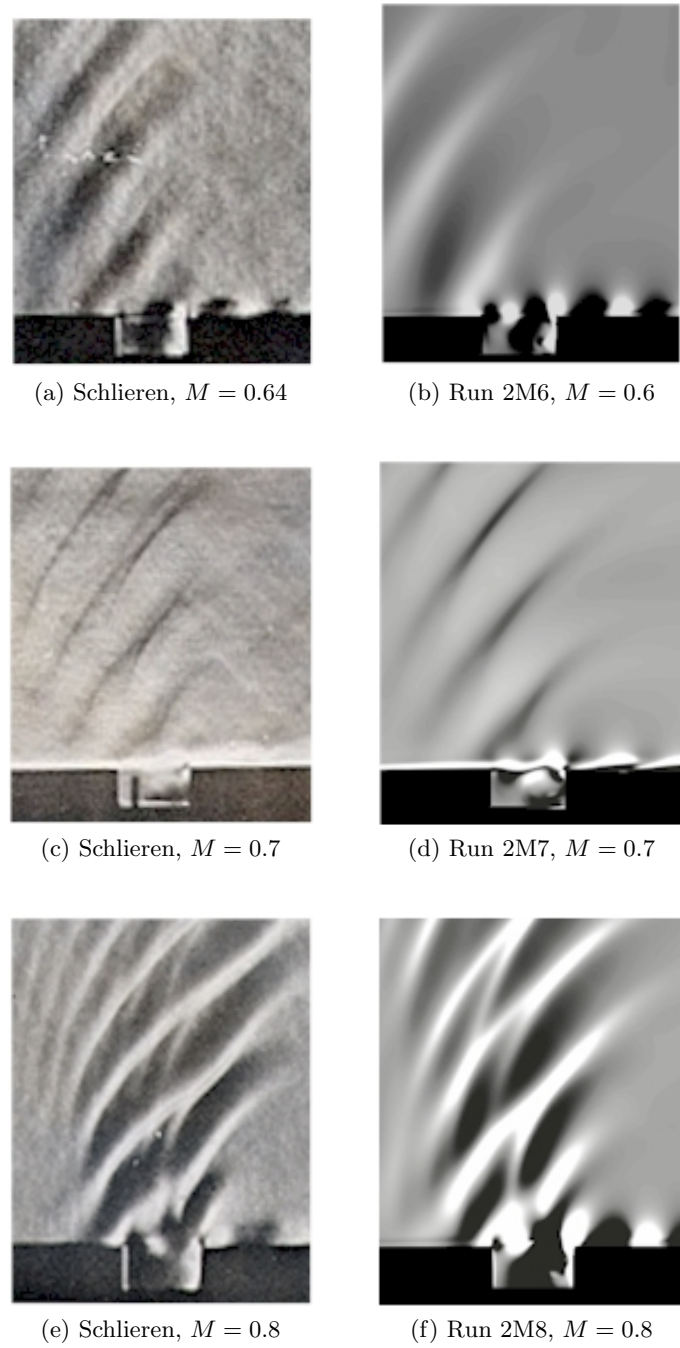


Figure 3.5: Comparison of schlieren photographs [Krishnamurty, 1956] with contours of density gradient from the DNS. In the schlieren photographs, the knife edge is horizontal in (c), vertical in the others; in the DNS figures, $\partial\rho/\partial y$ is shown in (d), $\partial\rho/\partial x$ in the others.

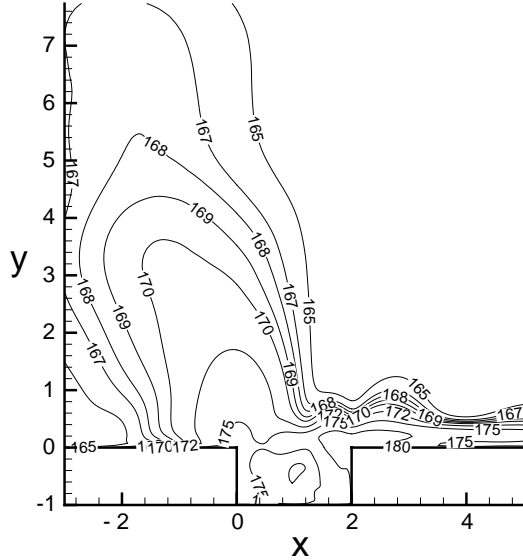


Figure 3.6: Sound pressure level (SPL) for run L2.

We performed a Discrete Fourier Transform (DFT) of 125 samples (every 250 time units) of the computational data over a period of time $TU/L = 30$, corresponding to 12 periods of the lower frequency, and 21 periods of the higher frequency. The resulting data record is approximately periodic in time, and the data is detrended prior to taking the DFT. We experimented with different windowing techniques, signal durations, and sampling rates, and we believe the results presented here are free from any artifacts of the limited signal duration and relatively low sampling rate.

Real and imaginary parts of the DFT are plotted, and the different wavelengths of farfield acoustic radiation are apparent. Hydrodynamic disturbances in the shear layer are also evident, and will be discussed further in section 3.2.4. It is striking that the level of the density fluctuations in the farfield is comparable to the level of the density fluctuations in the shear layer. This indicates the high efficiency of the acoustic scattering process at the cavity trailing edge. The wavelength of the acoustic fields at differing angles agrees with the predicted value based on the frequency of oscillation and the speed of the wavefront, $a_\infty(1 + M \cos \theta)$, where θ is the angle of the wave propagation direction measured from downstream x -axis, and a_∞ is the ambient sound speed.

3.2.2 Frequencies of oscillation

Figure 3.8 shows the spectrum of normal velocity at a point along the shear layer, at $y = 0$, $x/L = 0.783$, for a $L/D = 2$ cavity with $M = 0.7$ (run 2M7), which is oscillating in shear-layer mode. Several distinct peaks and their harmonics are evident. The frequencies labeled ‘‘Mode I, II’’ correspond to the first two

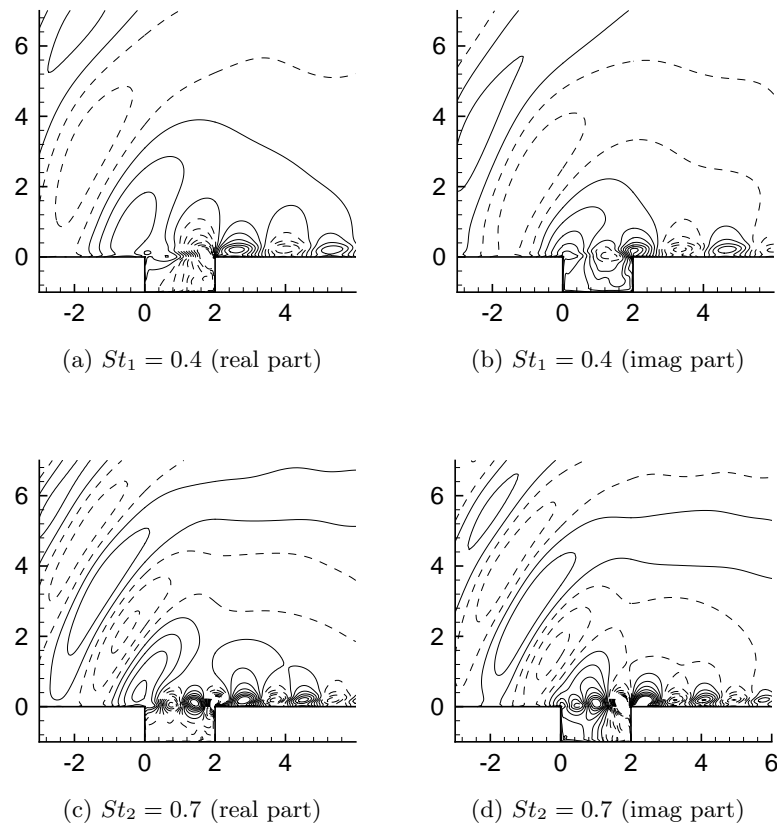


Figure 3.7: Contours of the DFT of the density at the two resonant frequencies for run L2. (a,b) 16 levels between $\pm 0.008\rho_\infty$; (c,d) 16 levels between $\pm 0.004\rho_\infty$; negative contours are dashed.

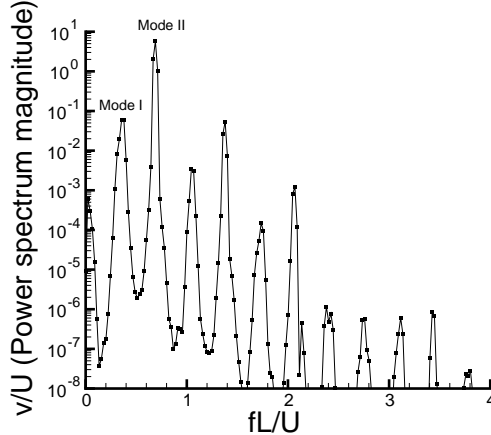


Figure 3.8: Spectrum of normal velocity at $y = 0$ and $x = 1.57D$, for run 2M7.

frequencies predicted by Rossiter's semi-empirical formula

$$St_n = \frac{f_n L}{U} = \frac{n - \gamma}{M + 1/\kappa}, \quad n = 1, 2, \dots, \quad (3.2)$$

where St_n is the Strouhal number corresponding to the n th mode frequency f_n , and κ and γ are empirical constants corresponding to the average convection speed of disturbances in the shear layer, and a phase delay. The other peaks in figure 3.8 are either harmonics or nonlinear interactions between the Rossiter modes.

In figure 3.9, the frequencies of the two most energetic peaks in the spectra for the series of runs 2M with $L/D = 2$ and $L/\theta_0 = 52.8$ and 4M with $L/D = 4$ and $L/\theta_0 = 102$ are compared to experimental data and predictions from equation (3.2), with $\gamma = 0.25$ and $\kappa = 1/1.75$, the original values used by Rossiter. The conditions in Krishnamurty's 1956 experiments are closest to those in our simulations, in that the upstream boundary layers were laminar, but the Reynolds number is five times larger than that in our simulations. Krishnamurty found only Mode II oscillations, and the frequencies are slightly higher than those measured in our simulations. Sarohia [1975] found in his experiments in water that the frequency increases with Reynolds number. He observed both Modes I and II, as shown in the figure, and it appears that the frequencies for higher Mach numbers would agree well with Sarohia's, when extrapolated to $M = 0$. For turbulent boundary layers, the frequencies are lower than for laminar boundary layers, as shown in the figure, and as noted previously by both Krishnamurty and Sarohia.

Note that there is quite a bit of scatter in the experimental data at low Mach numbers. In general, the data from experiments in water are fairly consistent [Sarohia, 1975; Knisely & Rockwell, 1982], but experiments in air at low Mach numbers have more scatter [Tam & Block, 1978; Rockwell & Schachenmann, 1982; Ahuja & Mendoza, 1995], because the frequencies of the resonant acoustic modes of the cavity become comparable to the Rossiter frequencies.

Peaks in the spectra corresponding to harmonics and sum and difference modes

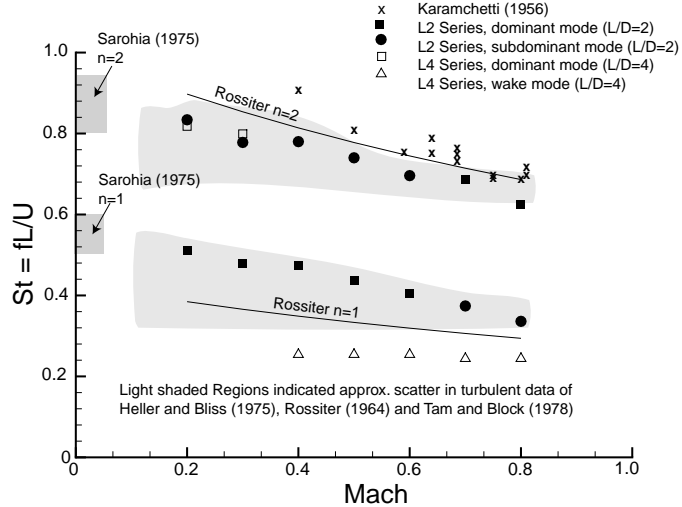


Figure 3.9: Strouhal numbers for peaks in spectra for the 2M series of runs (shear-layer mode), and 4M series (shear-layer and wake modes) compared to experiment and equation (3.2).

(primarily harmonics of $n = 1$ and the sum of Rossiter modes $n = 1$ and $n = 2$) were also detected in the data. Such nonlinear interactions between modes were studied by Knisely & Rockwell [1982] for incompressible cavity flow, and more recently by Cattafesta et al. [1998] for moderate subsonic speeds, with turbulent upstream boundary layers. These studies used bicoherence analysis and other sophisticated signal processing tools that rely on long time series of data. For the spectra obtained here, signal durations were relatively short, on the order of 20–100 times the lowest frequency peak in the data, so it was difficult to detect the presence of any mode switching, as was found to occur over long times by Cattafesta et al. [1998]. In the computations, it appears that the two primary Rossiter modes ($n = 1, 2$) were coexistent.

Finally, we note that in figure 3.9, oscillation frequencies from the 4M series of modes show the transition to wake mode oscillations for $M > 0.3$. These data are discussed more fully in section 3.3.

3.2.3 Shear-layer spreading rate

The shear layer spanning a cavity differs from a mixing layer in two main respects: Kelvin-Helmholtz instabilities are constantly being excited by the intense acoustic environment, and the entrainment is modified by the presence of the cavity. Despite these differences, most researchers report that shear layers over cavities closely resemble turbulent free shear layers, in that the spreading rate is approximately linear. However, there is some discrepancy as to the actual value of the spreading rate.

Here, we use the vorticity thickness δ_ω , defined in section 2.2, as a measure of

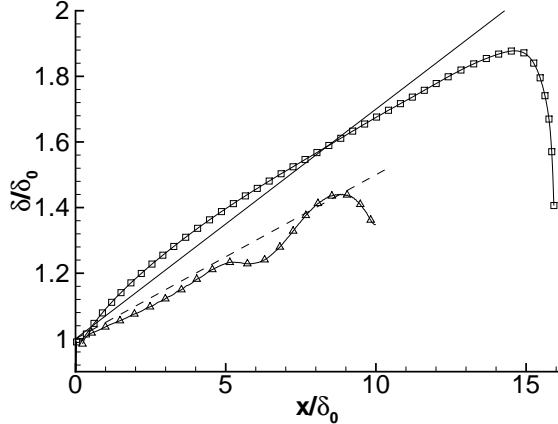


Figure 3.10: Vorticity thickness δ_ω along the shear layer for runs L2 (Δ) and LG6b (\square), and linear fits with slope $d\delta_\omega/dx = 0.05$ (---) and 0.07 (—).

the shear-layer thickness. It is common to use the momentum thickness θ (also defined in sec 2.2), but the momentum thickness shows significant variation caused by the recirculating region in the downstream portion of the cavity. The vorticity thickness is a local measure of the maximum shear, which better determines instability properties of the shear layer, and so it is the thickness we choose.

Sarohia [1975] appears to have been the first to measure the spreading rate in detail, and found that the spreading was approximately linear, and the spreading rate increased as L/θ_0 increased. As L/θ_0 increased from 52.5 to 105.2, with Re_θ and D/θ_0 held constant, the spreading rate $d\delta_\omega/dx$ varied from 0.025 to 0.088. These values are significantly lower than typical values for turbulent free shear layers, generally accepted to be around $d\delta_\omega/dx \approx 0.162$ [Brown & Roshko, 1974]. The upstream boundary layers in Sarohia's experiments were laminar. Gharib & Roshko [1987] also found linear growth of the shear layer, and found that the spreading rate was fairly constant at $d\delta_\omega/dx = 0.124^1$ for cavities with $L/\theta_0 > 103$. This indicates a spreading rate much closer to that of a turbulent free shear layer. The recent low Mach number experiments of Cattafesta et al. [1997] also exhibit linear spreading, with turbulent upstream boundary layers. Though the spreading rate is not stated, they report that for a cavity with $L/\theta_0 = 328$, the spreading rate closely matches that of a turbulent free shear layer, but for a cavity with $L/\theta_0 = 81$, the spreading rate is 50% *higher*, the opposite trend of that observed by Sarohia.

Shear-layer thicknesses from two of our runs are plotted in figure 3.10. Our data also indicate approximately linear growth, with spreading rates similar to those measured by Sarohia. Our run L2 ($L/\theta_0 = 53$) has a spreading rate of about $d\delta_\omega/dx = 0.05$, while Sarohia's experiments had $d\delta_\omega/dx = 0.056$ for $L/\theta_0 = 60$. Our spreading rates also increase with L/θ_0 , and for run LG6b ($L/\theta_0 = 90$) we

¹Where thicknesses are given in terms of momentum thickness θ , we set $\delta_\omega = 4\theta$, which is exact for a hyperbolic tangent profile.

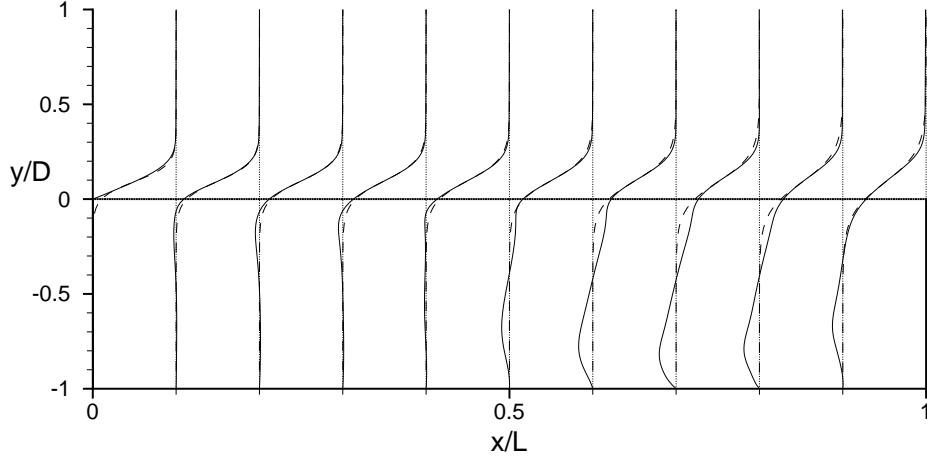


Figure 3.11: Mean streamwise velocity profile, $\bar{u}(x, y)/U$, for run L2 (—) compared to the hyperbolic tangent profiles with the same vorticity thickness (---).

measure $d\delta_\omega/dx = 0.07$, compared to an experiment of Sarohia's with $L/\theta_0 = 85$ and $d\delta_\omega/dx = 0.064$. Thus, our measurements support the trend noted by Sarohia, that the shear layer spreads faster for longer cavities. A likely reason for this trend is that a longer shear layer amplifies disturbances more, so the final amplitude of oscillations is larger, thus increasing Reynolds stresses, which cause the spreading.

3.2.4 Convection and amplification by the shear layer

In this section, we examine how disturbances are convected and amplified by the shear layer, and we compare the DNS results to those predicted by linear stability theory. The linear stability calculations are performed as described in chapter 2. We note that previous analyses (e.g., Tam & Block [1978]) did not account for the cavity bottom, as the cavity was assumed infinitely deep compared to the shear layer thickness.

We use the simulations to determine the mean flow for the linear stability calculations. Two different calculations are performed, one using the actual velocity profiles from the DNS, and another using hyperbolic tangent profiles with the same vorticity thickness and deflection. As shown in figure 3.11, the agreement is good close to the cavity leading edge, but much worse near the rear of the cavity, where the steady captive vortex is present. The actual DNS velocity profiles will of course be more accurate, but the tanh-profile linear stability calculations as a predictive tool to predict the total amplification by the shear layer.

The overall magnitude and phase of the instability wave is found by integrating

the complex growth rate α over the streamwise positions:

$$\tilde{f}(x, y) = \hat{f}(y) \exp\left(i \int_0^x \alpha \, dx\right), \quad (3.3)$$

where both the wavenumber α and the eigenfunction \hat{f} are slowly varying functions of x . Without carrying the analysis to higher order, the normalization of the eigenfunctions is arbitrary, and we have set the maximum amplitude of the normal velocity mode to unity at each axial position.

Figure 3.12 shows the normal velocity instability waves \tilde{v} , at the two resonant frequencies present in run L2 ($St = 0.4$ and 0.7), using the mean flow from the same run. Also shown is the DFT of the normal velocity, computed as described in section 3.2.1.

The linear stability eigenfunctions are seen to be in very good qualitative agreement with the Kelvin-Helmholtz instability waves at the corresponding frequencies, except very near the cavity trailing edge, where the DNS results show some of the disturbances being swept down into the cavity by the (nearly steady) vortex that occupies the downstream half of the cavity.

A more quantitative measurement of the phase variation is presented in figure 3.13. The phase of vorticity disturbances in the shear layer is plotted, again for run L2, at the two resonant frequencies. (This is just the phase of the DFT of vorticity, along $y = 0$.) Also plotted is the phase of the dilatation close to the cavity floor, which represents the upstream-traveling acoustic wave inside the cavity. These variables were chosen to better separate hydrodynamic disturbances from acoustic disturbances, though very similar results were obtained when normal velocity and pressure were used in the shear layer and cavity floor, respectively. The dilatation phase is relatively constant in the y -direction, except near the shear layer, where the hydrodynamic fluctuations are significant. Notice that the total phase variation from the shear-layer convection (downstream) and acoustic propagation (upstream) is almost exactly $2\pi n$, where n is the index of the Rossiter mode. This phase criterion is similar to that found in several experiments [Knisely & Rockwell, 1982; Rockwell & Schachenmann, 1982; Gharib & Roshko, 1987], which show that in the low Mach number limit, the total phase variation in the shear layer alone is a multiple of 2π . In this limit, the acoustic propagation is of course instantaneous, so for our compressible simulations we must add the phase variation of the finite-speed acoustic propagation. Note that the phase speed of the acoustic waves along the cavity bottom is far from constant. This indicates the presence of multiple acoustic reflections by the cavity walls.

Linear stability predictions for the phase variation in the shear layer are also plotted, and the phase variation is well predicted except for very near the leading and trailing edges of the cavity, where the DNS data show a slower phase speed (steeper phase variation). We do not expect the linear stability calculations to be very accurate in these regions, because the flow is rapidly changing in the streamwise direction, and significantly non-parallel at the downstream corner. In addition, any flow/acoustic coupling will be most important near the cavity cor-

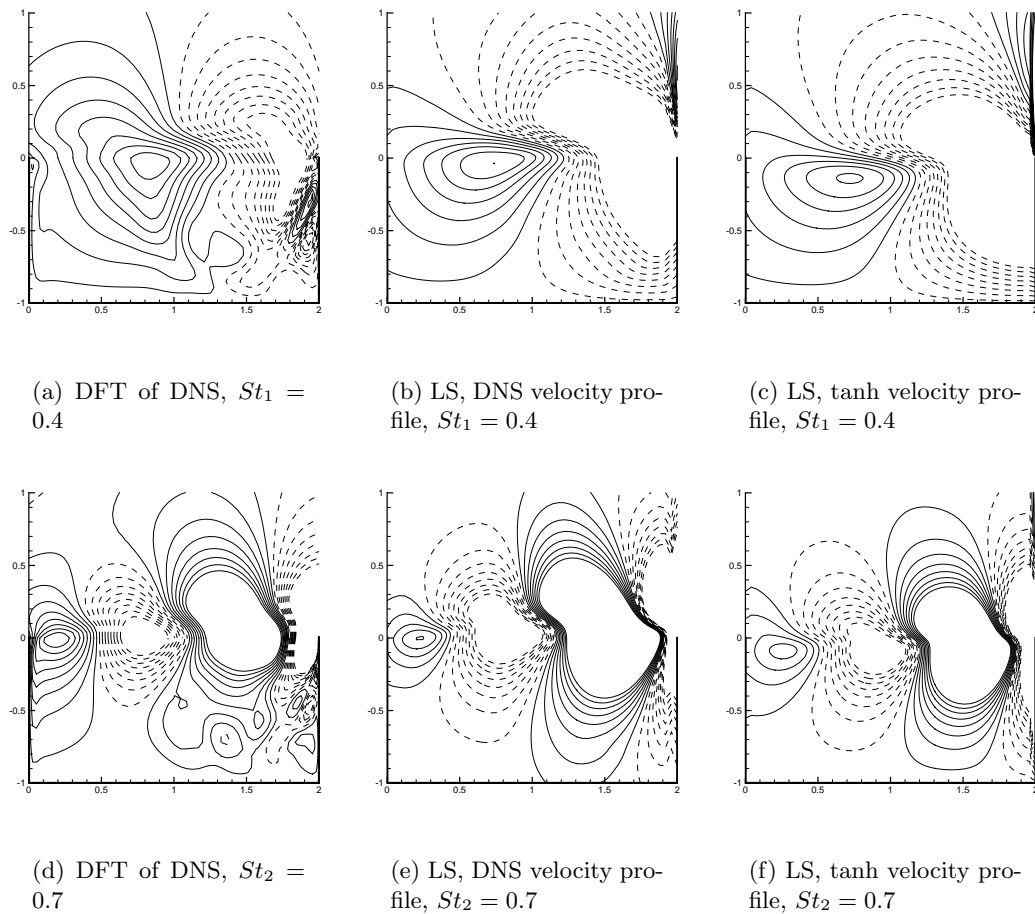


Figure 3.12: Comparison of mode shapes (real part) for normal velocity fluctuations in the shear-layer region for parameters of run L2. Contours are between $\pm 0.01U$ for (a–c), between $\pm 0.005U$ for (d–f).

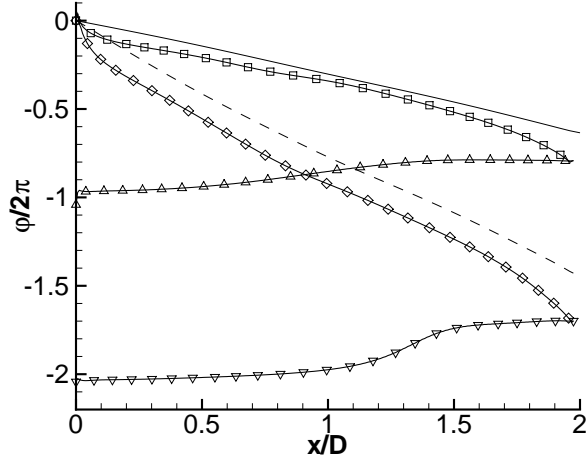


Figure 3.13: Phase of vortical and acoustic disturbances for run L2, at the frequencies of first two Rossiter modes ($St = 0.4, 0.7$). Vorticity disturbances in the shear layer at $y = 0$ (\square, \diamond); dilatation along cavity bottom at $y = -0.99D$ (\triangle, ∇); and shear-layer phase predicted by linear stability (—,---). Dilatation phase is shifted to line up with vorticity phase at $x = L$.

ners, where the receptivity to acoustic disturbances is high. These effects have been studied in detail by Rockwell & Schachenmann [1982].

Recall that Rossiter's formula for the resonant frequencies includes an empirical constant (γ in equation (3.2)) that represents an additional phase lag somewhere in the feedback loop. It is possible that the steeper phase variation exhibited near the leading and trailing edges of the cavity is the cause of this additional phase variation. The average phase speed from the DNS data is $c_p/U = 0.49$ for $St = 0.4$ and $c_p/U = 0.41$ for $St = 0.7$, while the linear stability calculations predict phase speeds of 0.63 and 0.49 for $St = 0.4, 0.7$.

Figure 3.14 shows the amplitude of normal velocity disturbances in the shear layer. The measured growth rates are significantly smaller than those predicted by the linear theory, which is surprising, because several experiments show the amplitude is well predicted, at least for moderate values of x/θ . Knisely & Rockwell [1982] used a constant-thickness mean profile, and found that the amplitude matched the linear theory well, for $x/\theta_0 \leq 30$; Cattafesta et al. [1997] found good agreement for $x/\theta_0 \leq 60$, also using a constant-thickness mean profile. However, our Reynolds number is much smaller than that in either of these experiments, so presumably a viscous stability calculation would agree better.

In summary, linear stability theory gives reasonable predictions for the mode shapes of the resonant frequencies, and also the convection speeds of disturbances, but amplification rates are significantly over-predicted. The linear stability calculation was compressible, but inviscid, and locally parallel. Adding viscous effects,

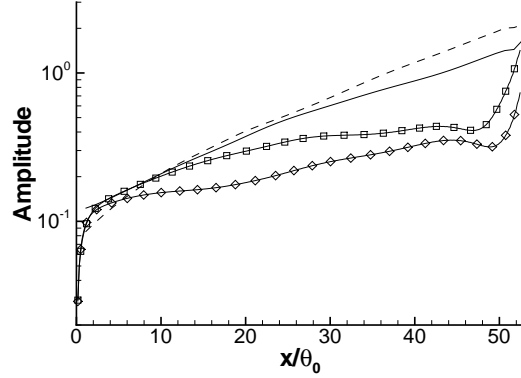


Figure 3.14: Amplitude of normal velocity fluctuations (run L2) along $y = 0$ at $St_1 = 0.4$ (\square) and $St_2 = 0.7$ (\diamond); and predictions from linear stability for St_1 (—) and St_2 (---).

including effects of flow/acoustic coupling, or carrying out a multiple scales analysis to account for slightly non-parallel effects [e.g., Crighton & Gaster, 1976] may provide a better agreement than is obtained here.

3.3 Wake mode

As the length or depth of the cavity (relative to the upstream boundary-layer thickness) and/or Mach and Reynolds numbers are increased, there is a substantial change in the behavior of the cavity oscillations. Under these conditions, the flow is characterized by a large scale shedding from the cavity leading edge. As noted in the introduction, Gharib & Roshko [1987] were the first to understand this transition in detail, and used the term *wake mode* to describe the resulting flow regime. Connections with the experiment are discussed further below.

3.3.1 Flow features

Figure 3.15 shows the general features of wake-mode oscillations. A vortex forms at the leading of the cavity, and grows until it is nearly the size of the cavity. As it is forming, irrotational free stream fluid is directed into the cavity, impinging on the cavity walls. Vorticity of the opposite sign (to that in the vortex and the upstream boundary layer) is generated between the large vortex and the upstream cavity wall. This opposite sign vorticity accumulates, and the large vortex is shed from the leading edge and ejected from the cavity in a violent event. The vortex is large enough to cause flow separation upstream of the cavity during its formation, and again in the boundary layer downstream of the cavity as it convects away.

Time traces of the normal velocity at a point in the shear layer ($y = 0$, $x = 3.13D$) are shown in figure 3.16, for the series of runs L1–L5, where L/θ_0 was varied, with constant D/θ_0 . For the shortest cavity (run L1, $L/\theta_0 = 20$), the flow is steady.

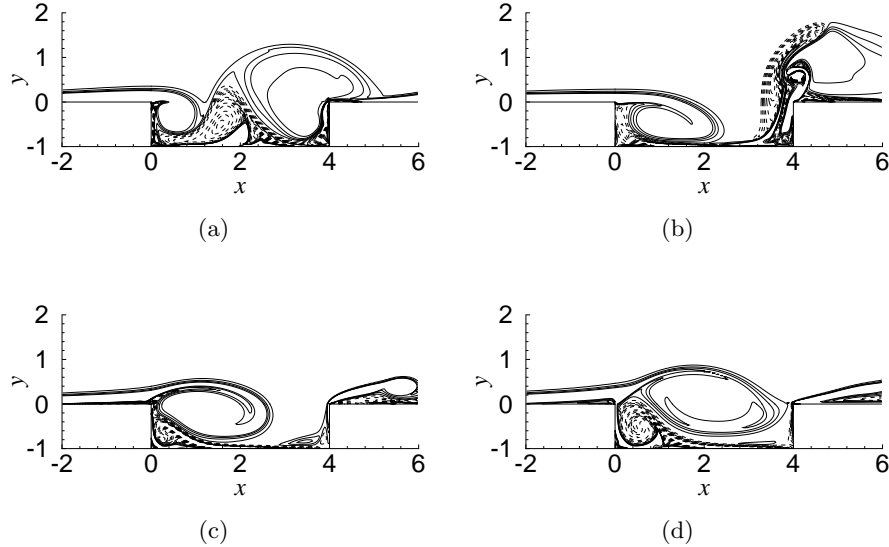


Figure 3.15: Instantaneous vorticity contours for run L4 (wake mode) at four different times (a–d), corresponding to approximately quarter phase intervals of the periodic cycle. 15 contours between $\omega D/U = -5$ and 1.67. Positive contours are dashed. Only a small portion of the computational domain near the cavity is shown.

For a longer cavity (run L2, $L/\theta_0 = 53$), shear-layer mode oscillations are evident, and as the cavity length increases further (runs L4, L5, $L/\theta_0 > 100$), the flow transitions into wake mode after a few oscillations in shear-layer mode. For run L3 ($L/\theta_0 = 75$) it appears that there is mode switching, with wake and shear-layer modes being present at different times (what we referred to in table 3.1 as *mixed mode*). The transition is also a function of Mach number, and for $L/\theta_0 = 102$, shear layer mode occurs for $M < 0.3$, and wake mode for $M > 0.3$. Time traces in the different regimes look similar to those in figure 3.16, and again indicated the presence of a mixed mode.

Figure 3.17 contrasts the time-averaged flow for runs L2 (shear-layer mode) and L4 (wake mode). The mean streamlines in wake mode are significantly deflected above the cavity, and show that on average, the boundary layer upstream of the cavity sees an adverse pressure gradient. On average the flow in the cavity is strongly recirculating, and there is an impingement of the recirculating flow on the rear wall. It is important to contrast the mean flow with the instantaneous visualizations of figure 3.15, which shows that, unlike in shear-layer mode, there is no stationary vortex within the cavity instantaneously. The region of high pressure near the back corner of the cavity resembles that observed by Fox [1965] in his high-drag flow regime. Variations in the average coefficient of pressure are also quite large, reaching a minimum of about -0.5 where the flow is expanding into the cavity, to about 0.3 in the impingement region on the rear step.

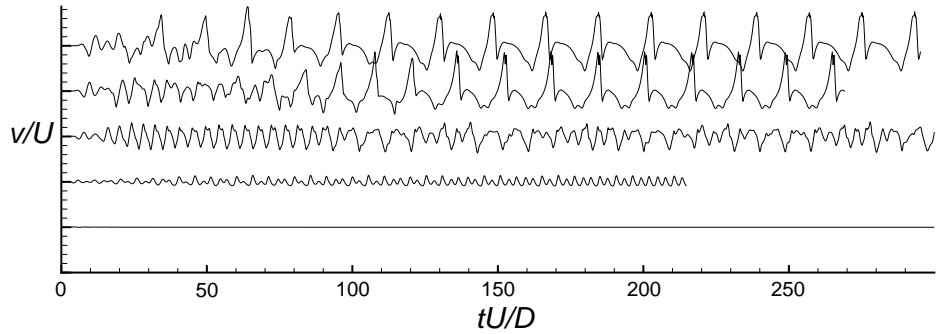


Figure 3.16: Time traces of the normal velocity, relative to U , at $y = 0$, $x = 3.13D$ for the series of runs L1–L5 (bottom to top). The vertical axes have been artificially shifted to show all the data clearly, with major tick marks representing 1 unit.

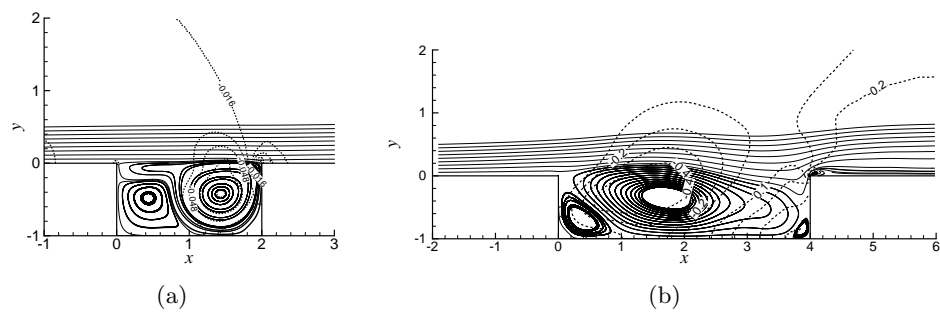


Figure 3.17: Time-averaged flow for (a) L2 (shear-layer mode), and (b) 4M6 (wake mode). Mean streamlines (solid lines) are superposed on contours of constant C_p (dashed lines).

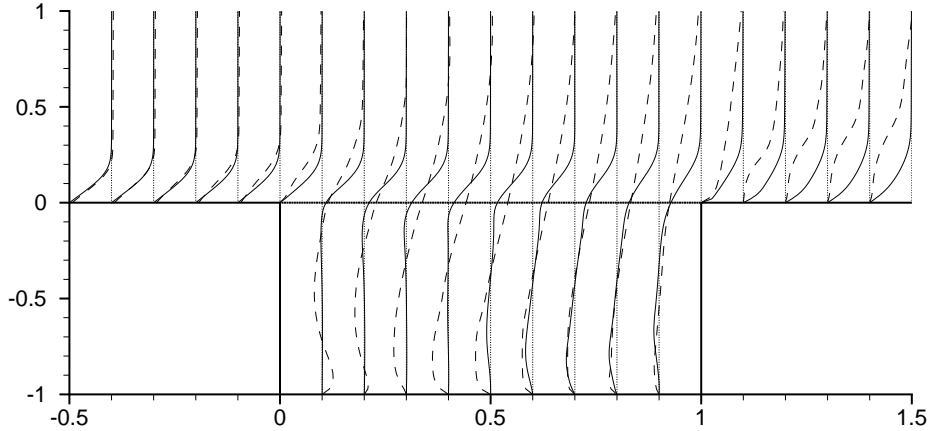


Figure 3.18: Mean streamwise velocity profiles, $\bar{u}(x, y)/U$, at different streamwise positions. Run L2 (—); Run L4 (---).

By contrast, the shear-layer mode shows much smaller pressure variations, and mean flow streamlines are nearly horizontal along the mouth of the cavity. The low pressures ($C_p \approx -0.08$) correspond to the center of the recirculation region that exists in the rear two-thirds of the cavity (see figure 3.4). The low pressure region appears to be the result of the vortical swirling motion in the cavity, and not because of an expansion of the flow into the cavity as was the case for wake mode. There is a very small impingement region at the rear edge, where C_p reaches about 0.1. However, over the majority of the rear face $C_p < 0$, which is consistent with the measurements of Roshko [1955] and others.

Similar flow features are also evident in the mean streamwise velocity profiles, shown in figure 3.18. Wake mode oscillations have a substantial effect on the mean even as far as 1–2 depths above the cavity, and also affect the upstream boundary layer, to about a quarter of a depth upstream. As we noted in section 3.1.2, the nominal momentum thickness that we use is that of the initial condition, and figure 3.18 shows that this is indeed substantially modified by the flow in wake mode. It is modified only by a very small amount in shear-layer mode.

In Gharib & Roshko [1987], transitions between non-oscillatory, shear-layer, and wake modes occurred at $L/\theta_0 = 80$ and $L/\theta_0 = 160$, respectively. The present data indicate a change from wake mode to shear-layer mode that depends also on the Mach number and Reynolds number. The specific parametric dependence of the transition to wake mode is discussed in section 3.3.3. The drag on the cavity (given for selected runs in table 3.1), is of comparable magnitude to the values reported by Gharib & Roshko [1987] for the different regimes. An impingement of the flow on the rear step was also noted in the experiments, and it also appears (see Figure 7(a) of Gharib & Roshko [1987]) from dye visualizations that the boundary layer separates upstream of the cavity leading edge.

3.3.2 Frequency of vortex shedding

The spectra of the resonant instabilities in wake mode are very different from those of the shear-layer mode (section 3.2.2). After an initial transient, which at early times is similar to shear-layer mode, the flow becomes nearly periodic in time, with the fundamental period corresponding to the vortex shedding from the leading edge (see figure 3.16). The spectrum (after the onset of wake mode) consists of a dominant frequency and strong peaks at its harmonics. The 4M series of runs transitioned from shear-layer to wake mode between $0.3 < M < 0.4$, and the peak frequencies were plotted in figure 3.9. For $M > 0.3$, the peaks fall well below the first Rossiter mode prediction, and, unlike the shear-layer mode, they show little variation with M . For $M = 0.4$ to $M = 0.8$ the fundamental frequency varied less than 4%, compared to the expected variation of about 20% for Rossiter Mode I. The 4% variation is, in fact, within the uncertainty associated with the total sampling period used to determine the frequency.

The lack of variation with M indicates that wake mode *is not a result of acoustic feedback*, and it appears that the feedback in this case is provided by the complicated recirculating flow in the cavity. This is discussed further in section 3.3.4.

3.3.3 Parametric dependence of the transition to wake mode

In table 3.1, we have indicated the dominant mode (steady flow, shear-layer mode, or wake mode) for the different runs, and, for the wake mode cases, the shedding frequency, *scaled with the cavity depth and freestream velocity*. Once established, the shedding frequencies in wake mode are all nearly the same for cavities with $L/D = 4$, meaning that, in addition to the invariance to Mach number noted above, they are not influenced by L/θ_0 or D/θ_0 . A lack of dependence of the shedding frequency on the boundary-layer thickness is a common feature of vortex shedding behind bluff bodies (for instance, for laminar flow over a cylinder, it is well known that the shedding frequency $St = fD/U$ is constant over a wide range of Reynolds numbers). We note that for the cavity with $L/D = 5$ (run L5), the shedding frequency is about 10% lower than that of the $L/D = 4$ runs, and that a periodic wake mode was not detected in any of the runs with $L/D = 3$ or smaller. Several of the $L/D = 3$ runs exhibited some characteristics of both shear-layer mode and wake mode.

While the wake mode typically occurs for larger L/θ_0 and D/θ_0 , the transition depends as well on the Mach and Reynolds numbers. For example the runs L4 and TK4b both have $L/D = 4$, but the latter is oscillating in shear-layer mode, as shown by the instantaneous vorticity fields plotted in figure 3.19, which should be contrasted to figure 3.15. Moreover, the transition to wake mode also depends on M , but it is interesting that, as previously noted, once wake mode is established the frequency of vortex shedding is nearly independent of M . The 4M series of runs shows transition to wake mode as the Mach number is increased, holding other parameters constant. The TK4 series of runs shows evidence of transition to

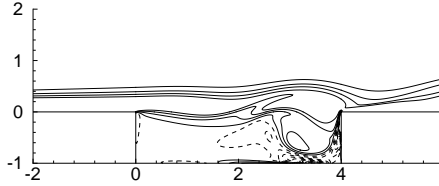


Figure 3.19: Instantaneous vorticity contours for run TK4b (shear-layer mode). Contour levels same as figure 3.15.

wake mode as the D/θ_0 is increased, holding L/D , M , and Re_θ nearly constant, and, finally, the R4 series shows transition with increasing Re_θ when L/D , M , and D/θ_0 are held nearly constant.

In all of the simulations that have been performed, examination of the instantaneous flow fields shows that the initial growth of instability is always in shear-layer mode, where acoustic radiation from the downstream edge is the mechanism for the feedback. The shear-layer oscillations, at early times, are growing in amplitude with each subsequent cycle, and the wake mode sets in only after the oscillations have reached a certain threshold. Thus it appears that the emergence of wake mode is determined by the conditions in shear-layer mode, and this forms the basis of our attempt below to model the parametric dependence of the wake mode. We note that we have not attempted to look for hysteresis in the transition to wake mode, as there is no unambiguous way to do so computationally.

3.3.4 Convective and absolute instability

As indicated above, the oscillation frequency in wake mode is independent of the Mach number, over a large range from $0.4 < M < 0.8$. This implies that, unlike the oscillations described by the Rossiter mechanism, wake mode oscillations are not acoustically forced convective instabilities. In wake mode, the flow exhibits several qualitative features of *absolutely unstable* parallel flows, as described in, e.g., Huerre & Monkewitz [1985], and this may provide an explanation of the governing mechanism.

The notion of absolute or convective instability is a useful tool for describing self-sustained oscillations in parallel shear flows. The idea is the following: given a certain parallel flow, if energy from a disturbance grows in time, but travels only downstream, the flow is called *convectively unstable*. In such flows, there is no possibility for self-sustained oscillations, since if the flow disturbance is removed, the oscillations convect away. However, if energy grows and travels upstream, then the flow is called *absolutely unstable*, and such flows have the potential for self-excitation. In this context, flows that exhibit self-sustained oscillations are called *globally unstable* [Huerre & Monkewitz, 1990]. This terminology is normally reserved for (nearly) parallel flows, however—non-parallel flows will normally not be steady solutions of the Navier-Stokes equations, so it does not make sense to

discuss their stability.

For cavity oscillations in shear-layer mode, the flow is nearly parallel, so these stability concepts apply directly. The established view of cavity oscillations in shear-layer mode is one of a *convective* Kelvin-Helmholtz instability in the shear layer, which leads to global instability through pressure feedback from acoustic waves generated near the trailing edge. Indeed, if $D/\theta_0 \gg 1$, so that the boundary condition at the cavity bottom may be neglected, and if flow within the cavity is relatively quiescent (such that the velocity ratio across the shear layer is approximately unity), then analysis shows that the shear layer is indeed (locally) convectively unstable [Huerre & Monkewitz, 1985]. The good prediction of oscillation frequencies by the Rossiter formula, and the computational confirmation given earlier (e.g., the results of section 3.2.4), confirm the feedback process leading to global instability.

In wake mode, the flow past the cavity is far from parallel, and the disturbances are far from small, so the notions of absolute and convective stability do not strictly apply. Nevertheless, these notions have been applied to very similar oscillating wake flows, such as the wake behind a cylinder, and the predictions of the theory have been shown to be in good agreement with experiment, despite these non-parallel, large-amplitude effects [Huerre & Monkewitz, 1990]. We therefore apply these ideas to the cavity flow in wake mode, even though the theoretical justification is questionable.

With these ideas in mind, the flow in wake mode is also globally unstable, since self-sustained oscillations persist despite no external forcing. However, since the frequency is independent of Mach number, the feedback mechanism is apparently no longer acoustic. It is therefore plausible that *absolute instability* provides the mechanism necessary for global instability.

The mean flow profiles shown in figure 3.18 show that in shear layer mode (run L2), there is very little backflow in the cavity, and furthermore the backflow is confined to a region at the rear of the cavity. By contrast, the wake mode profiles (run L4) reveal a substantial backflow even very close to the cavity leading edge. Huerre & Monkewitz [1985] have shown that for tanh profiles with greater than 13.6% backflow, the flow is absolutely unstable. The backflow in the mean profiles for run L4 reaches a maximum of over 38% of the freestream velocity near the center of the cavity, decreasing to about 21% within two boundary-layer thicknesses of the leading edge, and 15% within one boundary-layer thickness. The backflow for run L2 is much smaller, reaching a maximum of 23% of the freestream near the rear of the cavity, and never exceeding 3% of the freestream anywhere in the front 40% of the cavity. The mean profiles from run L4 are not well described by tanh profiles, but the main point is that there is significant backflow in the cavity, and in this sense the profiles are qualitatively similar to profiles which have been shown to be absolutely unstable. It is possible, then, that absolute instability may provide a mechanism for transition to wake mode. It is also conceivable that similar ideas to those expressed in Monkewitz & Nguyen [1987] might be used to predict the shedding frequency in wake mode.

3.4 Prediction of the oscillation regimes

Here we discuss a method of predicting transition between the various flow regimes: no oscillations, shear-layer mode, and wake mode. Our goal is not a quantitative prediction for the amplitude of oscillation, but rather an approximate scaling law to determine the parametric dependence of the transitions between the different regimes.

Our criteria for predicting transition to wake mode are based on the following observations: as certain parameters (e.g., L/θ_0) are increased, the Kelvin-Helmholtz disturbances in the shear layer grow to larger amplitude. The larger amplitude disturbances induce a larger recirculating flow within the cavity, possibly generating a region of absolute instability in the shear layer, and ultimately inducing large-scale vortex shedding from the leading edge. The key ideas here are that larger amplitude disturbances lead to larger back flow in the cavity, which ultimately leads to wake mode.

The onset of fluctuations (i.e., the transition from steady flow to shear-layer mode) demonstrates a similar dependence on the parameters of the problem, since the amplification by the shear layer must exceed a certain threshold for self-sustained oscillations to occur [Woolley & Karamcheti, 1974]. At low Mach number, Sarohia [1975] determined that there is a minimum cavity length, relative to the (laminar) incoming boundary-layer thickness, for which cavity oscillations may occur. For sufficiently large D/θ_0 ($D/\theta_0 > \sim 15$) he found oscillations only when

$$\sqrt{Re_\theta} L/\theta_0 > \sim 800, \quad (3.4)$$

which also shows that there is a minimum speed, a maximum viscosity, and a maximum boundary-layer thickness, holding other parameters constant, beyond which there are no oscillations. Gharib & Roshko [1987] also measured the onset of fluctuations at $\sqrt{Re_\theta} L/\theta_0 \approx 780$. As D/θ_0 was decreased below about 15, Sarohia [1975] found a rapid increase in the minimum length for oscillations to occur. The data for turbulent fluctuations and higher Mach numbers are not so complete, but the general trend is that the minimum length increases with turbulence [Krishnamurty, 1956; Sarohia, 1975], and decreases with increasing Mach number [Krishnamurty, 1956].

Thus, if the overall amplification of disturbances can be predicted, simple criteria for both the onset of fluctuations and the transition to wake mode would be that the amplification exceeds a certain value. In order to test this hypothesis, we estimate the amplification based on ideas about the shear-layer instability, and the efficiency of the acoustic radiation from the trailing edge. Although some of the approximations made are crude, our goal is to establish a rough parametric dependence of transitions between the flow regimes, rather than a detailed prediction for the overall amplitude.

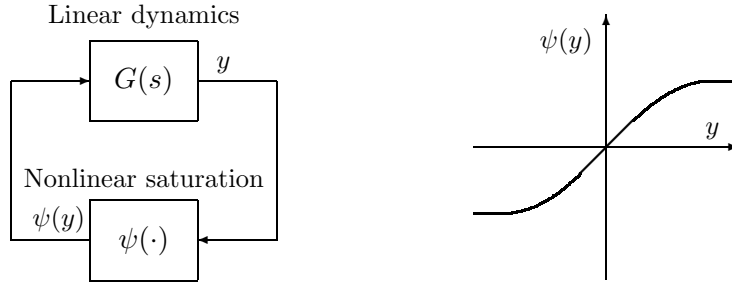


Figure 3.20: Simple model of nonlinearities.

3.4.1 The role of nonlinearities

All our analysis of the governing physical mechanisms will be linear. One might object at the outset that linear amplification rates say nothing about the final amplitude of a limit cycle—in fact, once the flow has settled into a limit cycle, the *loop gain* (total amplification once around the feedback loop) must be unity, regardless of the amplitude of the limit cycle (otherwise, oscillations would grow or decay). One must, in fact, take nonlinearities into account to predict amplitudes.

However, under simple yet reasonable assumptions about the nonlinearities present, the linear part of the loop gain defined above does predict both the onset of oscillations and the final amplitude of a limit cycle. Assume the system may be approximated (crudely) by linear dynamics coupled with a frequency-independent nonlinear saturation, as shown in figure 3.20. Here, $G(s)$ is the transfer function of the linear elements in the model (for our purposes, this will be the shear-layer amplification and scattering at the downstream corner), and $\psi(\cdot)$ is a *saturation nonlinearity*, defined precisely below. This form of the model lends itself to *describing function* analysis [e.g., Khalil, 1996], a simple tool for approximating both frequencies and amplitudes of limit cycles in nonlinear systems.

Describing functions

If y is periodic, of the form $y = A \sin \omega t$, then $\psi(y(t))$ will also be periodic, with the same frequency, and may be written as a Fourier series

$$\psi(y(t)) = \sum_{k=1}^{\infty} c_k(A) \sin k\omega t,$$

where we have assumed that ψ is odd. In the simplest form of describing function analysis, one neglects higher harmonics (assuming, for instance, that they will be attenuated by $G(s)$), and considers only $k = 1$, defining the *describing function*

$$N(A) = \frac{c_1(A)}{A} = \frac{2}{\pi A} \int_0^{\pi} \psi(A \sin t) \sin t dt. \quad (3.5)$$

Sinusoidal solutions $y = A \sin \omega t$ of the feedback loop must then satisfy $y = G(i\omega)\psi(y) \approx G(i\omega)N(A)y$, which gives the *harmonic balance* equation

$$G(i\omega)N(A) = 1. \quad (3.6)$$

For odd nonlinearities, $N(A)$ is real, and so taking the phase of this equation yields

$$\angle G(i\omega) = 0, \quad (3.7)$$

which determines possible frequencies of oscillation. (This is the same criterion used in Rossiter's model for the resonant frequencies.) Taking the magnitude of (3.6) gives

$$|G(i\omega)| = 1/N(A), \quad (3.8)$$

which determines the amplitude A of the limit cycle with frequency ω . Stability of the limit cycle may be addressed separately, using, for instance, Nyquist stability techniques.

The key assumption in the above discussion is that one may neglect higher harmonics ($k > 1$). For the cavity flow, the Kelvin-Helmholtz mechanism in the shear layer amplifies low frequencies, but attenuates higher frequencies, dropping off quite sharply as the frequency increases (see figure 6.7). Thus, the above assumptions are reasonable in the present context. Note that rigorous results are available, and one may rigorously prove existence (or non-existence) of limit cycles, if the linear part satisfies certain conditions [Khalil, 1996]. These conditions quantify how sharply the linear part must drop off as frequency increases. Here, since we do not know the precise nature of the nonlinearities, or quantitative information about the linear dynamics, we cannot directly verify these conditions, but they are not difficult to check, given a quantitative model.

Saturations

We now prove some properties of describing functions for *saturation nonlinearities*, defined as follows:

Definition 3.1 *An odd function ψ is a saturation nonlinearity if $\psi(y)/y$ is positive and decreasing for all $y > 0$, with $\psi(y)/y \rightarrow 0$ as $y \rightarrow \infty$.*

Note that $\psi(y)/y$ need not be *strictly* decreasing. We now demonstrate some properties of describing functions for this class of nonlinearities.

Proposition 3.1 *Let ψ be a saturation nonlinearity. Then its describing function N satisfies the following properties:*

1. $N(A) > 0$ for all $A > 0$.
2. $N(A) \rightarrow 0$ as $A \rightarrow \infty$.

3. $N(A) \rightarrow \psi'(0)$ as $A \rightarrow 0$.
4. $N(A)$ is decreasing for $A > 0$.

Proof: Property 1 follows directly from equation (3.5), since $\psi(y) > 0$ for $y > 0$, thus making the integrand positive for all t . Property 2 also follows from (3.5), since $\psi(y)/y \rightarrow 0$ as $y \rightarrow \infty$:

$$\begin{aligned}\lim_{A \rightarrow \infty} N(A) &= \lim_{A \rightarrow \infty} \frac{2}{\pi} \int_0^\pi \frac{\psi(A \sin t)}{A \sin t} \sin^2 t dt \\ &= \frac{2}{\pi} \int_0^\pi \lim_{A \rightarrow \infty} \frac{\psi(A \sin t)}{A \sin t} \sin^2 t dt \\ &= 0.\end{aligned}$$

The proof of property 3 is similar. Letting $K = \psi'(0) = \lim_{h \rightarrow 0} \psi(h)/h$, we have

$$\begin{aligned}\lim_{A \rightarrow 0} N(A) &= \lim_{A \rightarrow 0} \frac{2}{\pi} \int_0^\pi \frac{\psi(A \sin t)}{A \sin t} \sin^2 t dt \\ &= \frac{2}{\pi} \int_0^\pi K \sin^2 t dt \\ &= K.\end{aligned}$$

Property 4 uses that $\psi(y)/y$ is decreasing for $y > 0$. Let $A_1, A_2 \in \mathbb{R}$ with $0 < A_1 < A_2$. Then for $t \in (0, \pi)$,

$$\begin{aligned}A_2 \sin t &> A_1 \sin t > 0 \\ \implies \frac{\psi(A_2 \sin t)}{A_2 \sin t} &\leq \frac{\psi(A_1 \sin t)}{A_1 \sin t} \\ \implies \frac{\psi(A_2 \sin t)}{A_2} \sin t &\leq \frac{\psi(A_1 \sin t)}{A_1} \sin t \\ \implies \frac{2}{\pi A_2} \int_0^\pi \psi(A_2 \sin t) \sin t dt &\leq \frac{2}{\pi A_1} \int_0^\pi \psi(A_1 \sin t) \sin t dt \\ \implies N(A_2) &\leq N(A_1),\end{aligned}$$

and hence $N(A)$ is decreasing for $A > 0$. ■

These properties show that for saturation nonlinearities, the describing function $N(A)$ must have the general form depicted in figure 3.21.

The figure shows the amplitude A on the vertical axis, and the *reciprocal* of the describing function on the horizontal axis. Recall that a limit cycle with amplitude A must satisfy (3.8), so when the linear gain $|G(i\omega)| = 1/N(A)$, the amplitude of the limit cycle (as predicted by describing function analysis) is A , as indicated in the figure. The properties of saturation nonlinearities guarantee the qualitative features of the curve: specifically, it must always “bend to the right,” since $1/N(A)$ is an increasing function of A , and obviously the amplitude A can

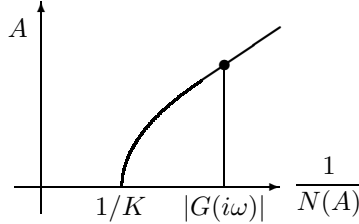


Figure 3.21: Describing function $N(A)$ for a saturation nonlinearity $\psi(\cdot)$. Here $K = \psi'(0)$, the gain of $\psi(\cdot)$ for small amplitudes.

never decrease if $|G(i\omega)|$ increases. (Otherwise, $N(A)$ would have to be multiple-valued.) Stability of the limit cycle must be addressed separately, but the standard argument based on the Nyquist criterion (see Khalil [1996]) shows that, as long as the approximations in describing function analysis are valid, the limit cycle is stable.

Application to cavity oscillations

Without knowing details of the nonlinearity and exact values for $G(i\omega)$, we cannot predict the exact value of the amplitude. But if we obtain scaling laws for $G(i\omega)$, the amplitude will follow (at least qualitatively) the same scaling laws: for $|G(i\omega)|$ below a certain threshold, we expect no oscillations to occur, and for $|G(i\omega)|$ above this threshold, we expect a stable limit cycle whose amplitude increases with $|G(i\omega)|$.

The precise way in which nonlinearities enter into the physics is still not clearly understood. One scenario, most likely to occur for short cavities (small L/θ_0), is that employed by Cain et al. [1996], where the saturation occurs because of spreading of the shear layer: the spreading of the mean flow is caused by Reynolds stresses that are proportional to the square of the amplitude of the oscillations, plus any background turbulence or other nonlinear interactions between the modes, as described by Morris et al. [1990]. Linear growth rates of the Kelvin-Helmholtz instability waves decrease as the shear layer spreads, and eventually become negative for very thick shear layers, thus providing a saturation mechanism. For this mechanism, then, the shear-layer disturbances are well described by linear methods, given the correct shear-layer thickness. Our data in section 3.2.4 are consistent with this, as shown by the good agreement of the data with linear predictions (see figure 3.12). Though the amplification predicted by linear theory does not agree well (figure 3.14), this is more likely because of viscous effects, rather than nonlinear effects, because there is disagreement even for small x/θ_0 .

The saturation mechanism more commonly considered is that once the oscillations grow large, the linearization is no longer valid, and the resulting nonlinear effects limit the growth. This effect is most likely for longer shear layers (large L/θ_0), as in the experiments of Cattafesta et al. [1997], which had a very thin upstream boundary layer ($L/\theta_0 = 328$). Knisely & Rockwell [1982] also attributed their saturation to this mechanism, although it is also plausible that the saturation

might be explained by mean flow spreading, as the linear stability calculation they compared to had a constant-thickness shear profile.

Both of these forms of nonlinearities fit nicely into the describing function framework described above: if a shear-layer disturbance at the leading edge is given by $f(0, t) = A \exp(i\omega t) + c.c.$, then at a distance x downstream, the amplified disturbance is approximately described by

$$f(x, t) = N_x(A) A \exp(i\omega t) \cdot G_x(i\omega) + c.c., \quad (3.9)$$

where $G_x(i\omega)$ is the linear gain and phase at location x (for instance, $G_x(i\omega) = \exp(i\alpha(\omega)x)$), and $N_x(A)$ is a nonlinear saturation, equal to unity for small A , and decreasing for large A , and also depending on the position x . Thus, $N_x(A)$ in (3.9) plays the same role as the describing function above, and similar conclusions about the stability and amplitude of the limit cycle follow.

3.4.2 Shear layer

The shear-layer amplification is a complicated function of M , L/θ_0 , D/θ_0 , and Re_θ . To proceed, we perform inviscid linear stability calculations similar to those described in section 3.2.4 for each set of computational parameters in table 3.1, and for each of the first three Rossiter frequencies (for which we use equation (3.2)). We assume a tanh velocity profile with a linear spreading rate $d\delta_\omega/dx = 0.1$. Based on the discussion above and in section 3.2.3, it is clear that the true spreading rate is dependent on growth of the disturbances in the layer, which, in turn, is dependent on all of L/θ_0 , D/θ_0 , M , and Re_θ . However, we performed calculations using different values of the spreading rate, and found the amplitude variation to be relatively weak compared to the other factors.

3.4.3 Scattering

In order to assess the efficiency of the sound generation at the edge as a function of the Mach number, we use the simple model proposed by Tam & Block [1978], where the process is idealized as an oscillating compact mass source (monopole). We determine the strength Q of the monopole source by setting Q equal to the mass flow rate out of the cavity. Tam points out that “the unsteady mass addition and removal at the trailing edge of the cavity as the cause of the acoustic disturbance . . . essentially suggests a dipole source at the trailing edge,” since by this mechanism a compression wave outside the cavity (mass addition) would correspond to a rarefaction wave inside the cavity (mass removal). However, as Tam points out, experimental, and now computational, observations indicate that the pressure waves inside and outside the cavity are in fact in phase, which corresponds to a monopole source at the trailing edge. Thus, we model the acoustic source as a monopole at the trailing edge, whose strength is determined by the mass flow rate out of the cavity.

If density fluctuations are small, the mass flow rate per unit volume is given

by

$$Q = \frac{\dot{m}}{V} \approx \frac{\rho_\infty}{V} \int_0^L v(x, 0, t) dx, \quad (3.10)$$

where v is the vertical velocity, and V is the volume of the source, at this time unknown. Assuming the velocity perturbations are sinusoidal, with an exponentially growing envelope, the integral above will be dominated by the portion closest to the trailing edge, and thus scales as $\lambda|v(L)|$, where $|v(L)|$ denotes the amplitude of the velocity perturbation near the trailing edge, and λ is the wavelength of the instability wave. Expressing the wavelength as $\lambda = 2\pi c_p/\omega$, where c_p is the phase speed of the instability wave, the source strength scales as

$$\dot{Q} = i\omega Q \propto i\omega \frac{\rho_0}{V} \frac{c_p|v(L)|}{\omega} \propto \frac{\rho_0 c_p |v(L)|}{V}. \quad (3.11)$$

This expression may also be arrived at on dimensional grounds alone, if it is assumed that the monopole strength is proportional to the vertical velocity (or shear-layer displacement) at the trailing edge.

Density fluctuations then satisfy a Helmholtz equation [see, e.g., Crighton, 1975], and far from the source are given by

$$\frac{\rho}{\rho_\infty} \propto \frac{c_p|v(L)|}{a_\infty^2} \frac{e^{ikr}}{\sqrt{kr}}, \quad (3.12)$$

where r is the distance from the source, and $k = \omega/a_\infty$ is the wavenumber. Note that there are two asymptotic arguments leading to equation (3.12). The first is that the retarded time is negligible over the source region (compact source), and the second is that we are at large distance, on the scale of the wavelength, from the source. The second approximation is not valid at very low Mach numbers, where the cavity length is small compared to the wavelength of the acoustic waves. For the present range of M , the asymptotic properties of the Green's function for the Helmholtz equation (i.e., the zeroth order Hankel function of the first kind) can be used to show that there is negligible error in the second assumption.

At the cavity leading edge, $r = L$, we then have the following scaling law (assuming $c_p/U = \text{const}$, as in the Rossiter model):

$$\frac{|\rho(0)|}{\rho_\infty} \propto \frac{|v(L)|}{U} M^{3/2} St^{-1/2}, \quad (3.13)$$

where $|\rho(0)|$ denotes the magnitude of density fluctuations at the leading edge, $x = 0$.

3.4.4 Loop gain

We now have enough information to determine the scaling of the *loop gain* for the cavity: that is, the amplification of a disturbance as it is amplified by the

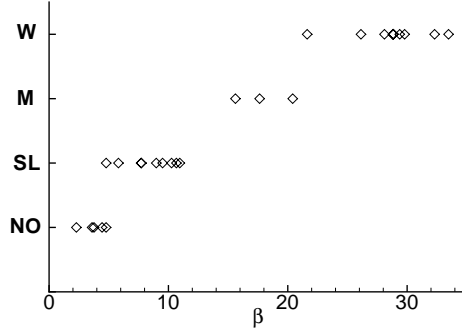


Figure 3.22: Correlation of loop gain β with mode of cavity oscillations. All runs from table 3.1 with $56 < Re_\theta < 70$ are shown. As in table 3.1, NO corresponds to no oscillations, SL denotes shear-layer mode, M denotes mixed mode, and W, wake mode.

shear layer and converted into a monopole acoustic source. (We do not include receptivity effects in this crude model.) Denoting the shear-layer amplification by $A(St, M, L/\theta_0, D/\theta_0)$, the loop gain scales as

$$\beta_n \propto A(St_n, M, L/\theta_0, D/\theta_0) M^{3/2} St_n^{-1/2} \quad (3.14)$$

where St_n denotes the Strouhal number of Rossiter mode n , given by Rossiter's formula (3.2). The total amplification is then $\beta = \max_n \beta_n$, and we take β as our criterion for predicting the onset of oscillations, and eventually wake mode. Note, however, that the dependence of Reynolds number is not included in (3.14), as our shear-layer calculations were inviscid. Variation with Reynolds number is considered separately below. Note also that this scaling law is not valid for small M , as the asymptotic approximation (3.12) no longer holds.

Figure 3.22 shows how β correlates with the mode of oscillation. Because Reynolds number effects are not included, we compare all runs in table 3.1 that fall in a limited Reynolds number range, $56 < Re_\theta < 70$. For each run, we compute the amplification β_n for the first three Rossiter modes ($n = 1, 2, 3$), and β for each run is then the maximum of the three. Figure 3.22 shows β vs. the observed mode of cavity oscillation, and we find that for this Reynolds number range, $\beta < 4.8$ corresponds to no oscillations, $4.8 < \beta < 15$ corresponds to shear-layer mode, $15 < \beta < 21$ for mixed mode, and $\beta > 21$ for pure wake mode.

3.4.5 Parametric dependence

We now discuss some results related to the specific parametric dependence of the transitions. In figure 3.23, we have plotted the total amplification from the shear layer alone (corresponding to A_n in equation (3.14)) for the first three Rossiter modes, as a function of L/θ_0 and D/θ_0 , at $M = 0.6$. Since, for fixed Mach number, the shear layer amplification is the predominant component of the loop gain β , the figure also indicates trends in β as the cavity length is varied. The

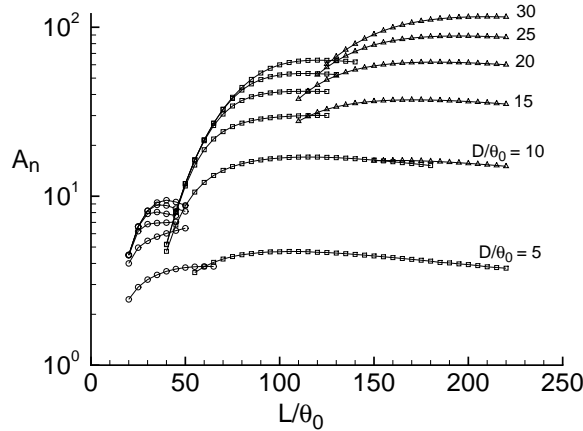


Figure 3.23: The shear-layer amplification, A_n , versus L/θ_0 for different D/θ_0 , with $M = 0.6$. The dominant mode is shown at each L/θ_0 , with $n = 1$ (\circ), $n = 2$ (\square), and $n = 3$ (Δ).

amplification shows strong dependence on D/θ_0 , especially for $D/\theta_0 < \sim 20$. This very well explains the trend seen (for low Mach number) by Sarohia [1975], who found the minimum cavity length for oscillations increased dramatically for small D/θ_0 . The plot also shows why the higher Rossiter modes tend to dominate for longer cavities, as has been observed in experiments.

It is interesting to note that the predictions show that multiple modes are likely to be present at roughly equal amplitudes for cavities of certain length, while, for other lengths, one mode is clearly dominant. For example, for $L/\theta_0 = 125$ and $D/\theta_0 = 30$, modes 2 and 3 should be of roughly equivalent strength (ignoring nonlinear interactions and frequency dependence of scattering/receptivity).

Figure 3.23 also shows similar effects for the transition to wake mode as a function of D/θ_0 , but given that the amplitude threshold is higher, wake mode should not occur in cavities with $D/\theta_0 < \sim 20$.

In figure 3.24 the total amplification in the shear layer for the first three Rossiter modes is plotted as a function of L/θ_0 and M , for $D/\theta_0 = 30$. The amplification rates are highest for the lowest Mach numbers, which is consistent with many previous analyses of the Kelvin-Helmholtz instability in compressible shear layers. This decreasing amplitude must be balanced by the increase in radiation efficiency at the edge as M is increased. As noted above, it is observed in experiments [Krishnamurty, 1956] that the minimum cavity length for the onset of fluctuations decreases with M . This is indeed what the model predicts, as evidenced by the good agreement with our data in figure 3.22.

We note that the computational data also shows a tendency for transition to wake mode with increasing Reynolds number. The R4 series of runs, for example, show a change from shear-layer to wake mode for $L/\theta_0 \approx 75$ as Re_θ varies from 40 to 80. The model of the transition process discussed above is based on an inviscid stability analysis, and is therefore unable to predict any Reynolds number

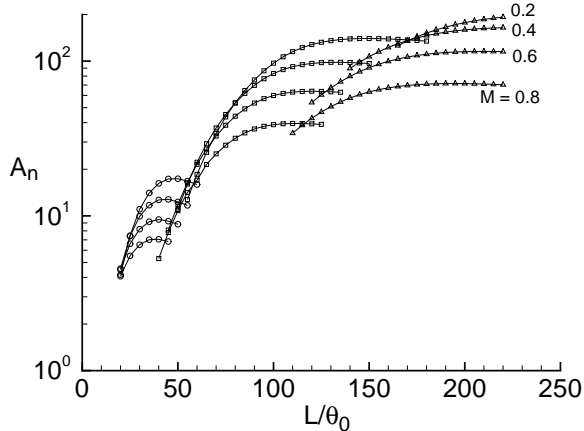


Figure 3.24: The shear-layer amplification, A_n , versus L/θ_0 for different M , with $D/\theta_0 = 30$. The dominant mode is shown at each L/θ_0 , with $n = 1$ (\circ), $n = 2$ (\square), and $n = 3$ (Δ).

effects. However, for the range of low Reynolds numbers, substantial reduction in the amplitude gain in the shear layer may be expected [e.g., Michalke, 1984], which is consistent with figure 3.14, and with the observed trend in transition to wake mode.

3.5 Concluding remarks

We have used numerical simulations to explore the operating regimes of the laminar flow past a two-dimensional rectangular cavity. For short cavities (relative to the upstream boundary-layer thickness), and for low Mach numbers and Reynolds numbers, the flow is steady. As these parameters are increased, the flow transitions into a shear-layer mode, where self-sustained oscillations occur. This is the regime usually observed in experiments, and the acoustic fields predicted by the simulation agree well with schlieren photographs from the experiments by Krishnamurty [1956]. The growth of disturbances in the shear layer is predicted well by a locally-parallel linear stability calculation, where the thickness of the shear layer is measured from the simulations.

For longer cavities, and larger Mach and Reynolds numbers, the flow transitions into a wake mode. Similar flow features have been observed in axisymmetric cavity experiments by Gharib & Roshko [1987], and in experiments in a pipe with closed side branches [Kriesels et al., 1995]. The frequency of oscillations in wake mode is independent of Mach number, indicating a purely hydrodynamic (non-acoustic) instability. In wake mode, a significant backflow is present inside the cavity, and we hypothesize that this backflow leads to an absolute instability, which may provide the feedback mechanism leading to wake mode. We have used a simple linear model to predict the scaling laws governing transition between the flow regimes,

and the model agrees well with data from our simulations.

To our knowledge, wake mode oscillations have not been observed in experiments in two-dimensional cavity geometries, for a similar range of L/D as we have investigated. (However, very recent three-dimensional PIV measurements in an $L/D = 5$ cavity show a time-averaged flow with a significant recirculating region, reaching about 15% of the freestream velocity [Krothapalli, 2001].) According to the criteria proposed in the previous section, transition to wake mode occurs when the amplitude of cavity oscillations increases beyond some threshold. Thus, any effect that decreases this amplitude should inhibit transition to wake mode. For instance, turbulent upstream boundary layers will likely inhibit transition to wake mode, since Krishnamurty [1956] observed that the acoustic radiation is less intense when the boundary layer is turbulent. Furthermore, three-dimensional effects may significantly change the character of the instabilities in the shear layer, making them less coherent, and ultimately inhibiting transition to wake mode. It appears that these three-dimensional effects do not affect the fundamental mechanisms underlying shear-layer mode, as our two-dimensional simulations in shear-layer mode agree well with experiments, but three-dimensional effects may reduce the overall amplitude of oscillations, which would inhibit transition to wake mode.

In the remainder of this thesis, we focus on the modeling and control of shear-layer mode, both because it is the regime usually observed in experiments, and because the underlying mechanisms are better understood, and lend themselves more readily to the modeling approaches we discuss in the following chapters.

Chapter 4

Model Reduction for Fluids

In this chapter, we discuss basic techniques for obtaining reduced-order models from simulations of fluid flows. First, we give an overview of the basic tools we use, Proper Orthogonal Decomposition and Galerkin projection. We briefly outline how these tools have been applied to incompressible flows in section 4.3. The main result of this chapter is the application to compressible flows in section 4.4.

4.1 Proper Orthogonal Decomposition

The central idea of the Proper Orthogonal Decomposition (POD) is, given a collection of data, elements of a vector space, to find a subspace of fixed dimension, which is “optimal,” in the sense that the error in the projection onto the subspace is minimized. Thus, the method is inherently data-based, and provides a way of distilling the information contained in large datasets, as are produced by simulations. The solution of the optimization problem is surprisingly simple—it reduces to a standard eigenvalue problem, and provides an orthonormal basis for the optimal subspace.

Here, we describe the decomposition in the context of an abstract Hilbert space. We use the abstract setting both for clarity, and more importantly, because in subsequent sections we will want to use different inner products, to obtain different notions of “optimality.”

The usual presentation of the method is in the stochastic setting (see Loève [1978, sec. 37.5]), where the “data” is regarded as a random variable. The presentation here treats the data as a finite ensemble, as it always is given in practice. This treatment removes many of the technical difficulties of the theory, since one need not worry about subtleties of infinite-dimensional operators, yet it retains all of the essential features relevant to model reduction.

4.1.1 The main theorem

First, we state the goal more precisely. Let H be a Hilbert space, with inner product $\langle \cdot, \cdot \rangle$. The goal is, given an ensemble of data $\{u^k \in H \mid k = 1, \dots, m\}$, find a subspace S of fixed dimension $n < m$, such that the error $E(\|u - Psu\|)$ is

minimized. Here, $\|\cdot\|$ is the induced norm on H , P_S is the orthogonal projection onto the subspace, and $E(\cdot)$ denotes an average over k . The data $\{u^k\}$ could be thought of as an ensemble of many different experiments, or as a time average, with u^k representing snapshots of a function $u(t)$ at different times $t = t_k$. We use the notation u to represent the entire ensemble $\{u^k\}$. The average $E(\cdot)$ may be a weighted average, and all we will assume is that it is linear, and thus may be interchanged with the inner product.

For our purposes, the space H will consist of functions on some spatial domain Ω in which a fluid evolves, e.g., $H = L^2(\Omega)$. These functions may be vector-valued, and in applications we will explicitly state which inner product we use.

Let $\{\varphi_j \in H \mid j = 1, \dots, n\}$ be an orthonormal basis for the subspace S . Then the orthogonal projection is given by

$$P_S u = \sum_{j=1}^n \langle u, \varphi_j \rangle \varphi_j \quad (4.1)$$

and it is simple to show that minimizing $E(\|u - P_S u\|)$ over S is equivalent to maximizing $E(\|P_S u\|)$, or maximizing $\sum_{j=1}^n E(|\langle u, \varphi_j \rangle|^2)$ over orthonormal functions φ_j . The desired φ_j are thus extremals of the functional

$$J[\varphi] = E(|\langle u, \varphi \rangle|^2) - \lambda(\|\varphi\|^2 - 1). \quad (4.2)$$

At this point, it is not obvious that the extremals of J will be orthogonal, but we will see shortly that they are.

Before finding extremals of (4.2), we introduce some notation. The space of all continuous linear complex-valued functionals on H is called the *dual space* of H , and is denoted H^* . For any vector $v \in H$, its *dual vector* $v^* \in H^*$ is given by $v^*(\cdot) = \langle \cdot, v \rangle$, a linear functional on H . Clearly, v^* depends on the inner product. For $v \in H$ and $\alpha \in H^*$, the *tensor product* $v \otimes \alpha : H \rightarrow H$ is the linear map given by $(v \otimes \alpha)\psi = v\alpha(\psi)$ for any $\psi \in H$. In particular, for $v, w \in H$, we have

$$(v \otimes w^*)\psi = vw^*(\psi) = v \langle \psi, w \rangle,$$

which of course depends on the inner product. (See Abraham et al. [1988] for the general theory of tensors on linear spaces.)

With this notation, we may rewrite the quantity $|\langle u, \varphi \rangle|^2$ as

$$|\langle u, \varphi \rangle|^2 = \langle u, \varphi \rangle \langle \varphi, u \rangle = \langle \langle \varphi, u \rangle u, \varphi \rangle = \langle (u \otimes u^*)\varphi, \varphi \rangle,$$

and so, introducing the linear operator $R : H \rightarrow H$ given by

$$R = E(u \otimes u^*), \quad (4.3)$$

we may rewrite (4.2) as

$$J[\varphi] = \langle R\varphi, \varphi \rangle - \lambda(\|\varphi\|^2 - 1). \quad (4.4)$$

It follows easily from the definition that R is self-adjoint (that is, $\langle R\varphi, \psi \rangle = \langle \varphi, R\psi \rangle$ for all $\varphi, \psi \in H$). Now, a necessary condition for φ to be an extremal of J is that the first variation vanish:

$$\frac{d}{d\delta} \bigg|_{\delta=0} J[\varphi + \delta\psi] = 0, \quad \text{for all } \psi \in H.$$

We have

$$\begin{aligned} \frac{d}{d\delta} \bigg|_{\delta=0} J[\varphi + \delta\psi] &= \frac{d}{d\delta} \left[\langle R(\varphi + \delta\psi), \varphi + \delta\psi \rangle - \lambda(\langle \varphi + \delta\psi, \varphi + \delta\psi \rangle - 1) \right] \bigg|_{\delta=0} \\ &= \langle R\psi, \varphi \rangle + \langle R\varphi, \psi \rangle - \lambda(\langle \psi, \varphi \rangle + \langle \varphi, \psi \rangle) \\ &= 2 \operatorname{Re} [\langle R\varphi - \lambda\varphi, \psi \rangle] \end{aligned}$$

where in the last equation we have used that R is self-adjoint. If φ is an extremal, this quantity must vanish for all variations ψ , and so we have

$$R\varphi = \lambda\varphi, \quad (4.5)$$

or φ must be an eigenfunction of R . Now, we see from (4.5) by taking an inner product with φ that

$$\lambda = E(|\langle u, \varphi \rangle|^2). \quad (4.6)$$

Thus, R is positive semi-definite ($\lambda \geq 0$), and the functions φ_j which maximize our original functional $\sum_{j=1}^n E(|\langle u, \varphi_j \rangle|^2)$ are the eigenfunctions corresponding to the largest n eigenvalues of R .

We now examine properties of the eigenvalues and eigenfunctions of R . It is obvious from the definition of R that its range is finite-dimensional (it is spanned by the $\{u^k\}$). Furthermore, R is bounded as long as the u^k are bounded, and hence R is compact (or completely continuous). For compact, self-adjoint operators, spectral theory guarantees at most a countable infinity of nonzero eigenvalues [Riesz & Sz.-Nagy, 1990], and since the range of R is finite-dimensional, the number of nonzero eigenvalues is actually finite. Furthermore, since R is self-adjoint, the eigenfunctions may be chosen to be orthonormal. We also mention that the solution to the optimization problem

$$\max \sum_{j=1}^n \langle R\varphi_j, \varphi_j \rangle \quad \text{for orthonormal } \varphi_j$$

may be obtained directly from functional analysis, without recourse to the variational argument given above [Riesz & Sz.-Nagy, 1990, sec. 93].

We summarize these results in the following theorem.

Theorem 4.1 (Proper Orthogonal Decomposition) *Given a linearly independent set $\{u^k \in H \mid k = 1, \dots, m\}$, the subspace S of dimension $n < m$ which minimizes $E(\|u - Psu\|)$ has an orthonormal basis $\{\varphi_j \in H \mid j = 1, \dots, n\}$ where*

φ_j are solutions of

$$R\varphi_j = \lambda_j \varphi_j, \quad (4.7)$$

where $R = E(u \otimes u^*)$ and $\lambda_1 \geq \lambda_2 \geq \dots \geq \lambda_n > 0$ are the largest n eigenvalues of R . The eigenfunctions φ_j are called POD modes.

We examine some properties of the POD in section 4.1.2, but first we illustrate with some examples.

Finite dimensions. Let $H = \mathbb{R}^p$, with the standard inner product $\langle \mathbf{x}, \mathbf{y} \rangle = x_i y_i$, where we use Einstein's convention of summing over repeated indices. Suppose the “data” is given as a collection of m linearly independent vectors $\{\mathbf{u}^k \in \mathbb{R}^p \mid k = 1, \dots, m\}$, and the average $E(\cdot)$ is just an arithmetic mean

$$E(f(\mathbf{u}^k)) = \frac{1}{m} \sum_{k=1}^m f(\mathbf{u}^k). \quad (4.8)$$

For $\mathbf{x}, \mathbf{y} \in \mathbb{R}^p$, we have $(\mathbf{x} \otimes \mathbf{y}^*)_{ij} = x_i y_j$, the usual dyadic product, so the operator $R : \mathbb{R}^p \rightarrow \mathbb{R}^p$ is the matrix given by

$$R_{ij} = E(\mathbf{u} \otimes \mathbf{u}^*)_{ij} = \frac{1}{m} \sum_{k=1}^m u_i^k u_j^k,$$

a $p \times p$ real symmetric matrix. Equation (4.7) is then a standard eigenvalue problem on \mathbb{R}^p .

Scalar-valued functions. Let $H = L^2[0, 1]$, the set of complex-valued square-integrable functions on the interval $[0, 1]$, with the inner product

$$\langle u, v \rangle = \int_0^1 \bar{v}(x) u(x) dx.$$

Then for $u, v, \varphi \in L^2[0, 1]$,

$$(u \otimes v^*)\varphi(x) = u(x) \langle \varphi, v \rangle = \int_0^1 u(x) \bar{v}(y) \varphi(y) dy,$$

so the eigenvalue problem (4.7) becomes

$$\int_0^1 E(u(x) \bar{u}(y)) \varphi(y) dy = \lambda \varphi(x),$$

a Fredholm integral equation, with kernel $K(x, y) = E(u(x) \bar{u}(y))$.

Vector-valued functions. Now let $H = C(\Omega, V)$, the space of continuous functions from some (spatial) domain $\Omega \subset \mathbb{R}^2$ to a vector space $V = \mathbb{C}^3$. Define an

inner product on H by

$$\langle \mathbf{u}, \mathbf{v} \rangle = \int_{\Omega} \bar{\mathbf{v}}^T(\mathbf{x}) A \mathbf{u}(\mathbf{x}) d\mathbf{x},$$

where $A \in \mathbb{C}^{3 \times 3}$ is a positive-definite Hermitian matrix. Then

$$(\mathbf{u} \otimes \mathbf{v}^*) \varphi(\mathbf{x}) = \mathbf{u}(\mathbf{x}) \langle \varphi, \mathbf{v} \rangle = \int_{\Omega} \mathbf{u}(\mathbf{x}) \bar{\mathbf{v}}^T(\mathbf{y}) A \varphi(\mathbf{y}) d\mathbf{y}$$

so the eigenvalue problem (4.7) becomes

$$\int_{\Omega} E(\mathbf{u}(\mathbf{x}) \bar{\mathbf{u}}^T(\mathbf{y})) A \varphi(\mathbf{y}) d\mathbf{y} = \lambda \varphi(\mathbf{x}). \quad (4.9)$$

4.1.2 Properties of the POD

In this section we discuss several important properties of the POD.

Energy captured

There is a physical significance to the value of the eigenvalue λ_k in (4.7): λ_k represents the average “energy” captured by POD mode φ_k , where the energy is in the sense of the induced norm on H . Letting $P_{\varphi}u = \langle u, \varphi \rangle \varphi$ denote the orthogonal projection of u onto the (normalized) function φ , the average energy captured by φ is given by

$$\begin{aligned} E(\|P_{\varphi}u\|^2) &= E(\langle P_{\varphi}u, P_{\varphi}u \rangle) = E(\langle \langle u, \varphi \rangle \varphi, \langle u, \varphi \rangle \varphi \rangle) \\ &= E(\langle u, \varphi \rangle \langle \varphi, u \rangle) \langle \varphi, \varphi \rangle \\ &= E(|\langle u, \varphi \rangle|^2), \end{aligned}$$

since $\|\varphi\| = 1$. Thus, by (4.6), λ_k is the average energy captured by mode φ_k .

Span of the snapshots

We mentioned in the previous section that the range of $R = E(u \otimes u^*)$ is contained within the span of the ensemble $\{u^k\}$. This follows directly from the definition of R , using the property of the average that $E(f(u))$ is a linear combination of $f(u^k)$. Note that in the stochastic setting which is often used for discussing the POD, the ensemble of u is infinite, and more work is needed to show this [Holmes et al., 1996]. Note also that the range is not necessarily *equal* to the span of the u^k , as this depends on the average (for instance, $E(\cdot)$ could be a weighted average, giving zero weight to certain elements).

An important implication of this result is that the POD modes (clearly in the range of R) may be written as linear combinations of the “snapshots” u^k . That is,

for any POD mode φ , we may write

$$\varphi = \sum_{k=1}^m c_k u^k \quad (4.10)$$

for some scalar coefficients c_k .

Inherited properties

A consequence of the preceding property is that, if every snapshot u^k satisfies a given linear constraint, say $L(u^k) = 0$ for all k , where $L : H \rightarrow \mathbb{R}$ is linear, then the POD modes will each satisfy that constraint as well. For any POD mode φ , by (4.10) we have

$$L(\varphi) = L\left(\sum_{k=1}^m c_k u^k\right) = \sum_{k=1}^m c_k L(u^k) = 0.$$

Examples of constraints which frequently arise are the divergence-free condition for velocity in incompressible flow ($\operatorname{div} u^k = 0$) and linear homogeneous boundary conditions (e.g., the no slip condition $u^k(\text{wall}) = 0$).

Symmetry

In the presence of translational symmetry (i.e., if the data is homogeneous in a spatial dimension), it can be shown that the POD modes reduce to Fourier modes in the directions of the symmetry [Sirovich, 1987]. Symmetries do not arise in the flows we discuss here, so we do not dwell on this point, but we mention that traveling POD modes can provide more accurate results (for a fixed number of modes) than the standard POD. However, if reduced-order models are to be obtained via Galerkin projection (see section 4.2), then one needs a *reconstruction equation* to determine the position of the traveling wave, and to close the resulting system of ODEs, as discussed in Rowley & Marsden [2000].

4.1.3 Computation: method of snapshots

The method of snapshots provides an alternate way of computing the POD modes, and is often more efficient than the *direct method*, where one directly solves the eigenvalue problem (4.7).

Let the average $E(\cdot)$ be defined as a weighted average over the snapshots u^k :

$$E(f(u)) = \sum_k \alpha_k f(u^k),$$

where the weights $\alpha_j > 0$ satisfy $\sum_j \alpha_j = 1$. (In this section, all sums are from $1, \dots, m$.) Typically, $\alpha_j = 1/m$, for equal weighting.

From the previous section, any eigenfunction φ may be written as a linear combination of snapshots

$$\varphi = \sum_k c_k u^k \quad (4.11)$$

for some coefficients $c_k \in \mathbb{C}$. The eigenvalue problem $R\varphi = \lambda\varphi$ then becomes

$$\begin{aligned} E(u \otimes u^*) \sum_k c_k u^k &= \lambda \sum_k c_k u^k \\ \sum_j \sum_k \alpha_j (u^j \otimes (u^j)^*) c_k u^k &= \sum_k \lambda c_k u^k \\ \sum_k \left(\sum_j \alpha_k \langle u^j, u^k \rangle c_j \right) u^k &= \sum_k \lambda c_k u^k. \end{aligned}$$

It suffices to solve

$$\sum_j \alpha_k \langle u^j, u^k \rangle c_j = \lambda c_k, \quad k = 1, \dots, m \quad (4.12)$$

which is just the standard m -dimensional eigenvalue problem

$$Uc = \lambda c, \quad (4.13)$$

where $c = (c_1, \dots, c_m)$ and U is an $m \times m$ matrix with $U_{ij} = \alpha_i \langle u^j, u^i \rangle$. Note that U is self-adjoint under the inner product $\langle a, b \rangle_\alpha = \sum_j a_j b_j^*/\alpha_j$, so the eigenfunctions c are orthogonal under the same inner product.

To summarize, the direct solution of (4.7) involves solving an eigenvalue problem on the space H , which may be infinite-dimensional. For instance, if the snapshots $u^k \in H$ are data from a finite-difference simulation, the dimension of H will be the number of gridpoints in the simulation, typically large. By contrast, the method of snapshots involves solving an m -dimensional eigenvalue problem (4.13), where m is the number of snapshots in the ensemble. The method of snapshots is thus more efficient whenever the number of snapshots is smaller than the number of gridpoints.

4.1.4 Affine subspaces

The POD described in section 4.1 determines a *linear* subspace S which optimally spans an ensemble of data. Often, it makes more sense to project the data onto an *affine* subspace. Given an element $b \in H$ and a linear subspace S , the affine space S_b is given by

$$S_b = \{b + v \mid v \in S\}. \quad (4.14)$$

The POD procedure extends easily to affine spaces, and amounts to subtracting the element b from the ensemble before performing the POD.

Given an ensemble of data $\{u^k \in H\}$, and an element $b \in H$, we form the new ensemble $\{v^k\}$ where $v^k = u^k - b$. The standard POD then provides a linear subspace S which optimally spans the ensemble $\{v^k\}$. If $\{\varphi_j \mid j = 1, \dots, n\}$ is the orthonormal basis for S , the projection onto S is, as before,

$$P_S v = \sum_{j=1}^n \langle v, \varphi_j \rangle \varphi_j,$$

and the projection onto S_b is then

$$P_{S_b} u = b + \sum_{j=1}^n \langle u - b, \varphi_j \rangle \varphi_j.$$

Note that the element $b \in H$ must be fixed before finding the POD modes φ_j . Typically we will choose b to be the mean of the ensemble, so $b = E(u)$, but other choices are possible.

4.2 Galerkin projection

Consider a dynamical system which evolves in a Hilbert space H . In particular, for $u(t) \in H$, $u(t)$ satisfies

$$\dot{u} = X(u), \quad (4.15)$$

where X is a vector field on H . For instance, for a partial differential equation (PDE) governing a variable $u(x, t)$, defined on some spatial domain $x \in \Omega$, H will be a space of functions defined on Ω , and X will be a spatial differential operator. Given a finite-dimensional subspace S of H , we wish to determine a dynamical system which evolves on S and approximates (4.15) in some sense. This dynamical system will be denoted

$$\dot{r} = X_S(r), \quad (4.16)$$

where $r(t) \in S$ and X_S is a vector field on S . Galerkin projection specifies this vector field by

$$X_S(r) = \mathbb{P}X(r), \quad (4.17)$$

where $\mathbb{P} : H \rightarrow S$ is the orthogonal projection map. The projection theorem states that this approximation is optimal, in the sense that it minimizes the error $\|X_S(r) - X(r)\|$, where $\|\cdot\|$ is the induced norm on H [Luenberger, 1997].

Galerkin projection is a special case of *weighted residual methods* [Fletcher, 1991], which specify the vector field X_S by requiring

$$\langle X_S(r) - X(r), w_k \rangle = 0, \quad k = 1, \dots, n, \quad (4.18)$$

for some specified weight functions $w_k \in H$, where $n = \dim S$. This is a linear system of n linear equations which determine the n -dimensional vector $X_S(r)$. In the Galerkin method, the weight functions w_k are chosen to be basis functions for the subspace S , and so the residual $X_S(r) - X(r)$ is orthogonal to S , which is equivalent to (4.17).

To apply this method to computations, we need to write (4.16) in coordinates. Let $\{\varphi_k \in H \mid k = 1, \dots, n\}$ be a basis for a subspace S . (For instance, such a basis may be obtained from POD on a set of data, as described in the preceding section.) Writing $r(t)$ in coordinates $a_k(t)$ with respect to this basis, we have

$$r(t) = \sum_{k=1}^n a_k(t) \varphi_k, \quad (4.19)$$

and using (4.18) with $w_k = \varphi_k$, (4.16) becomes

$$\sum_{j=1}^n \dot{a}_j(t) \langle \varphi_j, \varphi_k \rangle = \langle X(r(t)), \varphi_k \rangle, \quad k = 1, \dots, n. \quad (4.20)$$

This defines a linear system of ODEs for the evolution of $a_j(t)$. If the basis functions are orthonormal, then (4.20) further simplifies to

$$\dot{a}_k(t) = \langle X(r(t)), \varphi_k \rangle, \quad k = 1, \dots, n. \quad (4.21)$$

This is why an orthonormal basis is especially desirable, because we avoid inverting an $n \times n$ matrix to solve for \dot{a} .

The Galerkin procedure also extends easily to affine spaces, mentioned in section 4.1.4. Given the linear subspace S as above, and an element $b \in H$, we wish to project the dynamics onto the affine space $S_b = \{b + v \mid v \in S\}$. In this case, the expansion (4.19) takes the form

$$r(t) = b + \sum_{k=1}^n a_k(t) \varphi_k, \quad (4.22)$$

where $r(t) \in S_b$, and the projected equations are the same as above, (4.20) or (4.21), the only difference being the new expression (4.22) for $r(t)$.

4.2.1 Example: Quadratic equations

For many types of equations, the ODEs given by (4.21) may be determined analytically, in terms of the coordinates a_k . This is particularly useful computationally, as the inner product in (4.21) does not need to be computed at every timestep. We illustrate this with a quadratic PDE described by $\dot{u} = X(u)$, with

$$X(u) = L(u) + Q(u, u),$$

where $L : H \rightarrow H$ is a linear operator, and $Q : H \times H \rightarrow H$ is a bilinear operator (linear in each argument). We project the dynamics onto the affine space S_b , expanding $r(t) \in S_b$ as in (4.22). The projected ODEs (4.21) become

$$\begin{aligned}\dot{a}_k(t) &= \langle L(r) + Q(r, r), \varphi_k \rangle \\ &= \left\langle L\left(b + \sum_i a_i(t) \varphi_i\right) + Q\left(b + \sum_i a_i(t) \varphi_i, b + \sum_j a_j(t) \varphi_j\right), \varphi_k \right\rangle \\ &= b_k + \sum_i L_k^i a_i(t) + \sum_{i,j} Q_k^{ij} a_i(t) a_j(t),\end{aligned}$$

where the quantities

$$\begin{aligned}b_k &= \langle L(b) + Q(b, b), \varphi_k \rangle \\ L_k^i &= \langle L(\varphi_i) + Q(b, \varphi_i) + Q(\varphi_i, b), \varphi_k \rangle \\ Q_k^{ij} &= \langle Q(\varphi_i, \varphi_j), \varphi_k \rangle\end{aligned}$$

are constants (independent of t) which may be determined before integrating the ODEs.

A similar simplification is, of course, possible for cubic and higher-order polynomial nonlinearities, but for higher powers, the number of coefficients becomes unwieldy for even moderate dimensions n , so we restrict ourselves to quadratic governing equations.

4.3 Incompressible fluids

The applications in this thesis concern compressible flows, but we outline the well-established methods for applying POD/Galerkin to incompressible flows, and highlight the differences for compressible flows in the next section.

The definition of incompressibility is that the velocity $\mathbf{u} = (u, v, w)$ is divergence free, $\operatorname{div} \mathbf{u} = 0$. The motion of the fluid satisfies the Navier-Stokes equations [Batchelor, 1967], written in Cartesian coordinates as

$$\frac{D\mathbf{u}}{Dt} = -\nabla p + \nu \nabla^2 \mathbf{u}, \quad (4.23)$$

where ν is the viscosity, p is the pressure, and $D/Dt = \partial/\partial t + \mathbf{u} \cdot \nabla$ is the material derivative. Velocities have been normalized by some velocity scale U , lengths by a length scale L , time by U/L , pressure by ρU^2 where ρ is the density, and viscosity by $\rho U L$ (thus, ν is the reciprocal of the Reynolds number). These equations may be written as

$$\dot{\mathbf{u}} = N(\mathbf{u}) - \nabla p \quad (4.24)$$

where $N(\mathbf{u}) = -(\mathbf{u} \cdot \nabla) \mathbf{u} + \nu \nabla^2 \mathbf{u}$.

For incompressible flows, we write the velocity \mathbf{u} as an expansion in POD modes $\varphi(\mathbf{x})$, defined on a spatial domain Ω in which the fluid evolves:

$$\mathbf{u}(\mathbf{x}, t) = \sum_{j=1}^n a_j(t) \varphi_j(\mathbf{x}). \quad (4.25)$$

Our Hilbert space H is just the space of smooth (C^∞) vector-valued functions on Ω , with the standard inner product

$$\langle \mathbf{u}, \mathbf{v} \rangle = \int_{\Omega} \mathbf{u}(\mathbf{x}) \cdot \mathbf{v}(\mathbf{x}) dV. \quad (4.26)$$

(Additionally, we restrict the space H to contain only functions with finite norm.)

Inserting the expansion (4.25) into the Navier-Stokes equations (4.24), and taking an inner product with φ_k gives

$$\dot{a}_k = \langle N(\mathbf{u}), \varphi_k \rangle - \langle \nabla p, \varphi_k \rangle. \quad (4.27)$$

The pressure term on the right-hand side is easily rewritten

$$\langle \nabla p, \varphi_k \rangle = \int_{\Omega} \varphi_k \cdot \nabla p dV = \int_{\Omega} \operatorname{div}(p \varphi_k) dV = \int_{\partial\Omega} p \varphi_k \cdot \mathbf{n} dS$$

where in the second equality we have used that $\operatorname{div} \varphi_k = 0$. Thus, this term depends only on the pressure on the boundary $\partial\Omega$. Furthermore, if velocity is zero along the boundary (for instance, at a wall, or in the farfield of an open flow), then $\varphi_k = 0$ on $\partial\Omega$, and the pressure term vanishes altogether. If the boundary is not a wall, but rather an “artificial” boundary we impose (i.e., we consider only a limited portion of the whole flow), then the pressure term represents the influence of the rest of the flow on the domain we are considering, and must be specified as a boundary condition.

The technique for incompressible flows is well known. Many enhancements to the basic theory exist (see Holmes et al. [1996] for a thorough discussion), but the essential elements are the same as given here. The main feature that is normally included, but is not mentioned above, is that the velocity is usually decomposed into mean and fluctuating components ($\mathbf{u} = \bar{\mathbf{u}} + \mathbf{u}'$), where the mean $\bar{\mathbf{u}}$ is slowly varying in time. The mean may then be described in terms of the fluctuations \mathbf{u}' , which give rise to Reynolds stresses, as discussed in Aubry et al. [1988]. This is an important distinction, and gives rise to cubic equations, while the equations (4.27) are only quadratic. Another enhancement to the basic theory is the modeling of the energy transfer to the higher modes. In this thesis, we take the mean flow to be constant in time, without attempting to model the Reynolds stress contributions, and we neglect the energy transfer to the higher modes. These extensions could presumably be added to the compressible theory as well.

4.4 Compressible fluids

One of the main contributions of this thesis is a method for applying the above techniques to compressible flows. The distinction is a fundamental one. On a superficial level, the constraint $\operatorname{div} \mathbf{u} = 0$ no longer holds. On a more fundamental level, in a compressible flow, the thermodynamic variables are *dyamically* important, and must be included in the actual dynamics, not merely as a constraint. For incompressible flows, as discussed above, the pressure drops out completely, or appears only as an imposed boundary condition, and the only dynamical variable is the velocity. For compressible flows, this is not the case, and evolution equations must be given for one or more thermodynamic variables (e.g., ρ , p , entropy s , enthalpy h), as well as the velocity. This introduces further questions of whether to treat these variables completely separately from the velocity, or together as a single vector-valued “configuration” variable (e.g., $\mathbf{q}(x) = (\rho, u, v, p)(x)$).

We consider both alternatives, first discussing a *scalar-valued* method, where we compute separate POD modes for each flow variable, and next discussing a *vector-valued* method, where we write all the flow variables together as a single vector, and compute one set of vector-valued POD modes. To do this, we first need to define an appropriate inner product on our configuration space—the standard inner product may not be a sensible choice. For instance, if we use as flow variables $\mathbf{q} = (\rho, u, v, p)$, defined on the fluid domain Ω , the standard inner product is

$$\langle \mathbf{q}_1, \mathbf{q}_2 \rangle = \int_{\Omega} (\rho_1 \rho_2 + u_1 u_2 + v_1 v_2 + p_1 p_2) dV, \quad (4.28)$$

which does not make dimensional sense, since one cannot add a velocity and a pressure. We introduce an inner product suitable for compressible flows in section 4.4.3.

4.4.1 Governing equations

The compressible Navier Stokes equations, written in Cartesian tensor notation, are given by

$$\begin{aligned} \frac{D\rho}{Dt} + \rho \operatorname{div} \mathbf{u} &= 0 \\ \rho \frac{Du_i}{Dt} &= -\frac{\partial p}{\partial x_i} + \frac{\partial}{\partial x_j} 2\mu \left(S_{ij} - \frac{1}{3} \delta_{ij} \operatorname{div} \mathbf{u} \right) \\ T \frac{Ds}{Dt} &= \Phi + \frac{1}{\rho} \frac{\partial}{\partial x_i} \left(k \frac{\partial T}{\partial x_i} \right) \end{aligned}$$

(see Batchelor [1967]), where

$$S_{ij} = \frac{1}{2} \left(\frac{\partial u_i}{\partial x_j} + \frac{\partial u_j}{\partial x_i} \right)$$

is the rate-of-strain tensor (the symmetric part of the velocity gradient), and

$$\Phi = \frac{2\mu}{\rho} \left(S_{ij} S_{ij} - \frac{1}{3} (\operatorname{div} \mathbf{u})^2 \right)$$

is the rate of dissipation of mechanical energy. Here, s is the entropy, T is the temperature, and k the thermal conductivity of the fluid.

These equations are significantly more complicated than the incompressible equations, so we make some approximations to obtain a simpler set of equations which we may use for Galerkin projection. For the cavity, we consider cold flow ($T_{\text{wall}} = T_{\infty}$) and note that if the Mach number is not too high, density gradients will remain small and will be dominated by pressure changes. This is consistent with the neglect of the viscous dissipation Φ and heat conduction in the energy equation, and thus we treat the flow as *isentropic*. However, we retain the viscous diffusion in the momentum equation, but in this term we assume dynamic and kinematic viscosities are constant, again under the approximation that temperature gradients are small. Under these assumptions, the equations of motion become

$$\begin{aligned} \frac{D\rho}{Dt} + \rho \operatorname{div} \mathbf{u} &= 0 \\ \frac{D\mathbf{u}}{Dt} + \frac{1}{\rho} \nabla p &= \nu \nabla^2 \mathbf{u} \\ ds &= 0, \end{aligned} \tag{4.29}$$

where $\nu = \mu/\bar{\rho}$ is a constant. We still have more variables than equations, so to close the system we require an equation of state. With an equation of state, we may write the equations in terms of a single thermodynamic variable, since the entropy is constant. Any thermodynamic variable (independent of entropy) will suffice, but the enthalpy h is particularly convenient, as we shall see shortly.

Using the ideal gas relation $p = \rho RT$, we obtain the relation

$$a^2 = \frac{\gamma p}{\rho} = (\gamma - 1)h, \tag{4.30}$$

where a is the local sound speed. Using the Gibbs equation

$$dh = Tds + \frac{1}{\rho} dp \tag{4.31}$$

with $ds = 0$, the equations (4.29) are easily written in terms of h alone:

$$\begin{aligned} \frac{Dh}{Dt} + (\gamma - 1)h \operatorname{div} \mathbf{u} &= 0 \\ \frac{D\mathbf{u}}{Dt} + \nabla h &= \nu \nabla^2 \mathbf{u}. \end{aligned} \tag{4.32}$$

This procedure will work for any thermodynamic variable, but the enthalpy is particularly convenient, because the equations (4.32) are *quadratic*. If we used the

density, for instance, the momentum equation would become

$$\frac{D\mathbf{u}}{Dt} + \rho^{\gamma-2} \nabla \rho = \nu \nabla^2 \mathbf{u}.$$

For air, $\gamma = 1.4$, so the exponent $\gamma - 2$ in the above equation is fractional, which would cause difficulty when we perform Galerkin projections, described in section 4.2.

Another choice of thermodynamic variable which yields quadratic equations is the local sound speed a . Using (4.30), the equations (4.32) become

$$\begin{aligned} \frac{Da}{Dt} + \frac{\gamma-1}{2} a \operatorname{div} \mathbf{u} &= 0 \\ \frac{D\mathbf{u}}{Dt} + \frac{2}{\gamma-1} a \nabla a &= \nu \nabla^2 \mathbf{u}. \end{aligned} \quad (4.33)$$

The equations (4.32) and (4.33) are equivalent, and we refer to them (in either form) as the *isentropic Navier-Stokes equations*. We use the enthalpy form (4.32) with the scalar-valued method discussed in the next section, and the equations in terms of sound speed (4.33) with the vector-valued method discussed in section 4.4.4.

4.4.2 Scalar-valued POD modes

In this method, we consider each flow variable separately, and expand each flow variable in its own set of POD modes:

$$\begin{aligned} u(x, y, t) &= \bar{u}(x, y) + \sum_{j=1}^n u_j(t) \tilde{u}^j(x, y) \\ v(x, y, t) &= \bar{v}(x, y) + \sum_{j=1}^n v_j(t) \tilde{v}^j(x, y) \\ h(x, y, t) &= \bar{h}(x, y) + \sum_{j=1}^n h_j(t) \tilde{h}^j(x, y), \end{aligned} \quad (4.34)$$

where, e.g., $\tilde{u}^j(x, y)$ are the POD modes, $u_j(t)$ are the time coefficients, and $\bar{u}(x, y)$ is fixed, usually taken to be the mean of the snapshots used for the POD. The inner product we use here is just the standard inner product on real-valued functions:

$$\langle f, g \rangle = \int_{\Omega} f(x, y) g(x, y) dV$$

where $\Omega \subset \mathbb{R}^2$ is the region in which the fluid evolves.

Next, we write the isentropic Navier-Stokes equations (4.32) in nondimensional

form, as

$$\begin{aligned} u_t + uu_x + vu_y + h_x &= \frac{1}{\text{Re}_L} (u_{xx} + u_{yy}) \\ v_t + uv_x + vv_y + h_y &= \frac{1}{\text{Re}_L} (v_{xx} + v_{yy}) \\ h_t + uh_x + vh_y + (\gamma - 1)h(u_x + v_y) &= 0, \end{aligned} \quad (4.35)$$

where $\text{Re}_L = UL/\nu$. Here, velocities have been normalized by the freestream velocity U , h has been nondimensionalized by U^2 , x and y by a length L , and time by L/U . Inserting the expansions (4.34) into these equations, and taking inner products with the POD modes gives the system of ODEs

$$\begin{aligned} \dot{u}_k &= b_k^u + \sum_{i=1}^n (c_{ik}^u u_i + d_{ik}^u v_i + e_{ik}^u h_i) + \sum_{i,j=1}^n (p_{ijk}^u u_i u_j + q_{ijk}^u v_i u_j) \\ \dot{v}_k &= b_k^v + \sum_{i=1}^n (c_{ik}^v u_i + d_{ik}^v v_i + e_{ik}^v h_i) + \sum_{i,j=1}^n (p_{ijk}^v u_i v_j + q_{ijk}^v v_i v_j) \\ \dot{h}_k &= b_k^h + \sum_{i=1}^n (c_{ik}^h u_i + d_{ik}^h v_i + e_{ik}^h h_i) + \sum_{i,j=1}^n (p_{ijk}^h u_i h_j + q_{ijk}^h v_i h_j), \end{aligned} \quad (4.36)$$

where the coefficients are given by

$$\begin{aligned} b_k^u &= - \left\langle \bar{u} \bar{u}_x + \bar{v} \bar{u}_y + \bar{h}_x - (\bar{u}_{xx} + \bar{u}_{yy})/\text{Re}_L, \tilde{u}^k \right\rangle \\ b_k^v &= - \left\langle \bar{u} \bar{v}_x + \bar{v} \bar{v}_y + \bar{h}_y - (\bar{v}_{xx} + \bar{v}_{yy})/\text{Re}_L, \tilde{v}^k \right\rangle \\ b_k^h &= - \left\langle \bar{u} \bar{h}_x + \bar{v} \bar{h}_y + (\gamma - 1) \bar{h} (\bar{u}_x + \bar{v}_y), \tilde{h}^k \right\rangle \end{aligned}$$

$$\begin{aligned} c_{ik}^u &= - \left\langle \bar{u} \tilde{u}_x^i + \bar{v} \tilde{u}_y^i + \tilde{u}^i \bar{u}_x - (\tilde{u}_{xx}^i + \tilde{u}_{yy}^i)/\text{Re}_L, \tilde{u}^k \right\rangle \\ c_{ik}^v &= - \left\langle \tilde{u}^i \bar{v}_x, \tilde{v}^k \right\rangle \\ c_{ik}^h &= - \left\langle \tilde{u}^i \bar{h}_x + (\gamma - 1) \bar{h} \tilde{u}_x^i, \tilde{h}^k \right\rangle \end{aligned}$$

$$\begin{aligned} d_{ik}^u &= - \left\langle \tilde{v}^i \bar{u}_y, \tilde{u}^k \right\rangle \\ d_{ik}^v &= - \left\langle \bar{u} \tilde{v}_x^i + \bar{v} \tilde{v}_y^i + \tilde{v}^i \bar{v}_y - (\tilde{v}_{xx}^i + \tilde{v}_{yy}^i)/\text{Re}_L, \tilde{v}^k \right\rangle \\ d_{ik}^h &= - \left\langle \tilde{v}^i \bar{h}_y + (\gamma - 1) \bar{h} \tilde{v}_y^i, \tilde{h}^k \right\rangle \end{aligned}$$

$$\begin{aligned}
e_{ik}^u &= - \left\langle \tilde{h}_x^i, \tilde{u}^k \right\rangle \\
e_{ik}^v &= - \left\langle \tilde{h}_y^i, \tilde{v}^k \right\rangle \\
e_{ik}^h &= - \left\langle \bar{u} \tilde{h}_x^i + \bar{v} \tilde{h}_y^i + (\gamma - 1) \tilde{h}^i (\bar{u}_x + \bar{v}_y), \tilde{h}^k \right\rangle \\
p_{ijk}^u &= \left\langle \tilde{u}^i \tilde{u}_x^j, \tilde{u}^k \right\rangle & q_{ijk}^u &= \left\langle \tilde{v}^i \tilde{u}_y^j, \tilde{u}^k \right\rangle \\
p_{ijk}^v &= \left\langle \tilde{u}^i \tilde{v}_x^j, \tilde{v}^k \right\rangle & q_{ijk}^v &= \left\langle \tilde{v}^i \tilde{v}_y^j, \tilde{v}^k \right\rangle \\
p_{ijk}^h &= \left\langle \tilde{u}^i \tilde{h}_x^j + (\gamma - 1) \tilde{h}^j \tilde{u}_x^i, \tilde{h}^k \right\rangle & q_{ijk}^h &= \left\langle \tilde{v}^i \tilde{h}_y^j + (\gamma - 1) \tilde{h}^j \tilde{v}_y^i, \tilde{h}^k \right\rangle.
\end{aligned}$$

The equations (4.36) represent a reduced-order model of the isentropic Navier-Stokes equations. The original system (4.32), consisting of three coupled PDEs, has been reduced to a system of $3n$ coupled, quadratic ODEs, where n is the number of POD modes used for each variable. For many situations, the number of modes n required to capture a large fraction of the energy is small (say < 20), so these equations represent a significant reduction in order, since the typical number of gridpoints used in a simulation is $O(10^6)$. We apply these equations to the flow over a rectangular cavity in chapter 5.

Note that we could leave Re_L as a parameter in the equations (4.36), but in this thesis we do not study the bifurcation behavior of the equations for scalar-valued POD modes. We do include the effect of parameters for the equations for vector-valued modes, however, discussed in section 4.4.4.

4.4.3 Inner products for compressible flow

In order to obtain vector-valued POD modes, and perform Galerkin projections as in the previous section, we must first define an inner product. Here we introduce a family of inner products useful for compressible flow problems. As mentioned earlier, the usual inner product (e.g., (4.28)) may not make dimensional sense when both thermodynamic and kinematic variables are included. Of course, one could simply nondimensionalize the variables, but then the sense in which projections are “optimal” is rather arbitrary, and depends on the nondimensionalization (essentially the choice of “coordinates”), not on any physical grounds. We seek an inner product which makes intuitive sense, in that the “energy” defined by the induced norm is a meaningful physical quantity.

It is natural for the induced norm to be related to the *total energy* of a system. For instance, for a mechanical system this might be the kinetic energy—indeed, for incompressible flows, the norm induced by the standard inner product is the kinetic energy. For compressible flows, both thermodynamic and kinematic variables contribute to the total energy. For instance, the stagnation (or total) enthalpy of the

flow is given by

$$h_0 = h + \frac{1}{2}(u^2 + v^2),$$

where h is the static enthalpy. Analogously, the stagnation energy is $e = E + \frac{1}{2}(u^2 + v^2)$, where $E = h/\gamma$ is the internal energy per unit mass. Motivated by these physical quantities based on energy, we look for inner products which have induced norms of the form

$$\frac{1}{2}\|\mathbf{q}\|_\alpha^2 = \int_{\Omega} \left(\alpha h + \frac{1}{2}(u^2 + v^2) \right) dV, \quad (4.37)$$

where \mathbf{q} is the vector of flow variables, and $\alpha > 0$ is a constant. Note that the right-hand side of (4.37) is not quadratic, because h appears linearly, but this is easily remedied by transforming to the flow variables $\mathbf{q} = (u, v, a)$, since $a^2 = (\gamma - 1)h$, by (4.30). Thus, we define a family of inner products

$$\langle \mathbf{q}_1, \mathbf{q}_2 \rangle_\alpha = \int_{\Omega} \left(u_1 u_2 + v_1 v_2 + \frac{2\alpha}{\gamma - 1} a_1 a_2 \right) dV, \quad (4.38)$$

which has induced norm given by (4.37).

Obviously, choosing $\alpha = 1$ corresponds to using the integral of the stagnation enthalpy as the norm, and this is the choice we take for the results presented in this thesis. Taking $\alpha = 1/\gamma$ corresponds to using the stagnation energy as the norm. However, note that neither the integral of the stagnation enthalpy or the stagnation energy is actually a conserved quantity. The conserved quantity is the *total energy*, given by

$$\int_{\Omega} \left(\rho E + \frac{1}{2}\rho(u^2 + v^2) \right) dV. \quad (4.39)$$

(Of course, this is only conserved if there is no energy flux through the boundary of Ω , as when the velocity goes to zero on $\partial\Omega$.) It is not obvious how to define an inner product which has (4.39) as the induced norm, though this would perhaps be the most natural, from an energy point of view. However, we note that for $\alpha = 1/(\gamma - 1)$, the induced norm actually is a conserved quantity, for inviscid, isentropic flows.

With $\alpha = 1/(\gamma - 1)$, the integrand of (4.37) becomes

$$C = \frac{1}{\gamma - 1}h + \frac{1}{2}\mathbf{u} \cdot \mathbf{u},$$

where $\mathbf{u} = (u, v)$. Thus, assuming *isentropic* flow (equations (4.32) with $\nu = 0$),

we have

$$\begin{aligned}\frac{DC}{Dt} &= \frac{1}{\gamma-1} \frac{Dh}{Dt} + \mathbf{u} \cdot \frac{D\mathbf{u}}{Dt} \\ &= -h \operatorname{div} \mathbf{u} - \mathbf{u} \cdot \nabla h \\ &= -\operatorname{div}(h\mathbf{u}).\end{aligned}$$

Integrating over Ω and using the divergence theorem then gives

$$\frac{d}{dt} \frac{1}{2} \|\mathbf{q}\|_{1/(\gamma-1)}^2 = - \int_{\partial\Omega} h\mathbf{u} \cdot \mathbf{n} dS.$$

Hence, if $\mathbf{u} = 0$ along $\partial\Omega$, then the integral is zero, and the induced norm is conserved.

4.4.4 Vector-valued POD modes

We begin by nondimensionalizing the equations (4.30), scaling the velocities u, v by the freestream velocity U , the local sound speed by the ambient sound speed a_∞ , x and y by a length L , and time by L/U . The equations become

$$\begin{aligned}u_t + uu_x + vu_y + \frac{1}{M^2} \frac{2}{\gamma-1} aa_x &= \frac{1}{\operatorname{Re}_L} (u_{xx} + u_{yy}) \\ v_t + uv_x + vv_y + \frac{1}{M^2} \frac{2}{\gamma-1} aa_y &= \frac{1}{\operatorname{Re}_L} (v_{xx} + v_{yy}) \\ a_t + ua_x + va_y + \frac{\gamma-1}{2} a(u_x + v_y) &= 0,\end{aligned}\tag{4.40}$$

where $\operatorname{Re}_L = UL/\nu$ and $M = U/a_\infty$. This nondimensionalization is particularly useful, because the Mach number appears in the equations. Thus, M will also appear in Galerkin projections, and we may investigate its effect on the resulting reduced-order models. Note that by scaling x and y by different quantities (e.g., scale x by cavity length L and y by momentum thickness θ), we introduce another nondimensional parameter, the ratio of these lengths. For the cavity flow, this procedure may be used to investigate effects of L/θ_0 , for instance, but in this thesis we consider only the effects of M and Re_L . Writing $\mathbf{q} = (u, v, a)$, the equations may be written

$$\dot{\mathbf{q}} = \frac{1}{\operatorname{Re}_L} L(\mathbf{q}) + \frac{1}{M^2} Q_1(\mathbf{q}, \mathbf{q}) + Q_2(\mathbf{q}, \mathbf{q})\tag{4.41}$$

where

$$L(\mathbf{q}) = \begin{pmatrix} u_{xx} + u_{yy} \\ v_{xx} + v_{yy} \\ 0 \end{pmatrix}, \quad Q_1(\mathbf{q}^1, \mathbf{q}^2) = -\frac{2}{\gamma-1} \begin{pmatrix} a^1 a_x^2 \\ a^1 a_y^2 \\ 0 \end{pmatrix},\tag{4.42}$$

$$Q_2(\mathbf{q}^1, \mathbf{q}^2) = - \begin{pmatrix} u^1 u_x^2 + v^1 u_y^2 \\ u^1 v_x^2 + v^1 v_y^2 \\ u^1 a_x^2 + v^1 a_y^2 + \frac{\gamma-1}{2} a^1 (u_x^2 + v_y^2) \end{pmatrix}. \quad (4.43)$$

Next, we expand \mathbf{q} in terms of POD modes, as

$$\mathbf{q}(\mathbf{x}, t) = \bar{\mathbf{q}}(\mathbf{x}) + \sum_{j=1}^n a_j(t) \varphi_j(\mathbf{x}), \quad (4.44)$$

where $\bar{\mathbf{q}}$ is fixed, and typically taken to be the mean of all the snapshots used for POD. Recall that $\bar{\mathbf{q}}$ must be subtracted from the original data before the POD modes are computed, as described in section 4.1.4. The resulting Galerkin equations are given (see section 4.2) by

$$\begin{aligned} \dot{a}_k &= \frac{1}{\text{Re}_L} b_k^1 + \frac{1}{M^2} b_k^2 + b_k^3 \\ &+ \sum_{i=1}^n \left(\frac{1}{\text{Re}_L} L_{ik}^1 + \frac{1}{M^2} L_{ik}^2 + L_{ik}^3 \right) a_i \\ &+ \sum_{i,j=1}^n \left(\frac{1}{M^2} Q_{ijk}^1 + Q_{ijk}^2 \right) a_i a_j, \end{aligned} \quad (4.45)$$

where the coefficients

$$\begin{aligned} b_k^1 &= \langle L(\bar{\mathbf{q}}), \varphi_k \rangle & L_{ik}^1 &= \langle L(\varphi_i), \varphi_k \rangle \\ b_k^2 &= \langle Q_1(\bar{\mathbf{q}}, \bar{\mathbf{q}}), \varphi_k \rangle & L_{ik}^2 &= \langle Q_1(\bar{\mathbf{q}}, \varphi_i) + Q_1(\varphi_i, \bar{\mathbf{q}}), \varphi_k \rangle \\ b_k^3 &= \langle Q_2(\bar{\mathbf{q}}, \bar{\mathbf{q}}), \varphi_k \rangle & L_{ik}^3 &= \langle Q_2(\bar{\mathbf{q}}, \varphi_i) + Q_2(\varphi_i, \bar{\mathbf{q}}), \varphi_k \rangle, \\ \\ Q_{ijk}^1 &= \langle Q_1(\varphi_i, \varphi_j), \varphi_k \rangle \\ Q_{ijk}^2 &= \langle Q_2(\varphi_i, \varphi_j), \varphi_k \rangle \end{aligned}$$

are constants which may be computed before solving the reduced system. We use the inner product from section (4.4.3) (with $\alpha = 1$) both for computing the POD modes and for the Galerkin projection.

The equations (4.45) represent the reduced-order model of the isentropic Navier-Stokes equations when *vector-valued* modes are used. They are analogous to equations (4.36) for scalar modes. Note that (4.45) is a system of n equations, while (4.36) is a system of $3n$ equations, where n is the number of modes used in the Galerkin projection. Thus, it is reasonable to expect that lower-order models will be possible with (4.45) than with (4.36). For the cavity flow, this is indeed the case, as we shall see in chapter 5.

Chapter 5

Low-order Models of Cavity Oscillations

The model-reduction techniques discussed in the previous chapter are particularly well suited to cavity flows. First, the dynamical behavior of cavity flows is relatively simple, and exhibits qualitative features of low-dimensional dynamical systems (e.g., bifurcations, limit cycles), so it is reasonable to expect that a low-dimensional description is possible. Second, as mentioned in the introduction, one of the main reasons one is interested in modeling is to better understand how to control a flow. In many situations, the goal of control is to drive the flow into a completely different state—for instance, relaminarization of a turbulent flow—which no longer resembles the original, uncontrolled flow. In these situations, the POD/Galerkin method may not be suitable, since the POD modes capture only the limited portion of phase space that is spanned by the snapshots. For the cavity flow, however, we expect the controlled flow to have the same general flow features of the uncontrolled flow: a shear layer will still span the cavity, and will still amplify disturbances, but the amplitude of the oscillations will be smaller, or ideally, will vanish.

The goal of this chapter is to apply the POD/Galerkin method to the data from our simulations, to develop reduced-order models for the cavity flow. These models are suitable for bifurcation analysis, but do not yet include effects of actuation, and so are not yet directly suitable for control design or analysis. We use both scalar-valued and vector-valued POD modes, and show that the vector-valued method has significant advantages over the scalar-valued method. Throughout, we focus on two runs from table 3.1: runs L2 and H2. Both of these runs are oscillating in shear-layer mode, but run L2 has oscillations at both of the first two Rossiter frequencies, while run H2 has oscillations only at Rossiter Mode II.

5.1 Scalar-valued modes

All of the results in this section pertain to the methods for scalar-valued POD modes, discussed in section 4.4.2.

| Run | L/D | L/θ | Re_θ | istart | iend | iskip |
|------|-------|------------|-------------|--------|--------|-------|
| L2 | 2 | 52.8 | 56.8 | 20,750 | 44,000 | 250 |
| H2 | 2 | 58.4 | 68.5 | 70,000 | 80,000 | 200 |
| TK4b | 4 | 60.2 | 58.8 | 30,000 | 45,000 | 200 |

Table 5.1: Parameters for different runs considered, along with the timesteps of the first and last snapshots (istart, iend) and number of timesteps between snapshots (iskip).

5.1.1 POD modes

We compute POD modes for each flow variable separately, according to the expansion

$$q(x, y, t) = \bar{q}(x, y) + \sum_{k=1}^n q_k(t) \tilde{q}_k(x, y) \quad (5.1)$$

where q is any one of $\{u, v, h, \omega\}$, $\tilde{q}_k(x, y)$ are the POD modes, $q_k(t)$ the time coefficients, and the mean \bar{q} is taken to be the time average of the snapshots. The method of snapshots is used, and the matrix U from equation (4.13) is saved so that it need not be recomputed if one wishes to enlarge the ensemble of snapshots.

For the computation of scalar-valued POD modes in this section, snapshots are first interpolated onto a uniform grid (x_i, y_j) , with grid spacing $(\Delta x, \Delta y)$, and the inner product used is the standard Euclidean inner product, given by

$$\langle f, g \rangle = \sum_{i,j} f(x_i, y_j) g(x_i, y_j) \Delta x \Delta y, \quad (5.2)$$

for any functions f, g . The uniform grid is coarser than the original grid in the DNS, and the domain is truncated. For runs with $L/D = 2$, the coarse grid has 101×51 gridpoints inside the cavity (for $(x, y) \in [0, 2] \times [-1, 0]$), and 201×101 gridpoints above the cavity (for $(x, y) \in [-1, 3] \times [0, 2]$). Spatial derivatives are computed on the fine grid and then interpolated onto the coarse grid, for better accuracy in the Galerkin equations.

The snapshots used for each set of POD modes are listed in table 5.1, along with the relevant parameter values. We also compute POD modes for a third run, listed in table 3.1 as TK4b, which will be used later to investigate the relative importance of the parameters L/D and L/θ_0 . Figure 5.1 shows the v -velocity at a point in the shear layer, and indicates the times where the snapshots were taken. Snapshots for run L2 included more of the developing region, as shown.

Run L2

Figure 5.2 shows the eigenvalues λ_k for the POD modes for run L2. Recall that the eigenvalue λ_k represents the “energy” captured by POD mode k , in the sense of the

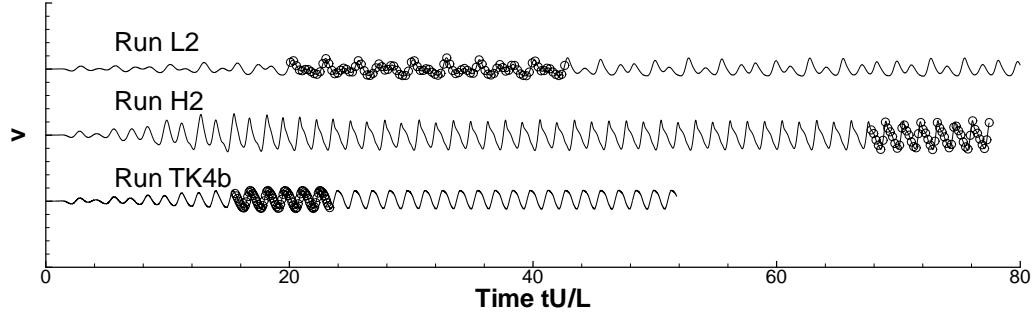


Figure 5.1: Normal velocity at a point in the shear layer, for each of the three runs; (o) indicates where snapshots are taken.

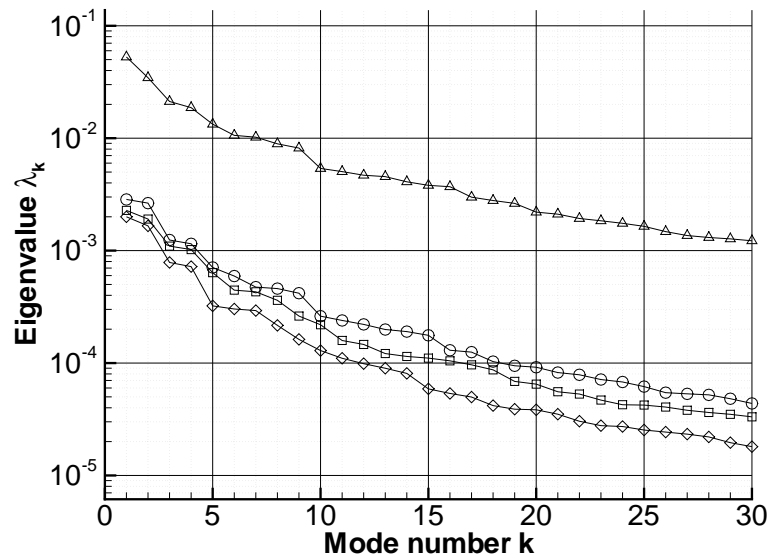


Figure 5.2: Eigenvalues from POD of run L2: u (o), v (□), h (◊), and ω (Δ).

| Mode # | % energy (u) | % energy (v) | % energy (h) | % energy ω |
|--------|------------------|------------------|------------------|-------------------|
| 1 | 20.85 | 21.39 | 25.64 | 20.37 |
| 2 | 19.34 | 17.92 | 21.28 | 13.33 |
| 3 | 9.08 | 10.29 | 10.06 | 8.19 |
| 4 | 8.41 | 9.59 | 9.24 | 7.22 |

Table 5.2: Fraction of energy captured by each POD mode, run L2.

induced norm $\|\cdot\|^2 = \langle \cdot, \cdot \rangle$, which here is given by (5.2), where each flow variable (u, v, h, ω) has its own norm. Note that the vorticity has significantly more energy, since differentiation amplifies the small scales. The velocities u, v have more energy than the thermodynamic variable h , and all variables fall off fairly rapidly, with the energy decreasing by an order of magnitude after only 10 modes. The fraction of the total energy captured by each of the first 4 modes is indicated in table 5.2.

The mean of the snapshots is shown in figure 5.3, and shows the shear layer spanning the cavity, with a steady vortex in the downstream half of the cavity.

The first 4 POD modes are shown in figures 5.4–5.7. The separate POD modes for the individual variables all have similar features: Modes 1 and 2 have slightly less than one full wavelength across the shear layer, corresponding to Rossiter Mode I (see section 3.2.4), and modes 3 and 4 have slightly less than two wavelengths across the shear layer, corresponding to Rossiter Mode II. This correspondence is also confirmed by the time coefficients $q(t)$ in (5.1): the time coefficients are approximately sinusoidal, with the first two coefficients at the first Rossiter frequency, and the next two coefficients at the second Rossiter frequency. Note also that the POD modes arise in pairs, out of phase by 90° , much like sine and cosine, with Modes 1 and 2 forming one pair, and Modes 3 and 4 forming another. (Note that the sign of the POD modes is arbitrary.)

Run H2

The POD modes for run H2 are computed the same way, and the eigenvalues are shown in figure 5.8. The energy falls off much more steeply, dropping an order of magnitude after the first four POD modes. This faster dropoff is to be expected, since run L2 has a more complicated behavior. Also note the pairwise dropoff of the energy. The percent energy captured in each mode for the first four modes is given in table 5.3.

The mean and first four POD modes are plotted in figures 5.9–5.13. From the mean, it is apparent that the steady vortex in the rear of the cavity is significantly stronger than in run L2. Also, by contrast with run L2, POD modes 1 and 2 have nearly *two* full wavelengths in the shear layer, corresponding to Rossiter Mode II. Again, this correspondence is confirmed by the frequency of the time coefficients. POD modes 3 and 4 contain smaller spatial scales, possibly corresponding to a higher Rossiter mode, or possibly higher harmonics of a lower Rossiter mode. (It is not possible to obtain accurate spectra for the higher frequencies with the

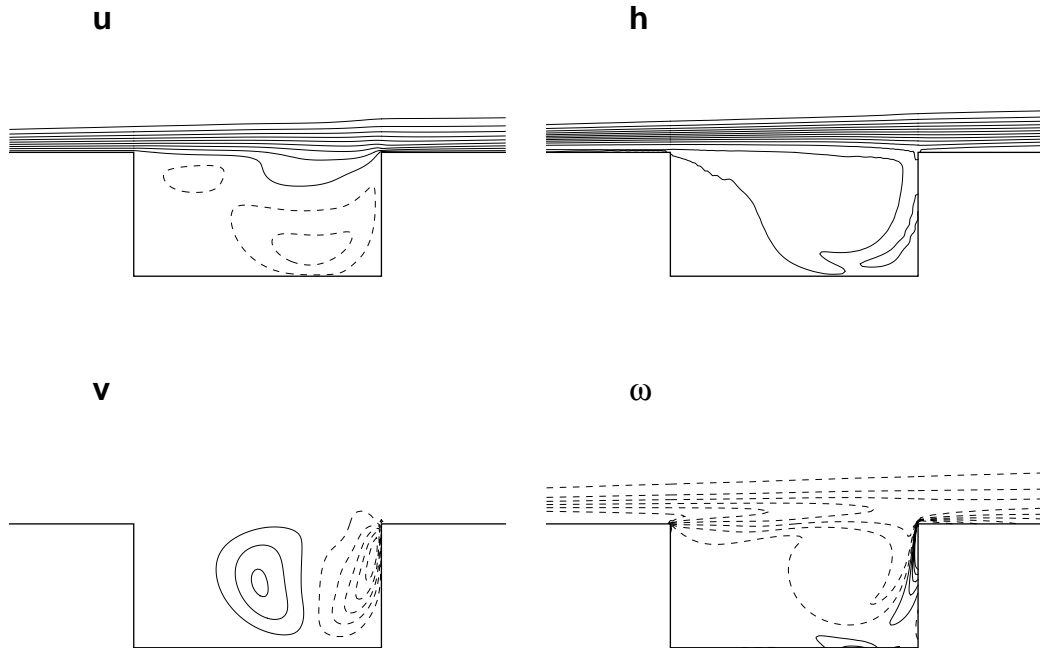


Figure 5.3: Mean from run L2. Each plot has 14 contours equally spaced with $u \in [-0.2, 0.61]$, $v \in [-0.2, 0.2]$, $h \in [2.49, 2.57]$, and $\omega \in [-5, 3]$. Negative contours are dashed.

| Mode # | % energy (u) | % energy (v) | % energy (h) | % energy (ω) |
|--------|------------------|------------------|------------------|-----------------------|
| 1 | 33.41 | 32.94 | 42.76 | 31.35 |
| 2 | 31.04 | 31.09 | 29.48 | 20.38 |
| 3 | 8.62 | 9.32 | 7.55 | 11.92 |
| 4 | 8.29 | 9.25 | 5.49 | 9.35 |

Table 5.3: Fraction of energy captured by each POD mode, run H2.

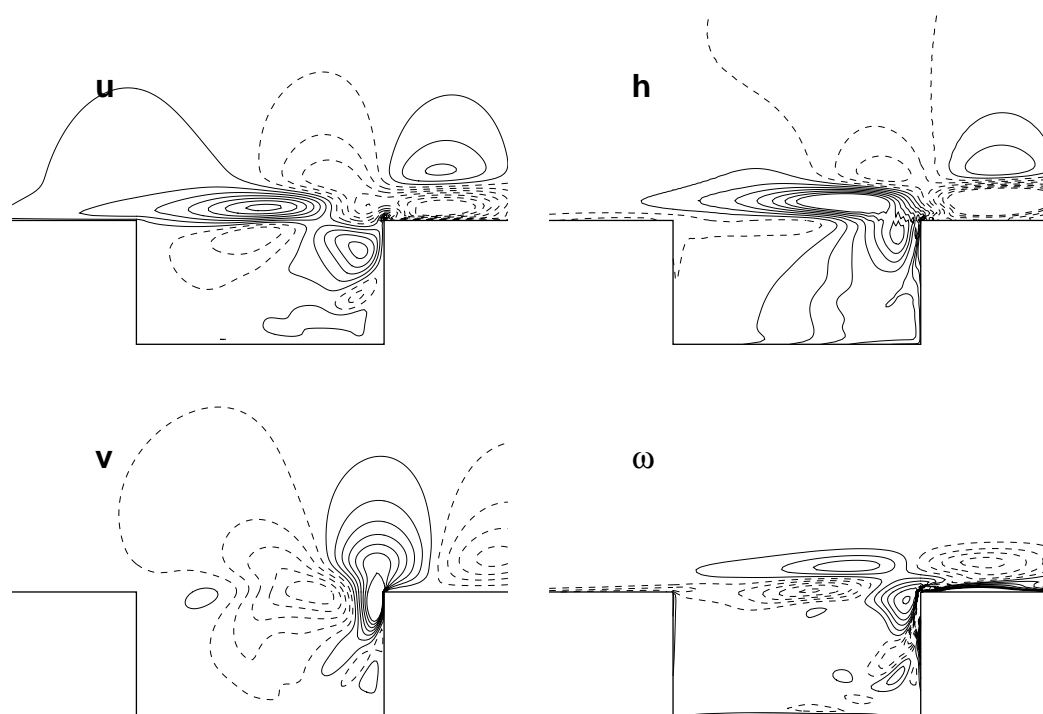


Figure 5.4: Mode 1 from run L2. Each plot has 14 contours equally spaced with $u \in [-1.5, 1.5]$, $v \in [-1.5, 1.5]$, $h \in [-1, 1]$, $\omega \in [-1.5, 1.5]$, with negative contours dashed.

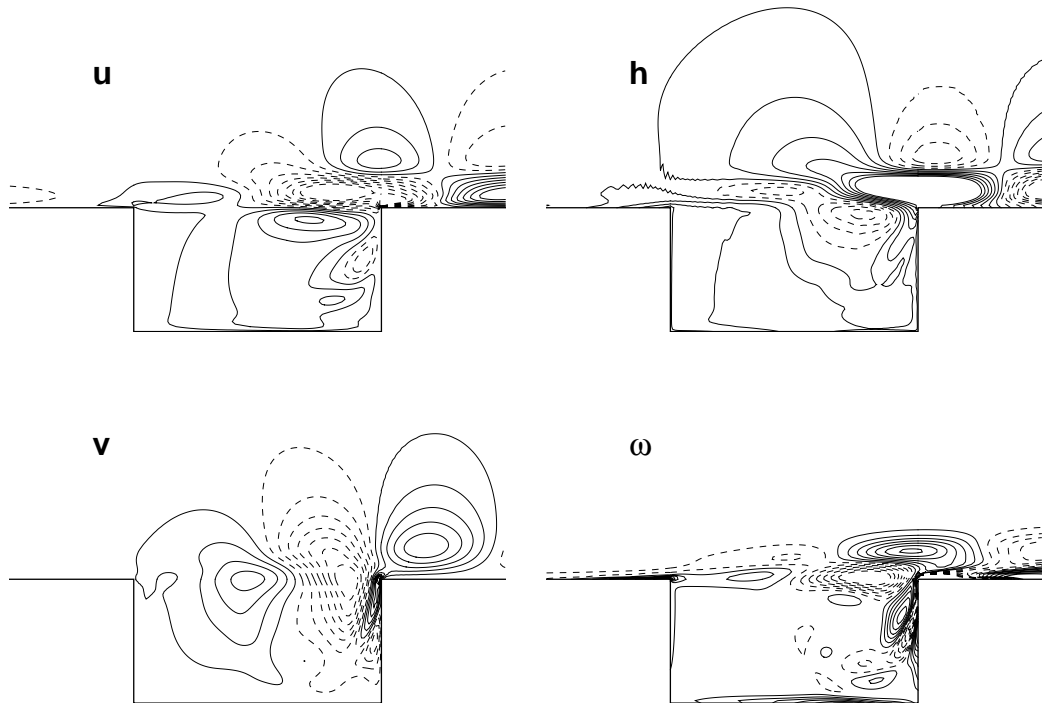


Figure 5.5: Mode 2 from run L2. Contours as in figure 5.4.

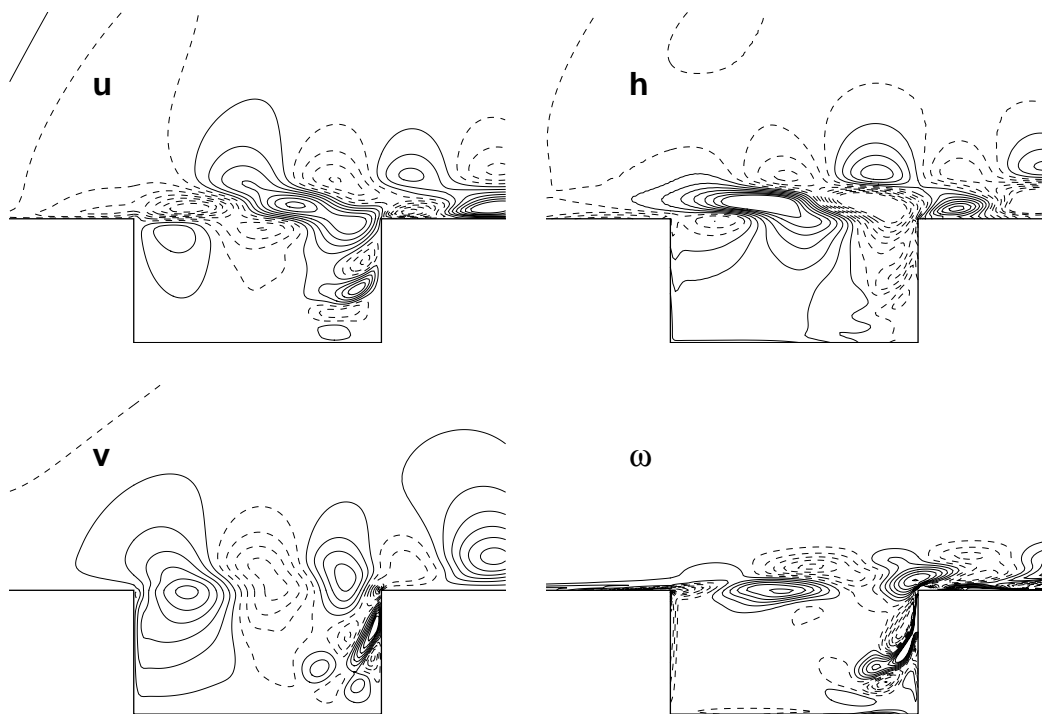


Figure 5.6: Mode 3 from run L2. Contours as in figure 5.4.

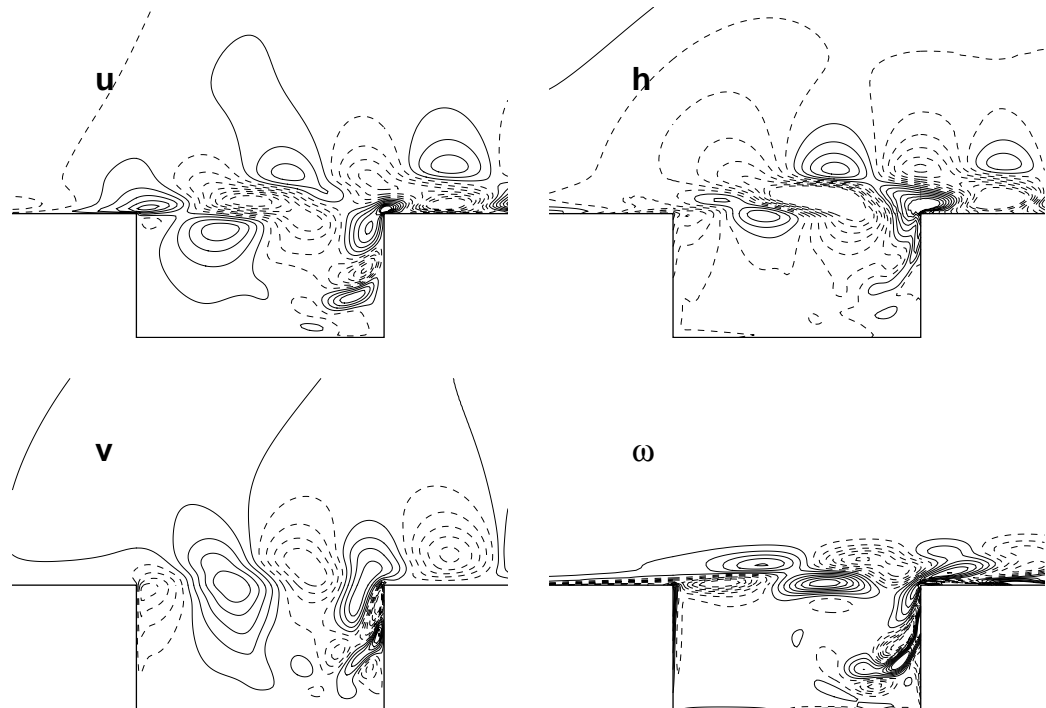


Figure 5.7: Mode 4 from run L2. Contours as in figure 5.4.

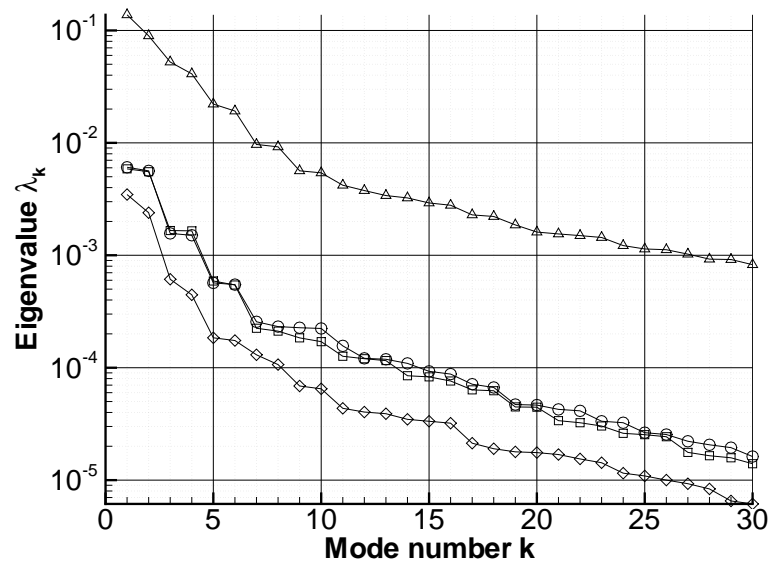


Figure 5.8: Eigenvalues from POD of run H2: u (\circ), v (\square), h (\diamond), and ω (Δ).

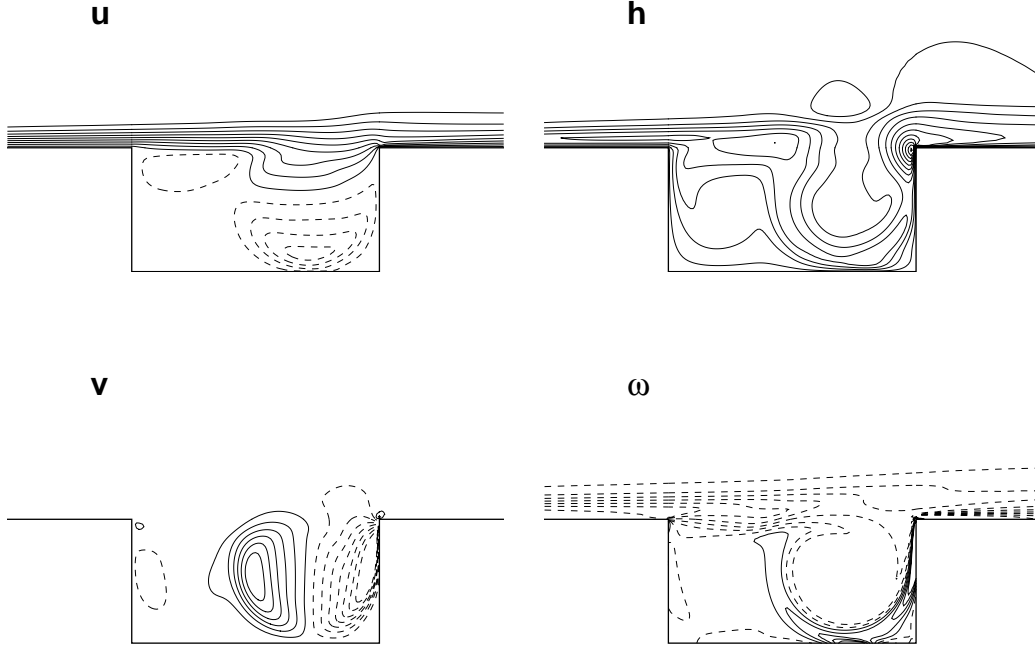


Figure 5.9: Mean from run H2. Each plot has 14 contours equally spaced with $u \in [-0.2, 0.61]$, $v \in [-0.2, 0.2]$, $h \in [2.47, 2.75]$, and $\omega \in [-5, 3]$. Negative contours are dashed.

coarse sampling used for the snapshots, listed in table 5.1.) In general, higher POD modes contain smaller and smaller spatial scales. As before, we notice the same flow structures appearing in pairs of POD modes, shifted in phase by 90° .

Scaling with cavity length

It is interesting to compare (qualitatively) POD modes for different operating conditions, to evaluate the scaling ideas mentioned in section 4.4.4. For instance, do the flow structures scale mainly with L/D or L/θ_0 ? We would expect shear layer structures to scale most strongly with L/θ_0 , since shear layer characteristics do not depend strongly on the cavity depth if the boundary layer is thin enough.

Figure 5.14 supports this idea, that L/D is relatively unimportant, compared to L/θ_0 . Shown is the first v -mode from run L2, next to the corresponding mode from run TK4b, which has nearly the same value of L/θ_0 and Re_θ , but with $L/D = 4$ instead of 2. The pictures are indeed qualitatively similar, especially in the shear-layer region, where the dynamics are important.

This scaling suggests that an appropriate scaling for the variables in the governing equations described in section 4.4.4 is to scale x by L and y by θ_0 , thus introducing the parameter L/θ_0 into the equations. When nondimensionalized in this way, POD modes from runs with different L/D will approximately ‘collapse’

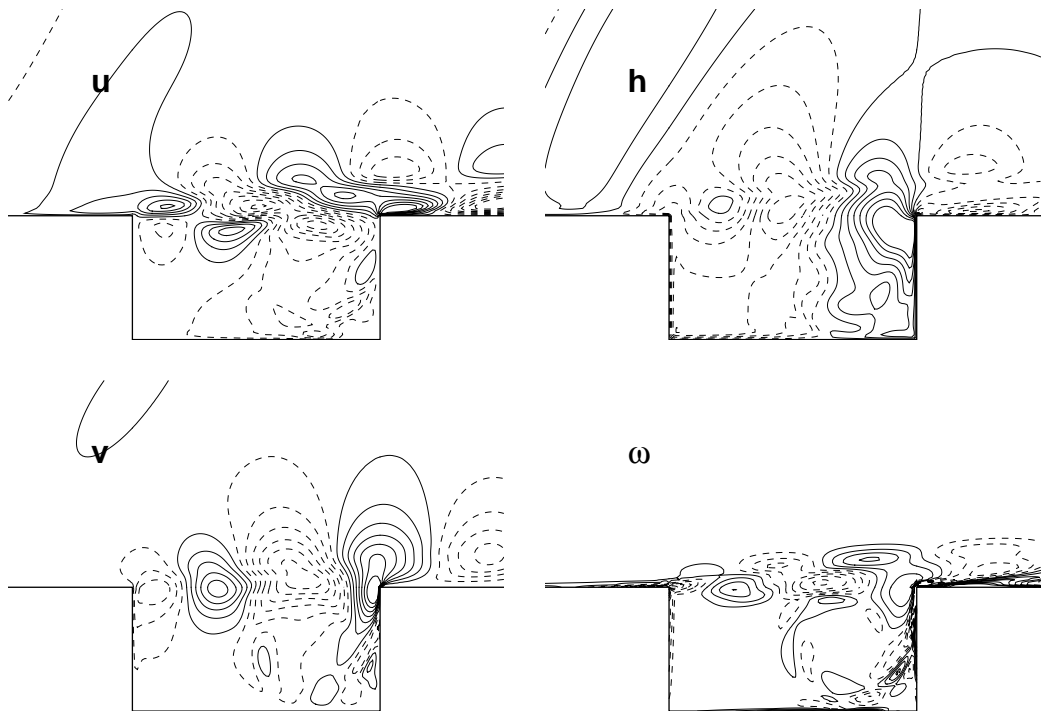


Figure 5.10: Mode 1 from run H2. Contours as in figure 5.4.

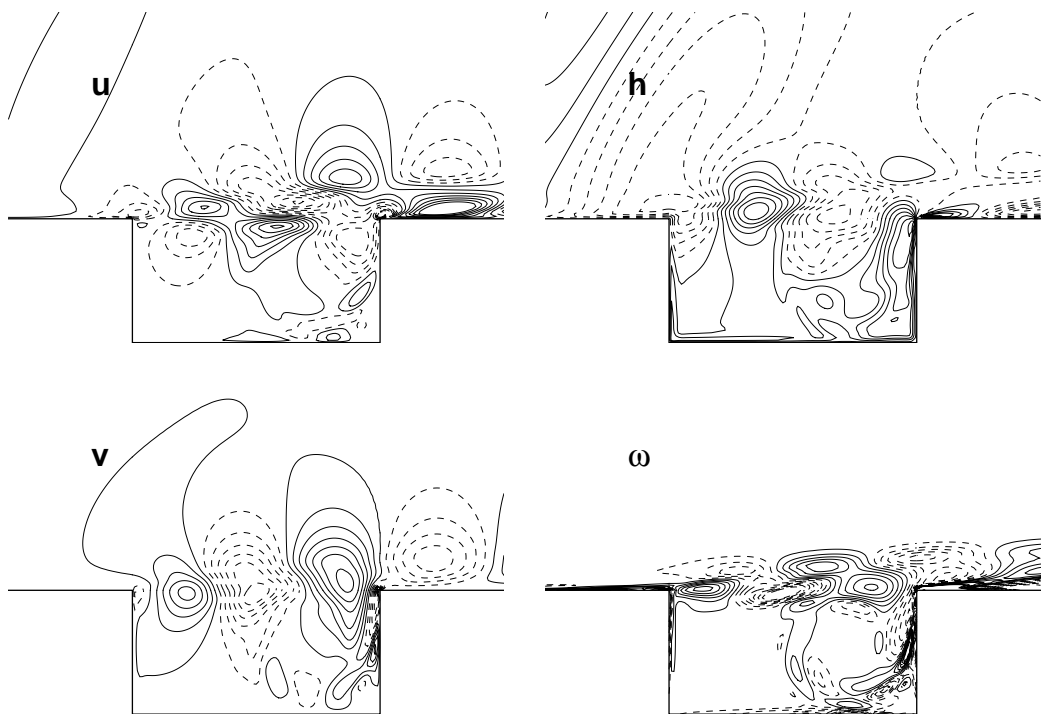


Figure 5.11: Mode 2 from run H2. Contours as in figure 5.4.

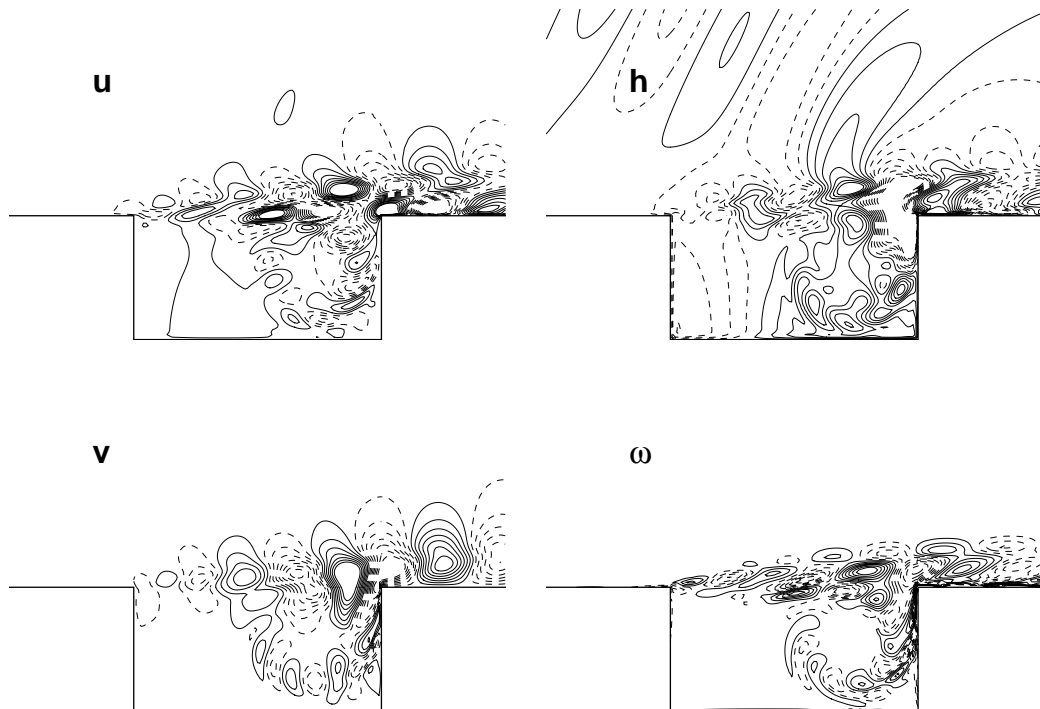


Figure 5.12: Mode 3 from run H2. Contours as in figure 5.4.

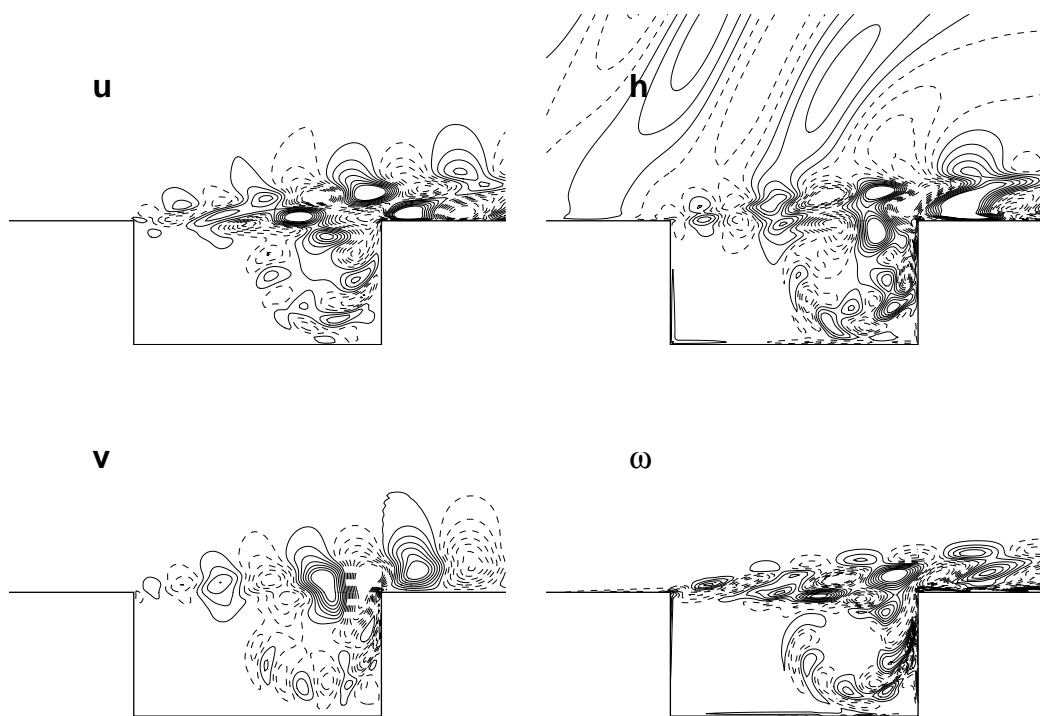


Figure 5.13: Mode 4 from run H2. Contours as in figure 5.4.

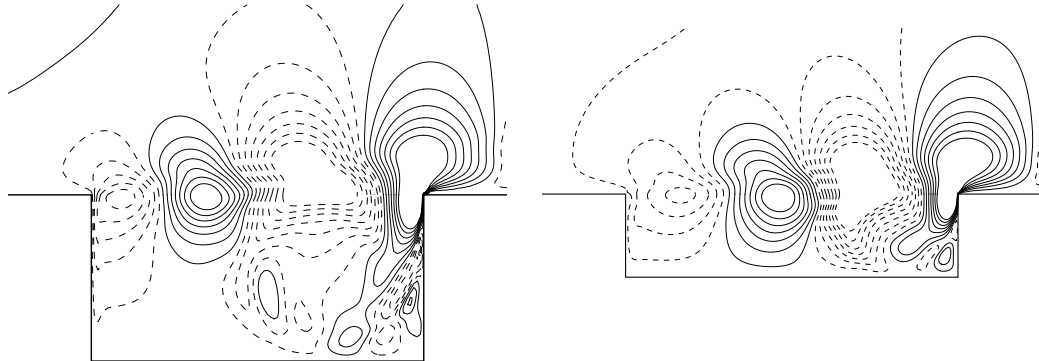


Figure 5.14: Comparison of v -mode 1 from run H2 (left) and TK4b (right).

onto each other,” for instance if one simply ignores the bottom portion of the $L/D = 2$ cavity in figure 5.14. Changing L/D will of course significantly change the resonant acoustic characteristics of the cavity, but the structures in the shear layer are more important for capturing the correct dynamics.

Linear stability modes

The POD modes also look qualitatively similar to the linear stability eigenfunctions discussed in section 3.2.4, although these eigenfunctions are obviously not orthogonal. Figure 5.15 shows a comparison three different types of modes, all of which look qualitatively similar: POD modes 1 and 3 from run L2; modes computed from the locally-parallel linear stability calculation, for the two primary frequencies observed, those of Rossiter modes 1 and 2 ($St = 0.4$ and 0.7 , respectively); and a discrete Fourier transform of the DNS data, for the same two frequencies. (Here we have used a tanh velocity profile for the linear stability calculation.)

5.1.2 Galerkin models

In this section, we discuss low-order models for the cavity, with POD modes taken from run H2. The equations we solve are given in the previous chapter by (4.36). The initial conditions for all runs are obtained by projecting a snapshot from the DNS onto the POD modes, and in this section we always use the snapshot at timestep 70,000, the first in the ensemble used to determine the POD modes.

Effects of higher modes

Figure 5.16 shows the time coefficients of the first four POD modes, for the projection of the DNS, and for several Galerkin simulations, where the number of modes varies from 2 to 20. Note that these correspond to ODEs with 6 to 60 states, since modes for u , v , and h are taken separately. Note that, as mentioned earlier, the time traces are approximately sinusoidal, with the frequency of the first two modes corresponding to the first Rossiter frequency, and the frequency of modes 3 and 4

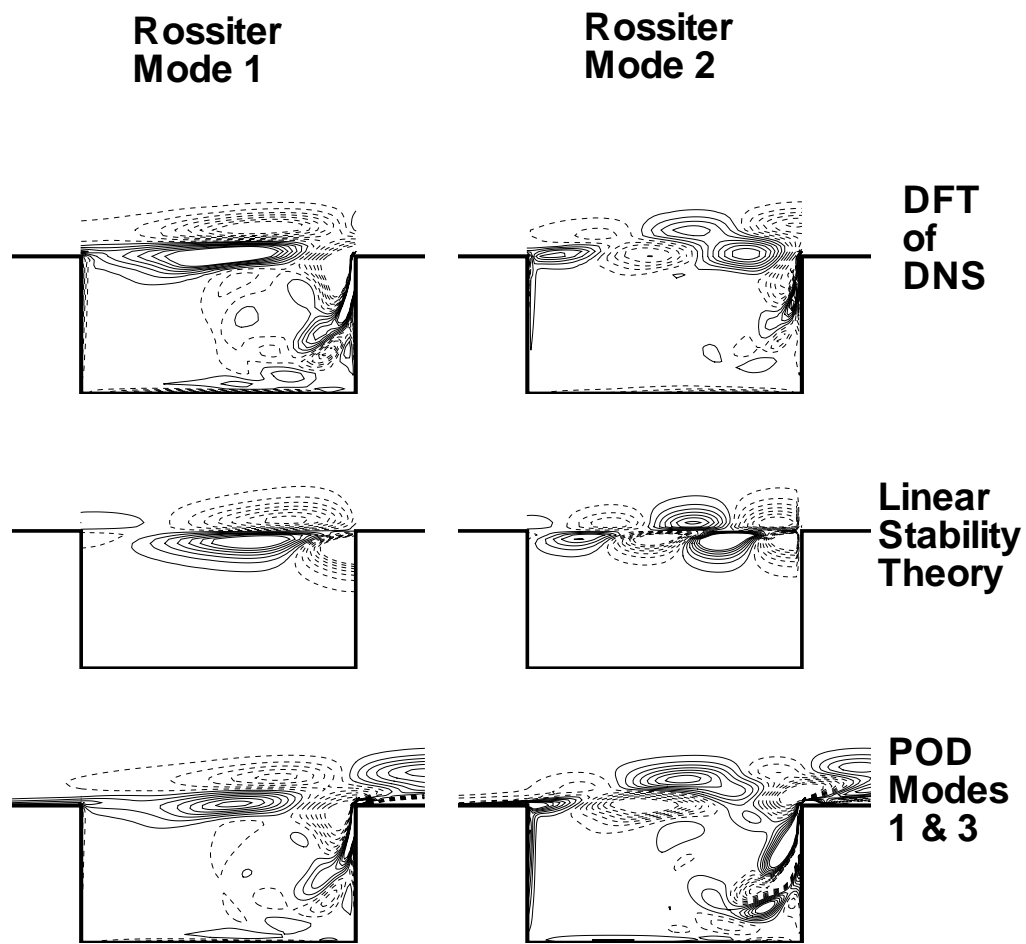


Figure 5.15: Vorticity eigenfunctions computed from linear stability theory, for first 2 Rossiter modes ($St = 0.4, 0.7$); discrete Fourier transform of DNS for the same frequencies; and comparison with vorticity POD modes 1 and 3 for run L2.

corresponding to the second Rossiter frequency. All of the Galerkin models track the DNS well for the first three or four periods. As we expect, for short times the 20-mode case follows the DNS the closest for the first few periods, but after 6 or 7 periods, all of the models begin to deviate.

The same simulations are shown for longer time in figure 5.17, which demonstrates disastrous long-time results. The 4-mode model grows to an amplitude which is much too large, the 10-mode model eventually blows up, and the 20-mode model demonstrates complicated, chaotic-looking behavior which bears no resemblance to the full DNS solution. Surprisingly, the 2-mode model performs best of all for long time, still growing to an amplitude which is too large, but at least remaining stable, with the same qualitative features as the DNS solution.

The alarming result is that increasing the number of modes does not necessarily improve the long-time accuracy of the simulations, and can even lead to instability. A well-known limitation of POD/Galerkin systems is that while local dynamics are guaranteed to improve by increasing the number of modes, there are no guarantees about the global dynamical behavior, or even the stability of equilibrium points and limit cycles, even if the POD subspace completely contains the space spanned by the snapshots [Rempfer, 2000].

Effects of viscosity

Since many of the important phenomena of cavity oscillations are essentially inviscid (e.g., shear layer instability, acoustic wave propagation), one might expect that the inviscid equations ($\nu = 0$) would model the flow nearly as well as the viscous equations.

Figure 5.18 shows time traces of POD modes 1 and 3, for two different 4-mode Galerkin models, with and without the viscous terms in equation (4.36). The viscous model uses the same value of Re_θ used in the original DNS run.

Both models follow the DNS closely for the first two periods of oscillation, but then the amplitude starts to increase, and the inviscid model starts to perform worse. For longer times, the inviscid calculation eventually blows up, while the viscous model remains stable, at least until $t = 130$, with no sign of blow-up. For the remainder of this thesis, we consider viscous models exclusively, with the viscosity ν determined from Re_θ of the original run.

5.2 Vector-valued modes

In this section, we apply the methods described in section 4.4.4 for obtaining reduced-order models using vector-valued POD modes.

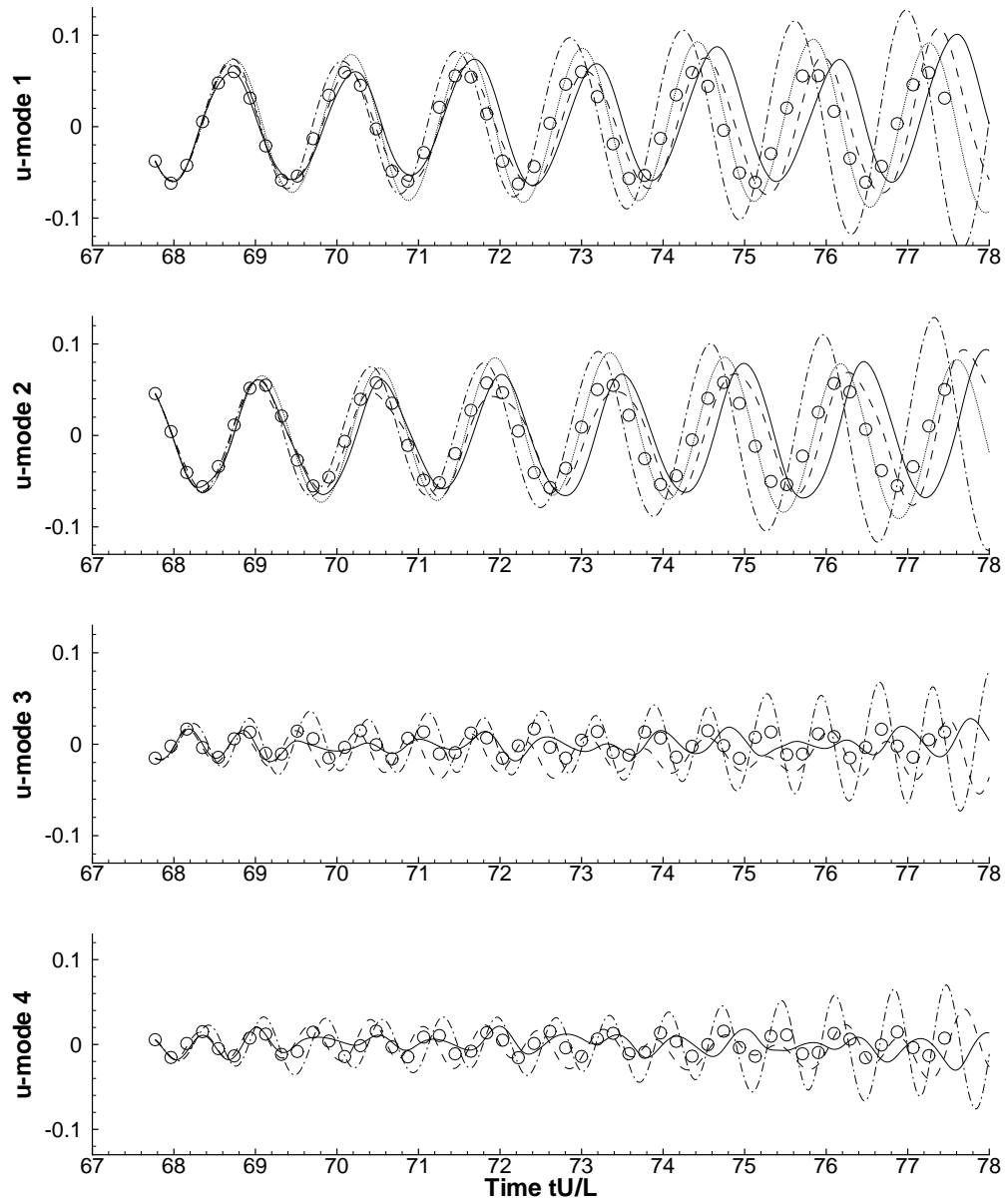


Figure 5.16: Coefficient of u -velocity modes 1–4, for projection of DNS (○), and POD/Galerkin models with 2 modes (····), 4 modes (—··—), 10 modes (----), and 20 modes (—).

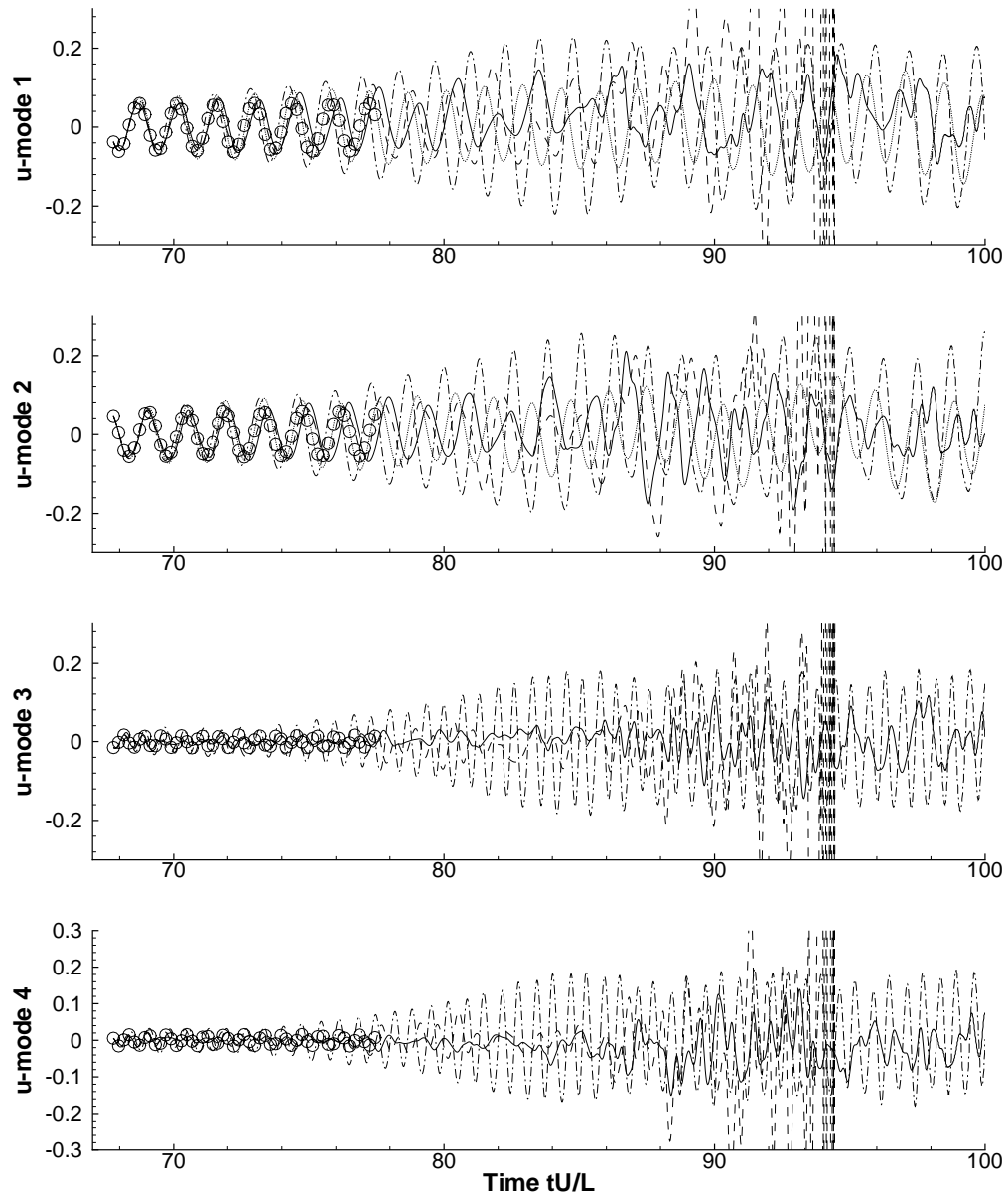


Figure 5.17: Coefficient of u -velocity modes 1–4, same run as in figure 5.16, for longer time. (See figure 5.16 for legend.)

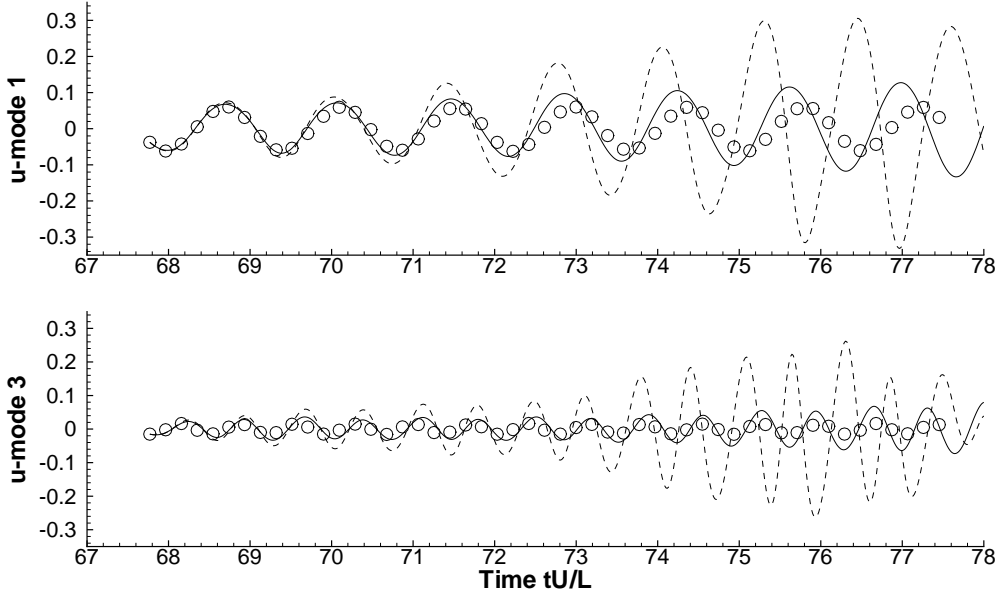


Figure 5.18: Coefficient of u -velocity modes 1 & 3: 4-mode Galerkin simulations with viscosity (—), without viscosity (----), and projection of DNS (○).

5.2.1 POD modes

We compute vector-valued POD modes for the vector of flow variables $\mathbf{q} = (u, v, a)$, obtaining the expansion

$$\mathbf{q}(x, y, t) = \bar{\mathbf{q}}(x, y) + \sum_{k=1}^n q_k(t) \tilde{\mathbf{q}}_k(x, y), \quad (5.3)$$

where $\tilde{\mathbf{q}}_k$ are the POD modes, and now there is only one set of time coefficients q_k . (In the previous section, there was a separate set of time coefficients for each flow variable.) As before, $\bar{\mathbf{q}}(x, y)$ is taken to be the mean of the snapshots used for the POD, though this choice is arbitrary.

In this section, we do not interpolate onto a coarse grid first, but use the original grid from the DNS. However, we use a truncated domain for computing inner products, in particular the domain $\Omega = [0, 2] \times [-1, 0] \cup [-1, 3] \times [0, 2]$, the same region used in the previous section. We use the family of inner products described in section 4.4.3, with $\alpha = 1$ unless otherwise stated (hence using the integral of the stagnation enthalpy as a norm). Because the stretched grid is used, the grid metrics must be included in the sum, so the inner products are computed as

$$\langle \mathbf{q}_1, \mathbf{q}_2 \rangle = \sum_{i,j} \left(u_1 u_2 + v_1 v_2 + \frac{2\alpha}{\gamma - 1} a_1 a_2 \right)_{ij} \frac{dx}{d\xi} \bigg|_i \frac{dy}{d\eta} \bigg|_j \Delta\xi \Delta\eta, \quad (5.4)$$

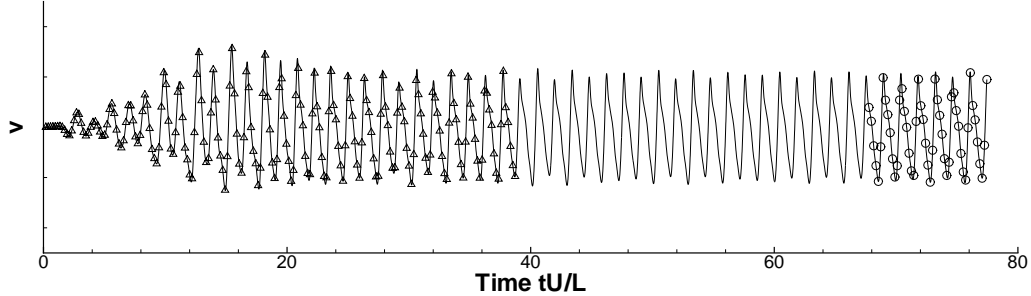


Figure 5.19: Normal velocity at a point in the shear layer, for run H2; (○) indicates where snapshots are taken for transient case, (Δ) for fully-developed case.

where (ξ, η) are coordinates of the uniform computational grid, and $dx/d\xi, dy/d\eta$ are the grid metrics. (Here, subscripts i and j denote evaluation at gridpoint locations x_i and y_j .)

We consider two different ensembles of snapshots for computing the POD modes, shown in figure 5.19, both taken from run H2. For the first set, which we refer to as the “transient” case, we take snapshots while the flow is developing, using 201 snapshots between 0 and 40,000 timesteps. The second set will be referred to as “fully-developed,” and we take 51 snapshots between 70,000 and 80,000 timesteps, the same as used for run H2 in the previous section.

Figure 5.20 shows the eigenvalues of the POD modes for the two cases. As we expect, the energy decay is much slower for the transient POD modes, as more modes are necessary to capture the more complicated flow structures in the developing region. As before, the eigenvalues occur in pairs, but for the transient snapshots, there are additional POD modes corresponding to flow structures which are not oscillating at a particular frequency, as can be seen by looking at the POD modes themselves.

Figure 5.21 shows the first six POD modes for the fully-developed case, and figure 5.22 shows the first six modes for the transient case. Because the modes are vector valued, we can compute any flow quantity from them, and here we plot the vorticity and dilatation, which approximately separates convecting disturbances from acoustic waves. The fraction of fluctuating energy ($\|\mathbf{q} - \bar{\mathbf{q}}\|^2$) for each mode is also shown.

For the fully-developed case, the POD modes clearly occur in pairs, shifted in phase by 90° , as in the previous section, and the first six modes together capture 99.59% of the energy in the fluctuations. For the transient case, the first six modes capture much less of the energy (93.85%), and not all of the modes appear in pairs. In particular, modes 1 and 4 both represent structures which arise as the flow changes from a boundary layer spanning a quiescent cavity (the initial condition), into an oscillating cavity flow, with a steady vortex. For the transient case, modes 2 and 3 form a pair, as do modes 5 and 6. These pairs may be identified objectively by looking for modes with similar energy content. As in the scalar-valued case, higher modes contain smaller and smaller spatial scales, at

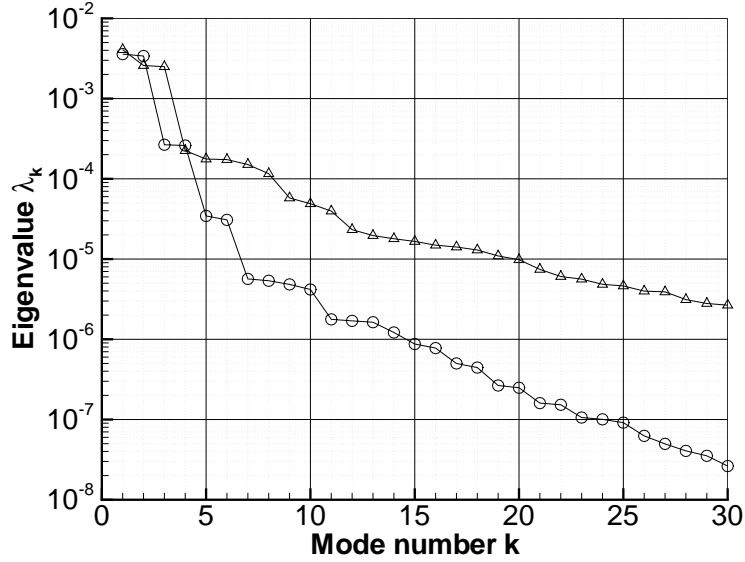


Figure 5.20: Eigenvalues of POD modes, for snapshots taken in transient regime (Δ), and after flow has fully developed (\circ).

higher temporal frequencies, with correspondingly smaller acoustic wavelengths.

The fraction of energy captured by the POD modes does not depend strongly on the ensemble of snapshots chosen: when a different ensemble of snapshots (from the same run) is projected onto the POD modes, the percent energy captured is almost the same, as we expect, since the dominant flow structures remain the same once the initial transient has decayed.

The value of α in (5.4) was varied from 0 to 2.5, and the POD modes were virtually identical for all values of α . This indicates that the energy in the fluctuations is dominated by kinetic energy in the flow variables, rather than internal energy in the thermodynamic variables. The POD modes are not shown, but we investigate Galerkin models using different values of α in the next section.

5.2.2 Galerkin models

We now form reduced-order models using the vector-valued POD modes, using the equations given in the previous chapter by (4.45). As with the scalar-valued modes, the initial condition for the simulations was obtained by projecting a snapshot from the DNS onto the modes.

Fully developed modes

We first examine models obtained from the modes given in figure 5.21. Figure 5.23 shows the results of a simulation using an initial condition from timestep 70,000, the first snapshot of the ensemble used to compute the POD modes, and the same as used for the initial condition in figure 5.17. Note that since the POD modes are

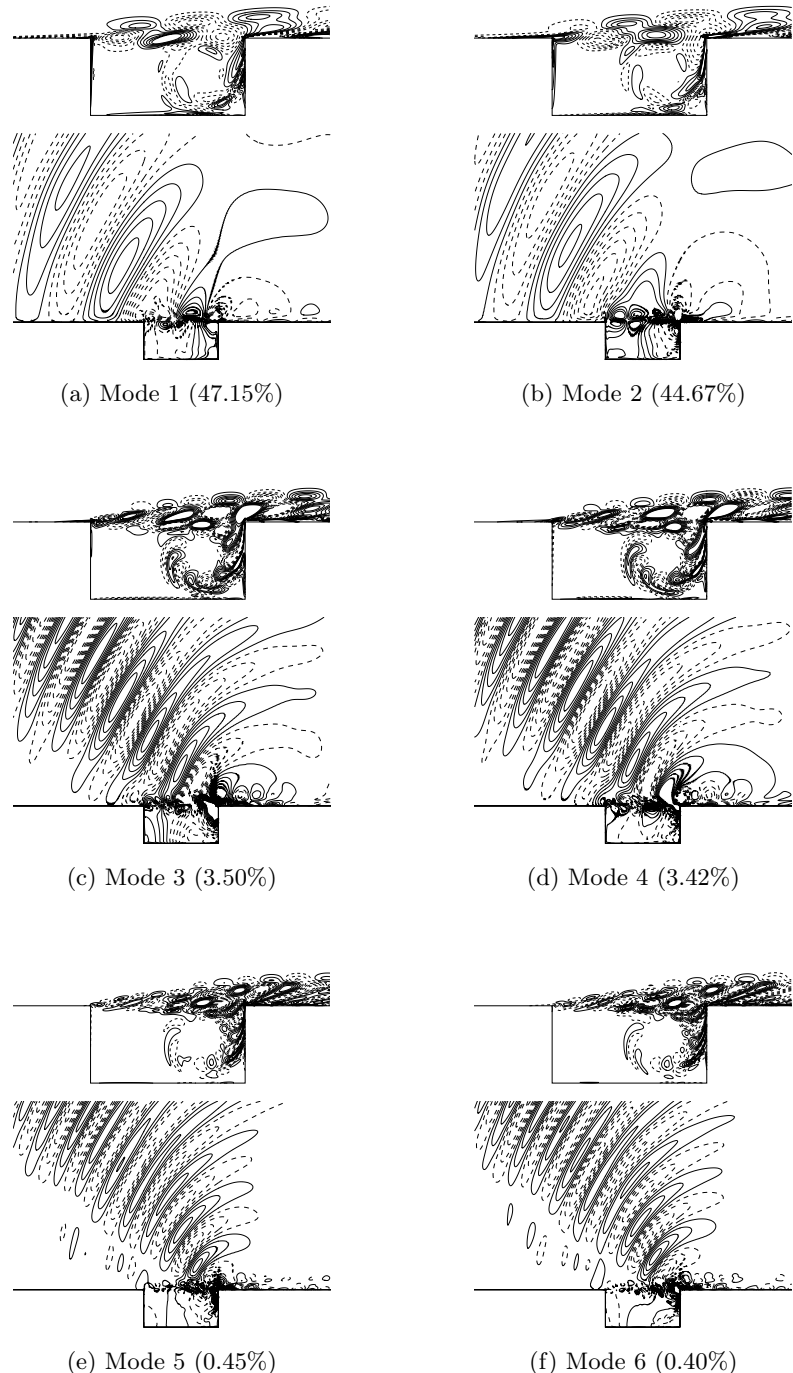


Figure 5.21: Fully developed modes: Vorticity (top) and dilatation (bottom), and percent energy captured, for run H2, with vector-valued POD modes, snapshots from fully developed flow.

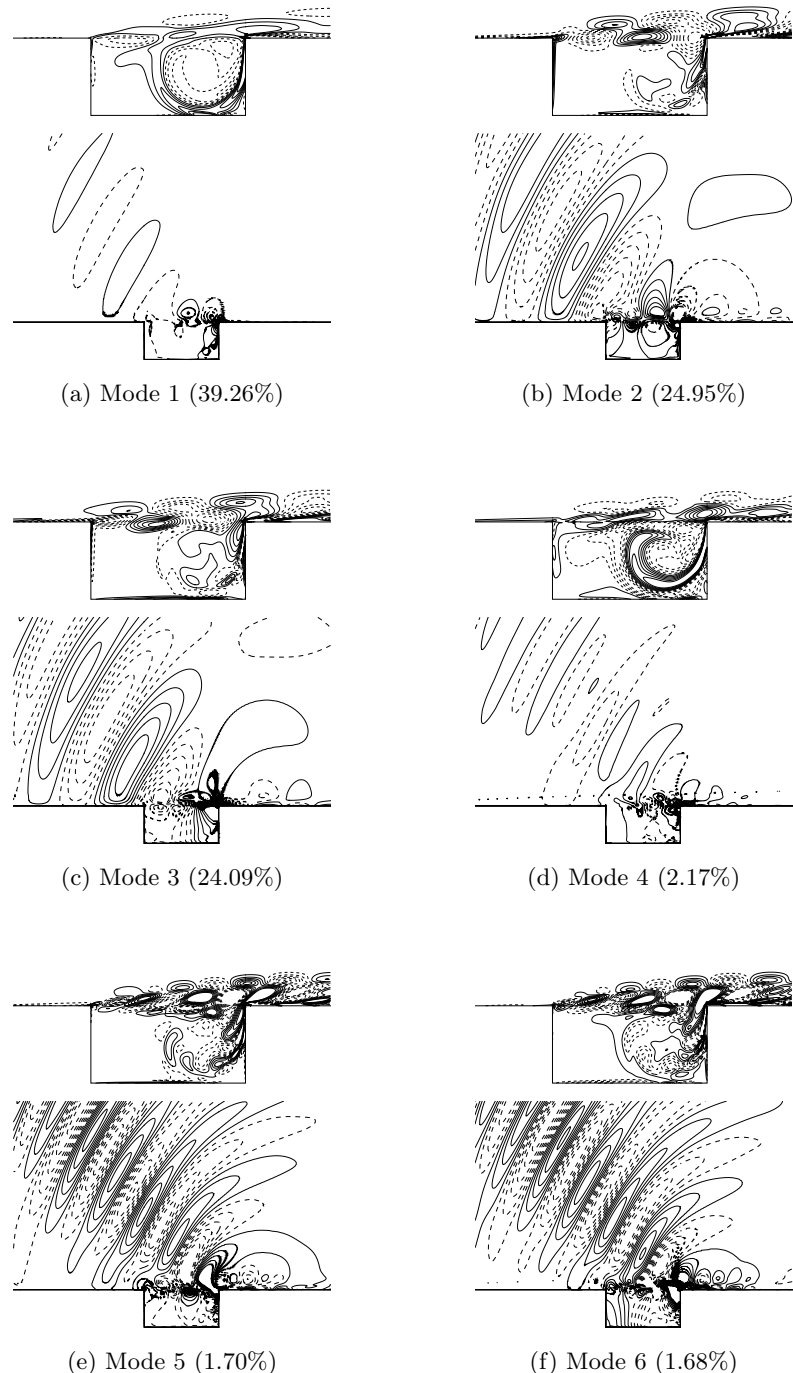


Figure 5.22: Transient modes: Vorticity (top) and dilatation (bottom), and percent energy captured, for run H2, with vector-valued POD modes, snapshots from developing region.

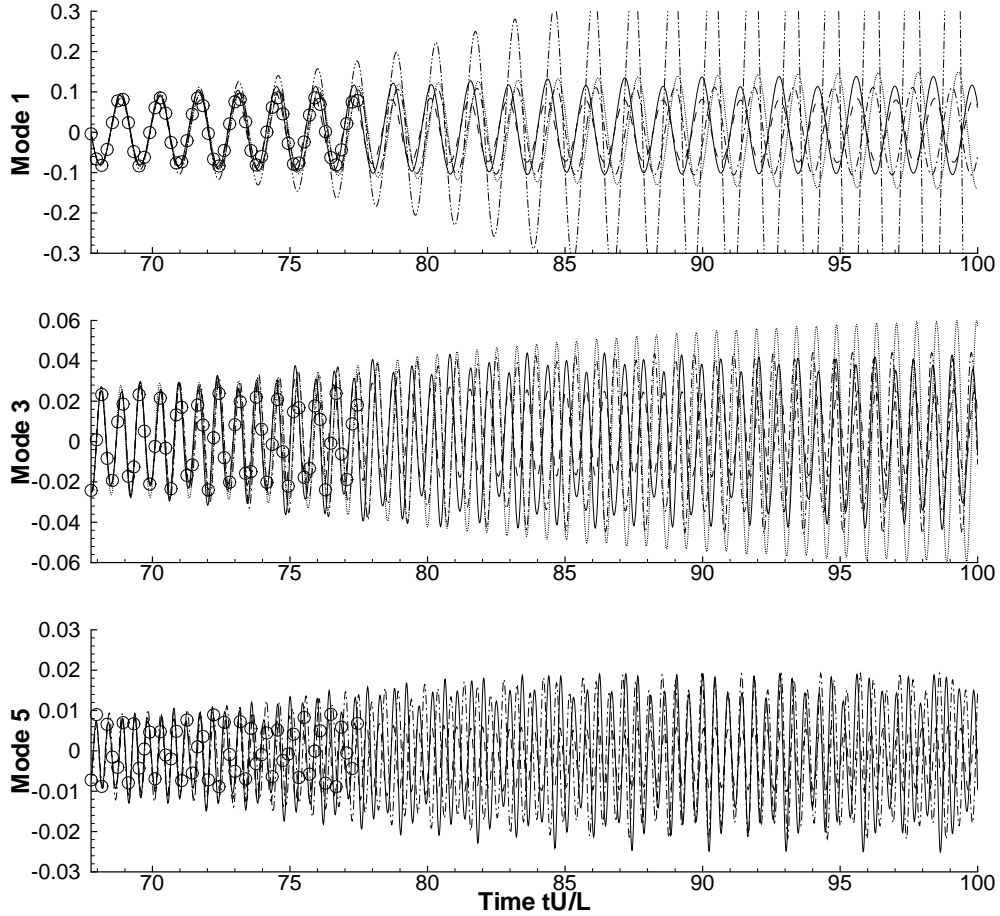


Figure 5.23: Fully-developed modes: Coefficients of POD modes 1, 3, and 5 for Galerkin simulations, starting at timestep 70,000, with 2 modes (—·—), 4 (····), 6 (—·—), 11 (----), and 20 modes (—).

different, one cannot compare the time coefficients directly between the figures, but several qualitative differences are evident.

In figure 5.23, all of the models track well for the first three or four periods. After this, the 2-mode model starts to diverge, increasing in amplitude, but all of the simulations with more modes have good qualitative agreement, even for long times. The amplitude of the limit cycle is accurately captured, and increasing the number of modes does not lead to long-time instability, as it did with the scalar-valued modes shown in figure 5.17. Also note that the number of ODEs to solve here is fewer by a factor of 3 compared to the scalar-valued method.

Figure 5.24 shows the same models started from a different initial condition, the initial snapshot from the DNS at $t = 0$, which is a Blasius boundary layer spanning a quiescent cavity. Here, the short-time agreement is not good, but the qualitative features are correct: oscillations gradually increasing in amplitude, and

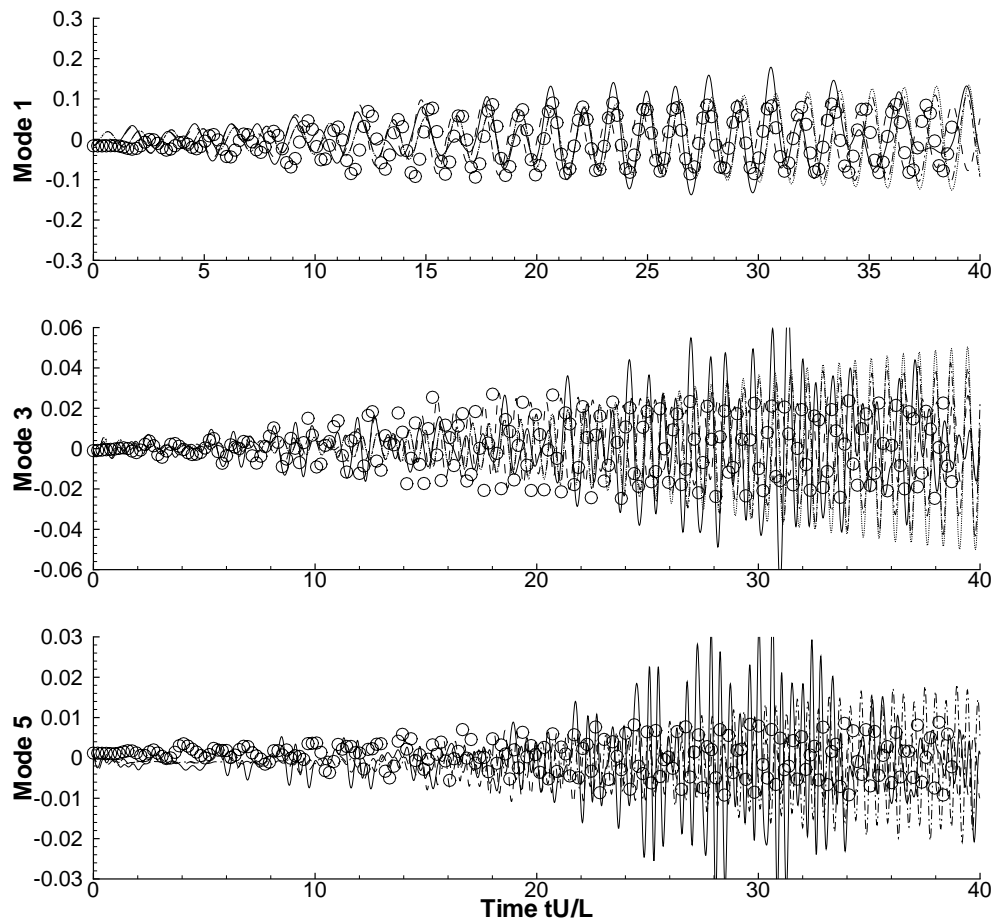


Figure 5.24: Fully-developed modes: Time coefficients for Galerkin simulations, starting at time $t = 0$. Legend as in figure 5.23, except 2-mode simulation not shown.

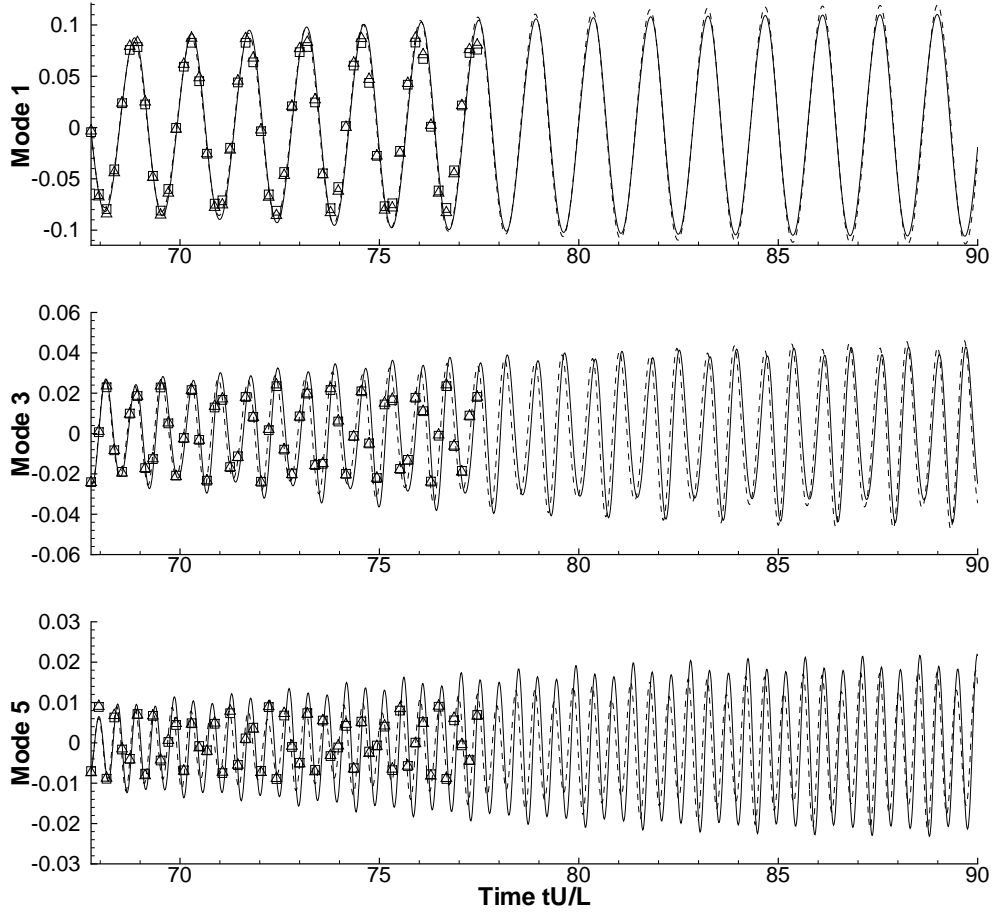


Figure 5.25: Fully-developed modes: Time coefficients, varying α in the inner product. For $\alpha = 0$, projection of DNS (\square), and 6-mode Galerkin simulation (---); for $\alpha = 2.5$, projection of DNS (\triangle) and 6-mode Galerkin (—).

ultimately saturating. It also appears the frequency is correct, at least for mode 1, and it is difficult to tell the frequency content of the higher modes in the DNS, because the sample rate of the snapshots is relatively low. The 20-mode case starts to deviate around time $t = 25$, but it does not blow up (at least for the length of our simulation, which was $t = 120$). All of the other cases capture the final amplitude reasonably well, and increasing the number of modes from 4 to 6 to 11 seems to improve the agreement for the higher modes.

In figure 5.25, we vary the value of α used in the inner product (5.4), from 0, neglecting the thermodynamic variables completely, to 2.5, weighting the thermodynamic variables more strongly. The modes used for these simulations were still the POD modes shown in figure 5.21—as noted earlier, changing α had negligible effect on the POD modes, but the value of α also affects the projection of the equations, which is what we investigate here.

As the figure shows, the projection of the DNS snapshots is very similar for the two inner products, as is the evolution of the different sets of Galerkin equations obtained from the two different projections. As mentioned earlier, this indicates that the energy in the fluctuations is dominated by the kinematic variables, not the thermodynamic variables, which is to be expected for a cold, low-Mach number flow such as this. Since the results are so weakly dependent on α , for the remainder of the section we fix $\alpha = 1.4$.

Transient modes

We now discuss simulations using POD modes from the transient snapshots, shown in figure 5.22. Figure 5.26 shows simulations varying the number of modes between 3 and 15, starting at timestep 70,000. Here, increasing the number of modes to 15 causes the flow to diverge after a few oscillations, unlike for the fully-developed modes (figure 5.23). Nevertheless, all of the other simulations in figure 5.26 track reasonably well for long times, and none of the simulations blow up, as they did for the scalar-valued modes (figure 5.17).

Figure 5.27 shows the same simulations started from time $t = 0$. Here, all of the simulations are again accurate for short times, but both the 10-mode and 15-mode cases deviate for long times. The 3-mode case overshoots in amplitude (both modes 1 and 2), but eventually settles into a more realistic flow (well beyond the time shown in the figure), and the 6-mode case tracks very well for the entire duration of the simulation.

For the simulations performed here, using the POD modes from the developing region gives worse results than using the fully-developed POD modes: more modes are required for qualitatively accurate results, and furthermore, taking more modes tends to make the models unstable. This is surprising, as one might think that the developing POD modes might make Galerkin projections *more* stable: since they contain more information about the transients, they might be better able to correct if the solution started to stray from its steady-state conditions. It is likely that many more modes are necessary, however, given the much slower energy decay shown in figure 5.20. The highest number of modes we tried in our simulations with transient POD modes was 15, and though the first 15 transient POD modes capture 98.57% of the energy in the transient dataset, they presumably capture much less energy for the fully developed oscillations.

5.2.3 Parameter variation

Here we briefly discuss the effect of varying the Mach number M in the Galerkin models. In particular, we investigate how the frequency of oscillation varies as the Mach number is changed, by examining the eigenvalues of the linearized system, which is just the linear part of the governing equations (4.45). For the models in this section, we use POD modes from the fully-developed snapshots, shown in figure 5.21.

The eigenvalues of the linearized system are shown in Figure 5.28, for Galerkin

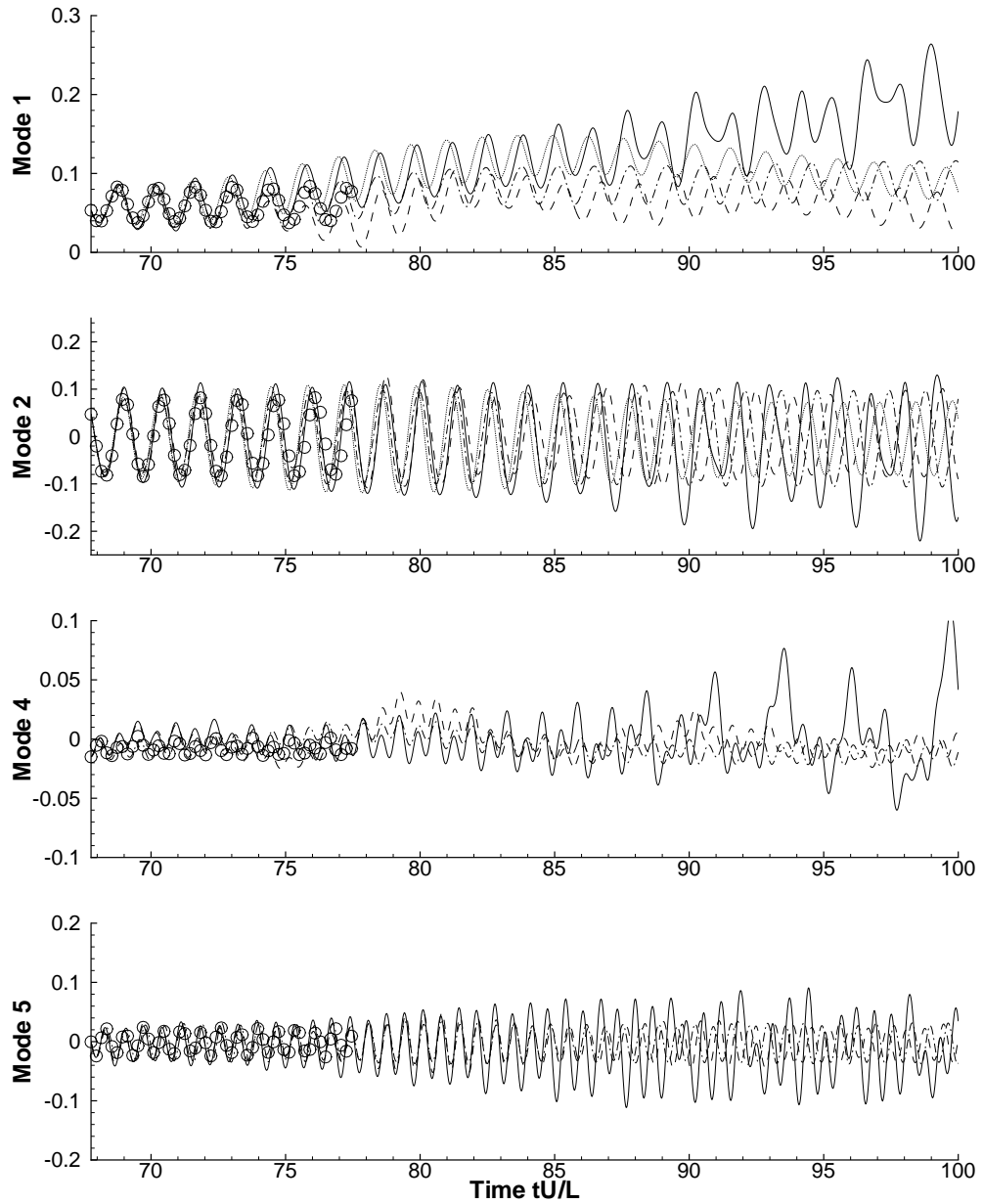


Figure 5.26: Transient modes: Coefficients of POD modes 1, 2, 4, and 5 for Galerkin simulations, starting at timestep 70,000, with 3 modes (····), 6 (··—), 10 (—·—), and 15 modes (—).

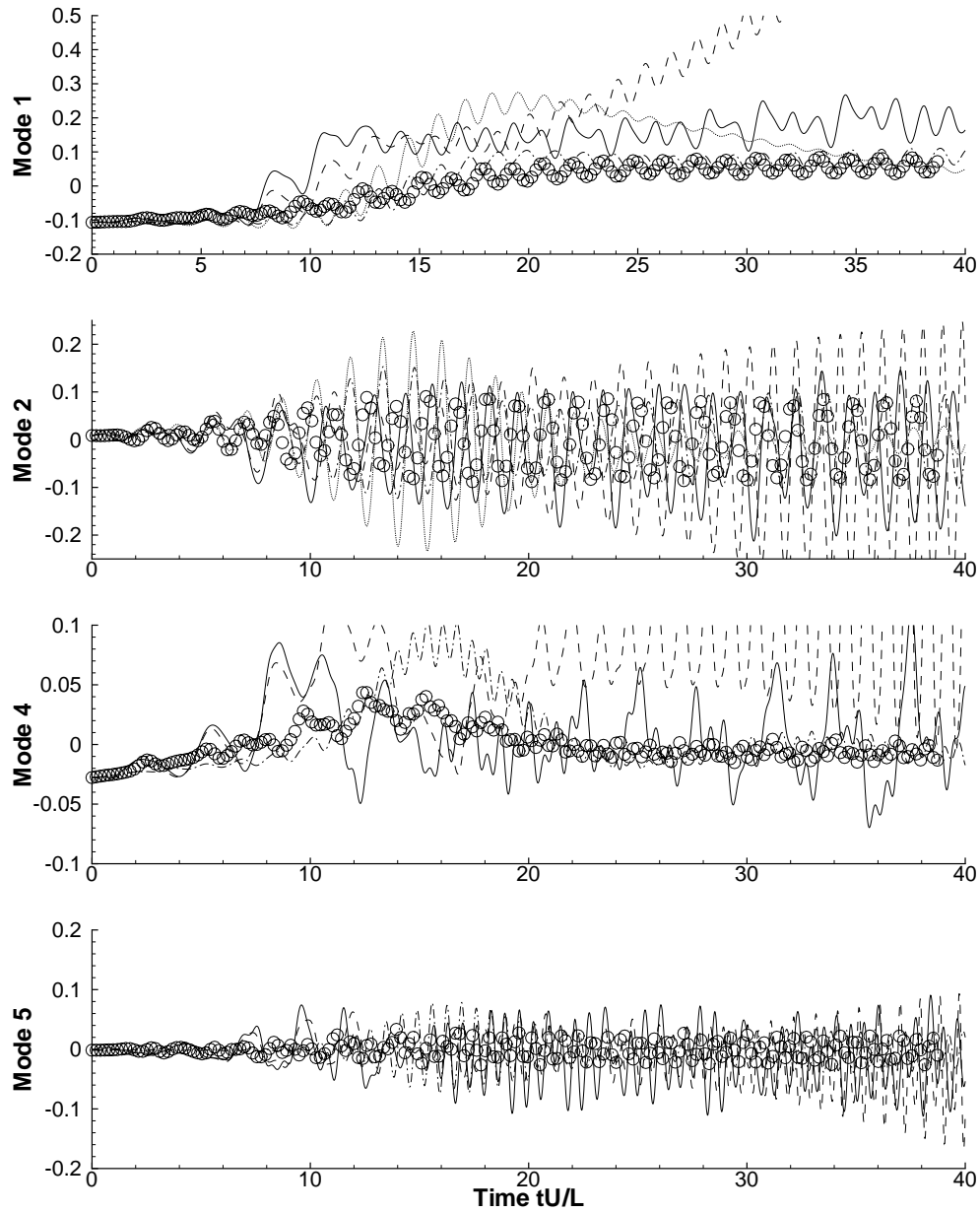


Figure 5.27: Transient modes: Time coefficients for Galerkin simulations, starting at time $t = 0$. Legend as in figure 5.26.

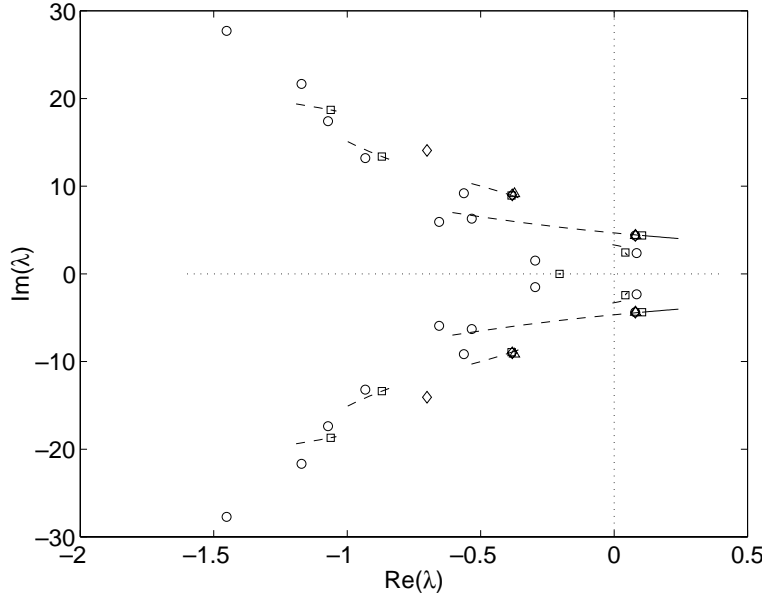


Figure 5.28: Eigenvalues of 4-mode (\triangle), 6-mode (\diamond), 11-mode (\square), and 20-mode (\circ) linearized Galerkin models, at the nominal value $M = 0.6$; and of the 11-mode model with $0.3 < M < 0.6$ (---), and $0.6 < M < 0.9$ (—).

models with 4, 6, 11, and 20 POD modes. The 4- and 6-mode models have one pair of unstable (right-half-plane) eigenvalues, at the frequency of Rossiter mode II. The 10- and 20-mode models have an additional pair of unstable eigenvalues, at the lower frequency of Rossiter mode I. This indicates that Rossiter mode I is still present in the dataset, but at a much smaller energy than Rossiter mode II.

As the Mach number is varied, the eigenvalues move, as shown in figure 5.28. When the Mach number is decreased, the eigenvalues become more stable, which is consistent with observations from the simulations.

Figure 5.29 shows how the frequencies (imaginary parts of the unstable eigenvalues) change as the Mach number is varied. Also plotted are the frequencies measured from the DNS at $M = 0.6$, and the curves of the first two frequencies predicted by Rossiter's formula (3.2), using Rossiter's original values $\gamma = 0.25$, $1/\kappa = 1.75$. The frequencies closely match the frequency measured in the DNS, and capture the same trend with Mach number predicted by Rossiter's model. Note that we do not expect our Galerkin model to be valid very far from the parameter range where the snapshots were taken, since for different parameter values, the flow structures will presumably be different.

5.3 Conclusions

In this chapter, we have compared reduced-order models obtained from POD and Galerkin projection, and in particular we have compared the procedure based

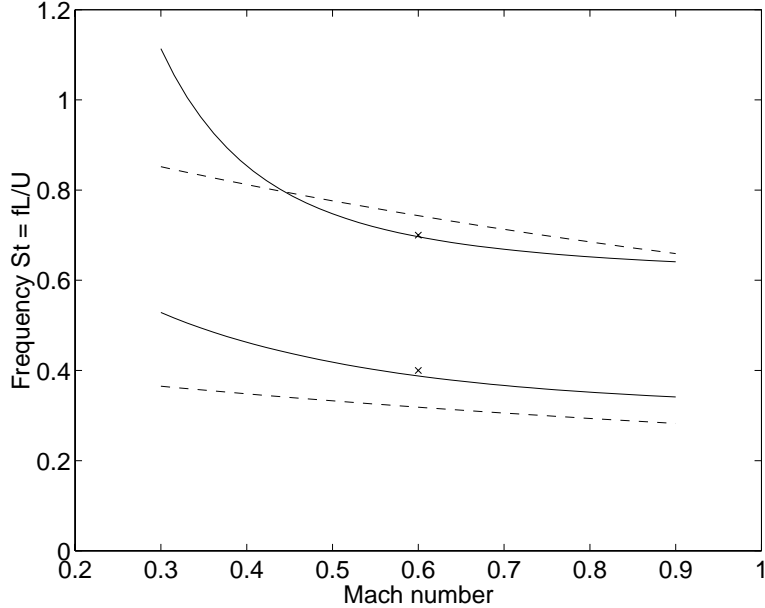


Figure 5.29: Frequencies predicted by Galerkin model as Mach number is varied: $\text{Im}(\lambda/2\pi)$ for unstable eigenvalues λ of 11-mode Galerkin model (—); frequencies measured from DNS (x); and frequencies predicted by Rossiter's equation (---).

on scalar-valued POD modes to that based on vector-valued POD modes. Both methods capture the dynamics well for short time, but the scalar-valued models in particular tend to diverge after a few oscillations. In addition, the scalar-valued modes tend to perform *worse* when more POD modes are retained, in that the long-time behavior is either non-physical or leads to blow-up.

A possible reason why the scalar-valued modes perform poorly for long time is the following. One of the terms appearing in the governing equations is the dilatation $u_x + v_y$. For low-Mach number flows such as this, the dilatation remains small, even though the individual terms u_x and v_y are not small. If scalar-valued modes are used, u and v may drift apart slightly after some time, so that they no longer cancel each other, and the resulting error in dilatation can drive the equations in a non-physical way. When vector-valued modes are used, the dilatation is computed much more accurately, as it is effectively computed for each POD mode, and not from a sum of POD modes for different variables which may drift apart.

In order to use these models for control analysis or synthesis, it is of course necessary to introduce the effects of actuation into the models. The presence of an actuator will presumably change the flow structures, so POD modes need to be taken in the actuated flow, perhaps stacking snapshots from different runs. Precisely how to do this remains an open question, and is a topic for future research, but the present results are promising: since the unactuated flow can be accurately modeled by as few as 3 POD modes, it is likely the actuated flow may also be

described by a model of very low dimension.

Chapter 6

Control Design and Experimental Results

As mentioned in the introduction, previous experiments at controlling cavity oscillations have met with limited success. For instance, a control system might reduce the steady-state amplitude at one resonant frequency, but increase the amplitude at another frequency [Williams & Fabris, 2000b]. The goal of this chapter is to understand these effects using physics-based models, and to use these models both to design control laws, and to understand any performance limitations.

We present a linear model of the cavity, designed around the experiments of Williams & Fabris [2000a]. We then design an (\mathcal{H}_2) optimal controller based on this model, and implement several different control laws on the experiment. The model explains several phenomena observed in the experiments, as well as some performance limitations, discussed in section 6.4.3.

The results described in this chapter represent joint work with Dave Williams at Illinois Institute of Technology, and we mention that the experimental results are very recent, and have not been fully analyzed. Nevertheless, the preliminary results reveal interesting features of the controlled flow, as we discuss in section 6.4.

6.1 Experimental setup

The experimental apparatus described in this section was designed and built by David Williams, Drazen Fabris, and others at the Fluid Dynamics Research Center at Illinois Institute of Technology. Experiments were performed using the 3 ft \times 3 ft subsonic wind tunnel at the United States Air Force Academy in Colorado Springs. We give a brief description of the relevant aspects of the experiment here, and refer to Williams & Fabris [2000a] for further details.

A cavity model 20 in long, 15 in wide, and 4 in deep was installed in the floor of the 3 ft \times 3 ft test section of the wind tunnel. With the cavity in place, the tunnel has a Mach number range of 0.2–0.55. A photograph of the cavity interior is shown in figure 6.1, and a photograph of the assembly from outside the tunnel is shown in figure 6.2.

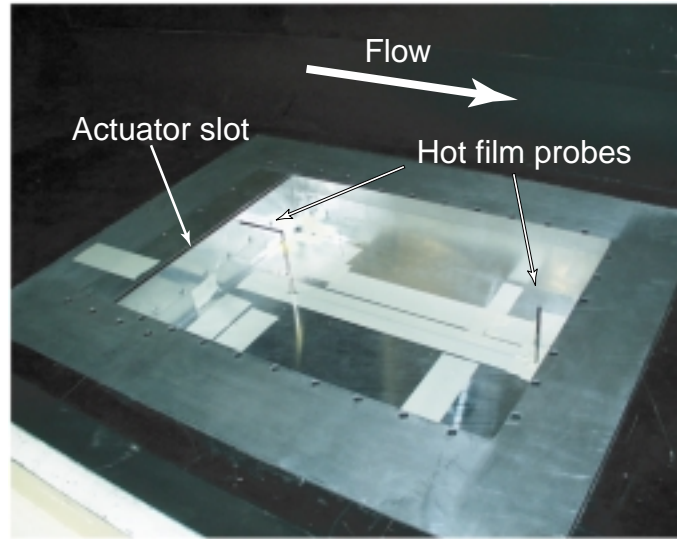


Figure 6.1: Photograph of cavity, from downstream and above.

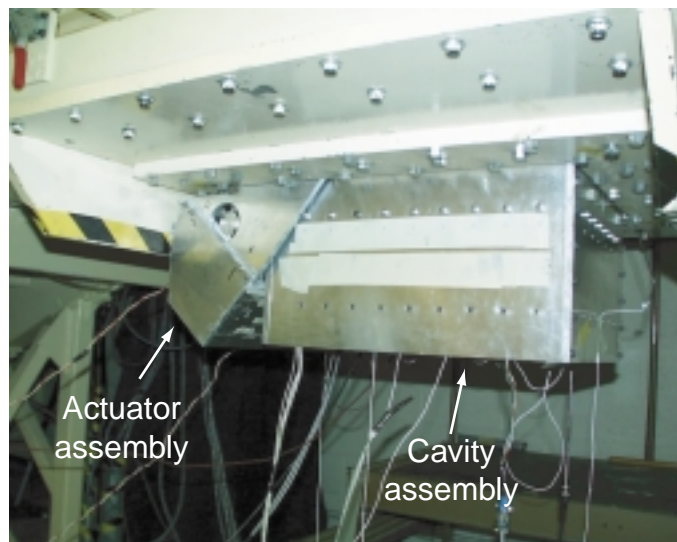


Figure 6.2: Photograph of cavity assembly from outside wind tunnel.

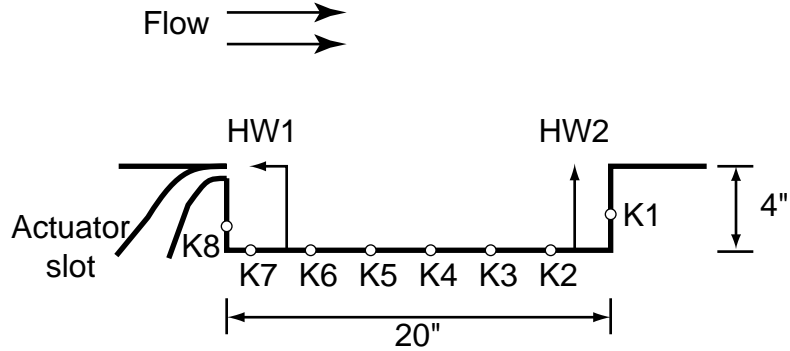


Figure 6.3: Diagram of experimental apparatus (side view). Location of Kulite pressure transducers is indicated by K1–K8, location of hot films indicated by HW1, HW2.

6.1.1 Sensors

The cavity was instrumented with eight Kulite pressure transducers placed along the cavity walls, one on the upstream wall, one on the downstream wall, and six along the floor, approximately equally spaced. The approximate locations are indicated in figure 6.3.

Velocity measurements were obtained using two hot-film sensors placed in the shear layer spanning the cavity, one near the upstream corner ($5/8$ in from the wall), and one near the downstream corner ($1\frac{19}{32}$ in from the wall), both in line with the lip of the cavity, and close to the center in the spanwise direction. These are indicated in figure 6.3, and also appear in the photograph in figure 6.1.

All signals were passed through anti-aliasing filters prior to sampling by a digital data acquisition system. Data were sampled at 6 kHz, typically for 65,536 samples (10.9 sec). The anti-aliasing filters were 4th-order Butterworth bandpass filters, with a pass band of 0.6 Hz–2.2 kHz. (The high-pass filter was necessary to remove the DC offset, and when needed, the DC component was measured using a digital multimeter.)

6.1.2 Actuator

The flow was forced using zero-net-mass blowing through a slot in the upstream wall of the cavity, shown in figure 6.3. The actuator was a pair of 500-Watt 8 in diameter loudspeakers in an enclosed chamber (visible in figure 6.2). The loudspeakers were powered by a 300-watt power amplifier. Though the actuator injects zero net mass through the slot, a nonzero net momentum is induced by spanwise vortices generated by periodically blowing through the slot (the “synthetic jet” effect).

Earlier experiments by Williams & Fabris [2000a] investigated the effects of different orientations of the slot, and found that the actuator was more effective when the slot was oriented in the streamwise direction (as indicated in the figure),

than when it was oriented in the wall-normal direction, or at a 45° angle relative to the free-stream. Note, however, that Shaw [1998] found the opposite trend for a pulsed-blowing actuator (positive net mass injection): forcing in the wall-normal direction was most effective, and forcing in the streamwise direction was least effective.

Though it is possible that the presence of the actuator assembly may introduce other effects into the flow, for instance by changing the structural resonance of the cavity, these extraneous effects are small, as the model has been tested with and without the actuator assembly in place, and the observed results are identical.

6.1.3 Control implementation

Both analog and digital controllers were implemented. The analog controller consisted of a bandpass filter and a phase shifter. The gain and phase could be continuously adjusted, and the frequencies of the passbands could be adjusted in discrete increments.

Digital controllers were implemented using a dSPACE interface board, running on a separate computer from the data acquisition system. For typical controllers we were running, the maximum sample rate of the dSPACE system was about 20 kHz. The digital controllers implemented will be described in sections 6.3 and 6.4.

6.2 Linear model

Our model for the cavity dynamics is based on the familiar Rossiter mechanism described in the introduction: small disturbances to the shear layer excite Kelvin-Helmholtz instabilities, and grow as they convect downstream. When these disturbances impinge on the trailing edge of the cavity, they are scattered into acoustic waves, which propagate upstream and excite further instabilities in the shear layer. This process is depicted in the block diagram shown in figure 6.4, where we have written each component of the mechanism described above as a separate transfer function.

Here, $G(s)$ represents the shear-layer transfer function, i.e., the transfer function from velocity disturbances v_0 at the leading edge to velocity disturbances v_L at the trailing edge. Transfer functions for acoustic scattering, propagation, and receptivity are given by S , A , and R , and in the diagram p_0 and p_L denote pressure disturbances at the leading and trailing edges, respectively. These quantities may be measured from the experiment: v_0 is measured by hot film 1, v_L by hot film 2, and p_L and p_0 by Kulites 2 and 8, respectively (see figure 6.3). Here, we do not use Kulite 1, as this sensor measures substantial pressure fluctuations from the impinging shear layer.

The other transfer functions depicted in figure 6.4 represent the influence of the actuator and controller. The control output u is the voltage to the amplifier, and we use the signal from Kulite 8 as the input y . The controller transfer function (which we choose) is given by C , and the actuator dynamics are described by a transfer function V .

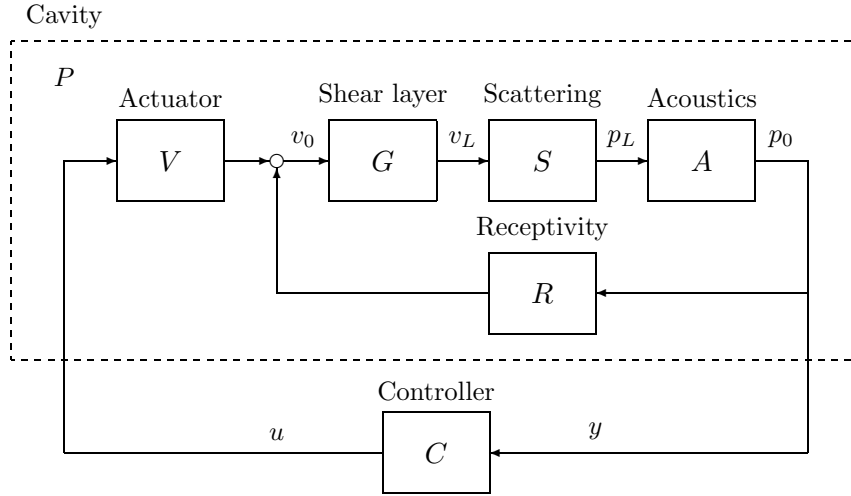


Figure 6.4: Block diagram of cavity model.

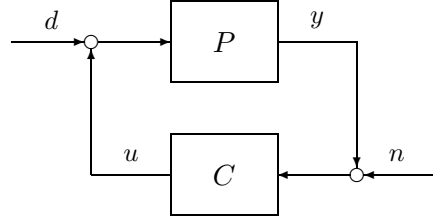


Figure 6.5: Block diagram of cavity model with disturbances.

The overall transfer function P for the cavity is then

$$P = \frac{ASGV}{1 - RASG}. \quad (6.1)$$

For the purposes of studying the dynamical features of this model, we ignore the actuator dynamics, setting $V = 1$. (These actuator dynamics may be measured from the experiment, and once measured, their effects may be inverted out of the control laws we obtain.) Theoretical models for the remaining transfer functions are discussed below.

Figure 6.4 does not include the effects of disturbances. Our model for the way in which disturbances enter is the standard approach shown in figure 6.5, where n is the sensor noise, and d is the process noise. While it might make better physical sense for the process noise to enter after the actuator dynamics V (e.g., as a disturbance to v_0 in figure 6.4), this effect may easily be inverted by changing the frequency content assumed for d .

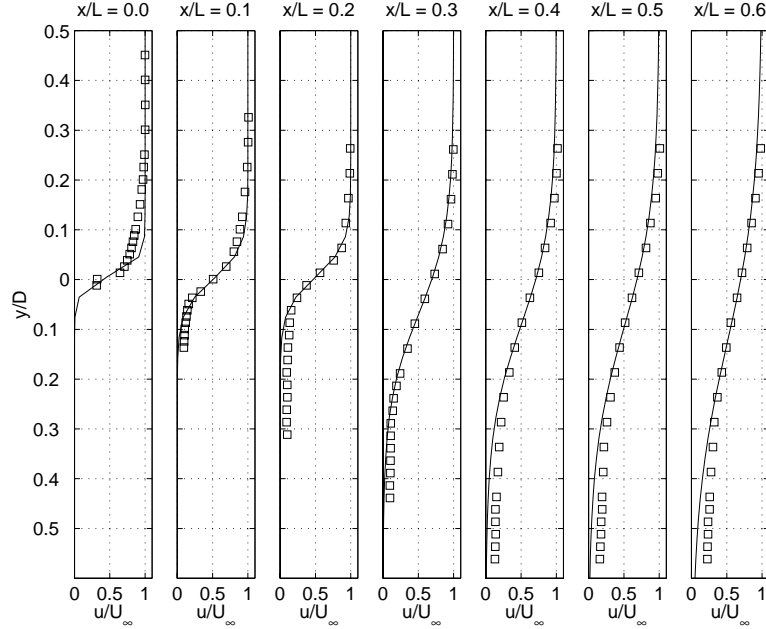


Figure 6.6: Velocity profiles for the cavity shear layer. Hot wire measurements (□) and tanh profiles with same vorticity thickness and deflection (—).

6.2.1 Shear layer

The shear layer transfer function $G(s)$ is determined from linear stability theory. We begin with velocity profiles measured in experiments by Williams & Fabris [2000a], shown in figure 6.6. These profiles are from a run with Mach number $M = 0.35$, in a cavity with aspect ratio $L/D = 5$. Figure 6.6 shows the experimental data along with hyperbolic tangent profiles with the same vorticity thickness. The spreading rate of the shear layer is determined from a linear fit to the data, and used as an input to a linear stability calculation to determine the amplification and phase of shear layer disturbances. We then fit a rational function to the resulting transfer function, and the result is shown in figure 6.7.

6.2.2 Acoustics

The model we use for acoustic propagation in the cavity is shown in figure 6.8. Here, $\tau = L/a$ is a time delay which represents the acoustic lag between the trailing edge and leading edge (here, L is the cavity length and a is the sound speed inside the cavity). An acoustic wave emanating from the downstream corner $x = L$ propagates upstream, and some of it reflects off the upstream wall, propagates downstream, and again reflects off the downstream wall. The reflection coefficient r measures the attenuation in these reflections (e.g., if both reflections are perfect, then $r = 1$; if each reflection reduces the amplitude by 0.5, then $r = 0.25$). This model therefore captures longitudinal modes of acoustic resonance, but ignores

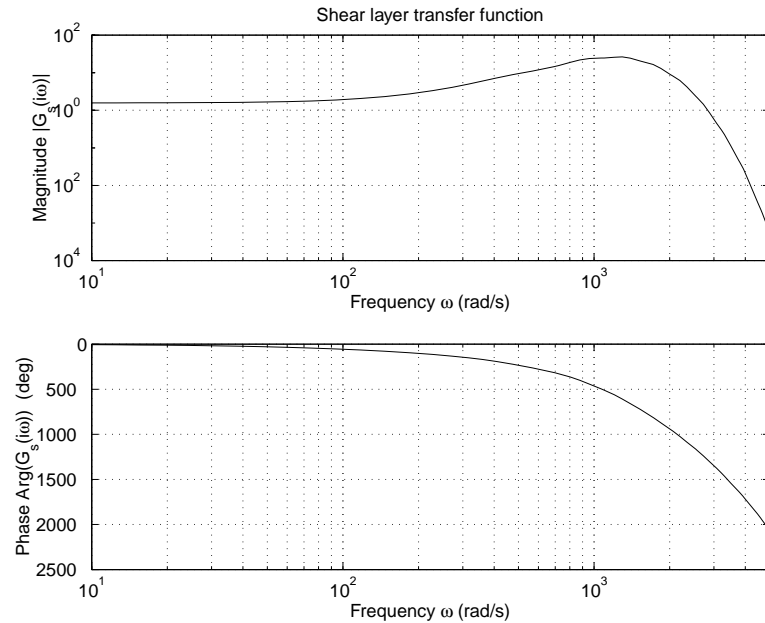


Figure 6.7: Bode plot of shear layer transfer function $G_s(s)$, determined from linear stability theory.

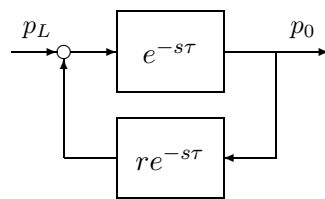


Figure 6.8: Block diagram of transfer function $A(s)$ for cavity acoustics.

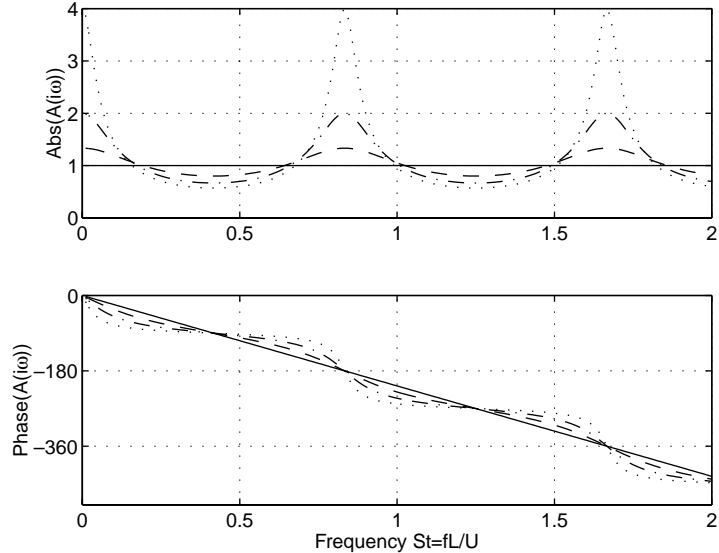


Figure 6.9: Frequency response of acoustic transfer function, for $M = 0.6$. Reflection coefficient $r = 0$ (—); $r = 0.25$ (---); $r = 0.5$ (—·—); $r = 0.75$ (····). Note the linear frequency scale.

depth modes. It is probably reasonable to ignore the depth modes for such a shallow cavity ($L/D = 5$).

The overall transfer function is given by

$$A(s) = \frac{e^{-s\tau}}{1 - re^{-s\tau}}$$

and the Bode plot is shown in figure 6.9, for $M = U/a = 0.6$, and various values of r , ranging from 0 to 0.75. The resonant peaks are clearly apparent, and for this simple model, all of the harmonics are equally strong. Note that these resonant peaks represent the longitudinal acoustic modes of the cavity, and not the Rossiter frequencies. However, when these resonant acoustic frequencies approach the Rossiter frequencies, they may influence the mode selection, determining which Rossiter mode is dominant.

6.2.3 Scattering and Receptivity

The scattering and receptivity effects, which couple vortical and acoustic disturbances at the trailing and leading edge, are the least well understood aspects of the cavity model. Details of these effects have been studied by Crighton [1992] for edge tones, and Kerschen [1996] for cavity flows. However, both of these models describe the scattering by a sharp edge, rather than a corner; scattering at a sharp edge produces a dipole source, as is well known for edge tones, while the acoustic source in the cavity is more closely represented by a monopole, as mentioned in section 3.4.3. Furthermore, these previous scattering models are quite

detailed, employing a Wiener-Hopf factorization (which does not extend easily to corners), and for the purposes of control we are not concerned with detailed flow features, but merely the overall phase and amplitude effects, as a function of frequency. Hence, in this section we consider a crude model, based on Rossiter's semi-empirical formula.

Rossiter's formula, given by equation (3.2), is derived as follows. Consider the total phase variation φ around the cavity feedback loop, given by

$$\varphi = \alpha L - 2\pi\gamma + kL, \quad (6.2)$$

where α is the wavenumber of convected disturbances in the shear layer, k is the wavenumber of acoustic waves, and γ is an empirical constant which represents a phase lag, which Rossiter attributed to receptivity and scattering effects. The wavenumbers may be rewritten in terms of the shear layer convection speed $c_p = -\omega/\alpha$ and the sound speed $a = -\omega/k$. Resonant frequencies occur whenever $\varphi = -2\pi n$, so solving (6.2) for ω , we obtain Rossiter's formula for the resonant frequencies

$$\frac{\omega L}{2\pi U} = \frac{n - \gamma}{M + 1/\kappa}, \quad (6.3)$$

where $\kappa = c_p/U$. Rossiter found that with $\gamma = 0.25$, a good correlation was obtained between the resonant frequencies given this formula and those measured in experiment. As shown by (6.2), the corresponding phase shift from scattering and receptivity is $-\pi/2$, independent of frequency. The analytic transfer function $S(s)$ with this phase shift is simply an integrator, $S(s) = 1/s$. This transfer function has an infinite gain at zero frequency, which is physically unreasonable, but this may be avoided by using a first-order lag instead of a pure integrator:

$$S(s) = \frac{K}{s + a} \quad (6.4)$$

where K is a gain, and a is cutoff frequency which is small compared to all resonant frequencies.

For the present mode, we use (6.4) for the scattering effects, and for the receptivity we take $R = 1$. This is undoubtedly a crude model, but no more crude than Rossiter's model, which has been shown to predict resonant frequencies reasonably well.

6.2.4 Overall cavity model

The overall cavity transfer function P is then formed from equation (6.1), and its poles and zeros are plotted in figure 6.10. (For the time delay, we use a 6th-order Padé approximation to obtain a rational transfer function.) The imaginary part of the poles near the imaginary axis closely match the Rossiter frequencies, as we expect. The first three Rossiter frequencies are unstable, and higher frequencies are stable, since they are damped by the shear layer. The unstable frequencies

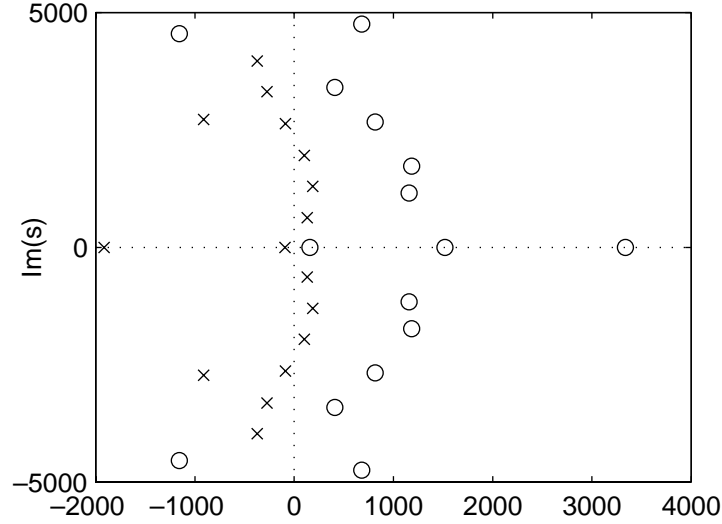


Figure 6.10: Poles (\times) and zeros (\circ) of the cavity transfer function $P(s)$. A 6th-order Pade approximation is used for the time delay. Note unstable poles at the first three Rossiter frequencies.

predicted by our model (at $M = 0.35$) are 100 Hz, 207 Hz, and 312 Hz. In the experiment, only the second and third modes were observed, at frequencies of about 190 Hz and 337 Hz.

6.3 Control design

In this section, we apply standard tools of control design to the cavity model developed above. We use Linear Quadratic Gaussian (LQG) methods to design a controller which is optimal, based on prescribed quadratic cost functions and simple assumptions about the disturbances.

6.3.1 LQG design

We begin with a state-space realization of the cavity model $P(s)$, written in the form

$$\begin{aligned}\dot{x} &= Ax + Bu \\ y &= Cx,\end{aligned}\tag{6.5}$$

where u and y are the inputs and outputs, respectively (see figure 6.4), and x is the state variable. In the LQG design procedure, one first designs a state-feedback controller $u = Kx$ which stabilizes the system, assuming full knowledge of the state, and then one designs an observer to estimate the state based on output measurements y . The controller gains K are found by solving the Linear Quadratic

Regulator (LQR) problem, which gives a linear controller which is optimal, based on a prescribed quadratic cost function. To estimate the state, one uses a Kalman filter, which is a state estimator which is optimal in terms of minimizing the mean square estimation error, based on some assumptions about the disturbances.

The cost function we minimize for the LQR control design is

$$\int_0^\infty (Qy^2 + u^2) dt \quad (6.6)$$

where Q is an arbitrary weight which determines how much to penalize the control input, relative to the output error.

The state estimator provides an estimate \hat{x} of the exact state x (which cannot be measured directly). The estimate is determined by

$$\begin{aligned} \dot{\hat{x}} &= A\hat{x} + Bu + L(y - \hat{y}) \\ \hat{y} &= C\hat{x}, \end{aligned}$$

a system which mimics (6.5), but is forced by the output error $y - \hat{y}$. It is simple to show that the error $\hat{x} - x$ converges to zero as long as the eigenvalues of $A - LC$ are stable. The Kalman filter specifies observer gains L which are optimal, in the sense that the error converges the fastest in the presence of stochastic disturbances d and n (see figure 6.5), assumed to be Gaussian white noise, with specified covariances.

The LQR and optimal estimator problems are easily solved using standard routines in Matlab. The controller and estimator are then combined to give a compensator, which may be written as a transfer function $C(s)$ of the same order as the original plant $P(s)$. This order of the compensator may be reduced using balanced truncation, or more crudely by simply canceling nearby pole-zero pairs.

6.3.2 Stabilizing controller for the cavity model

In the model shown in figure 6.4, it is clear that a controller which merely cancels the natural acoustic feedback in the cavity will stabilize the plant. Any process noise d will still be amplified by the shear layer, but the feedback path which leads to cavity resonance will be broken.

If we neglect the actuator dynamics ($V = 1$), then a stabilizing controller is given by $C = -R^{-1}$. Since we take $R = 1$ in the model, the stabilizing controller is just $C = -1$. Indeed, the optimal control techniques outlined in the previous section give a compensator which closely matches this result.

The optimal controller given by LQG is very high-order (the same dimension as the state, which is high-order, as can be seen by the large number of poles and zeros in figure 6.10), so we perform an elementary model reduction on the compensator $C(s)$, removing (stable) pole-zero pairs which nearly cancel each other. After model reduction, the compensator is sixth-order (reduced from 16), and its transfer function is shown in figure 6.11. Note that, in the frequency range where the model is valid (less than about 3000 rad/sec), the compensator closely resembles

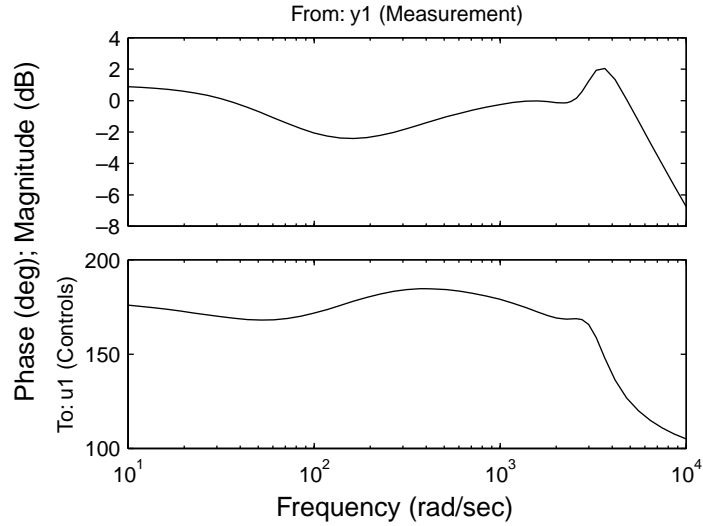


Figure 6.11: Bode plot of controller transfer function $C(s)$ (reduced-order controller). For reference, the unstable frequencies occurred at $\omega = 628, 1301$, and 1960 rad/s.

the function -1 (180° phase, with a gain of 0 dB), as expected.

The poles of the closed-loop system (with control) are shown in figure 6.12. Without the model reduction step, LQG guarantees the closed-loop system will be stable, but figure 6.12 demonstrates that the closed loop system is stable (all poles in the left half-plane) even with the reduced-order compensator.

For such a simple model, where a stabilizing control law is obvious, we really do not require the elaborate machinery of LQG design. Our methodology is nevertheless useful, as enhancements to the model (for instance, measuring transfer functions directly from an experiment) will lead to more complex controllers. Furthermore, once we have a model of the physics, we may analyze limitations of achievable performance, as we discuss in the next section.

6.4 Experimental results

Here, we present some recent results from the experiment described in section 6.1, discussing results using both analog and digital controllers. All of the results are for a run with $M = 0.34$, at which only a single mode of cavity oscillations was present.

6.4.1 Analog controller

The analog controller consisted of an Ithaco filter, a 4th-order Butterworth band-pass filter whose passbands could be adjusted in discrete increments, and a phase

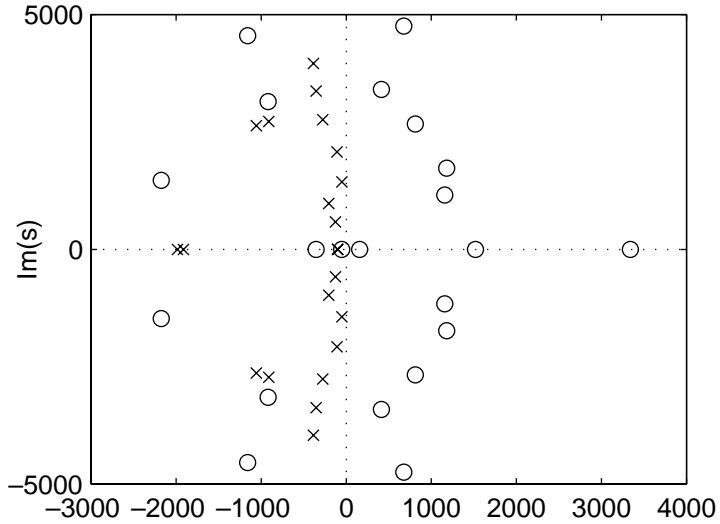


Figure 6.12: Poles and zeros of closed-loop transfer function, with reduced-order controller. Rossiter modes are stabilized.

| Name | Order | Passband |
|----------|-------|------------|
| Filter 1 | 2 | 320–360 Hz |
| Filter 2 | 2 | 290–390 Hz |
| Filter 3 | 2 | 215–465 Hz |

Table 6.1: Parameters of digital Butterworth filters used.

shifter, which could be fine-tuned manually. The transfer function of the analog controller is shown in figure 6.13, where the passband was set to 300–350 Hz.

Figure 6.14 shows the results of the experiment, with and without control. For the case shown, the gain and phase were manually tuned for the greatest suppression. When control is switched on, the resonant frequency at 337 Hz is attenuated significantly, but a new peak appears at 434 Hz. The smaller peak at 674 Hz is the first harmonic of the fundamental cavity frequency, and it too is attenuated with control.

6.4.2 Digital controller

The digital controllers implemented were also bandpass filters, and we tried several digital Butterworth filters of different orders and passbands. The orders and passbands for the filters used here are shown in table 6.1, and the transfer functions are shown in figure 6.15.

Figure 6.16 shows the results of the closed-loop experiments with the different filters. In this figure, the gain and phase was tuned for the best suppression. The narrow band filter showed very little attenuation, and the broadband filters better attenuated the main cavity frequency, but a higher frequency peak appears, as it

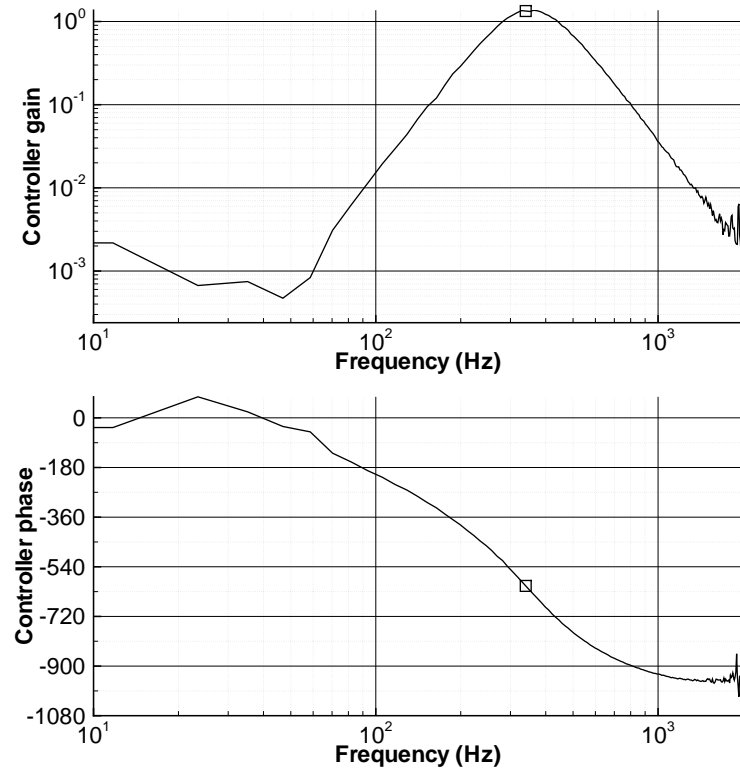


Figure 6.13: Bode plot of analog controller. Frequency of cavity oscillations indicated by (□).

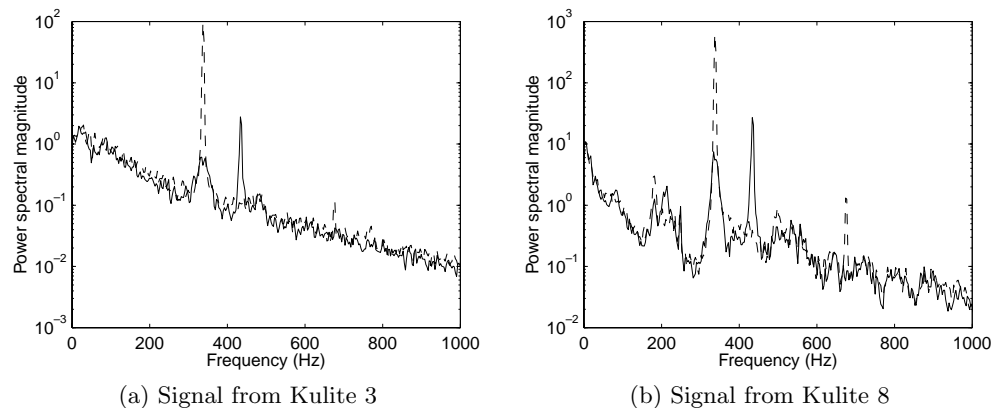


Figure 6.14: Power spectrum from two pressure sensors, for analog controller: control off (----); control on (—).

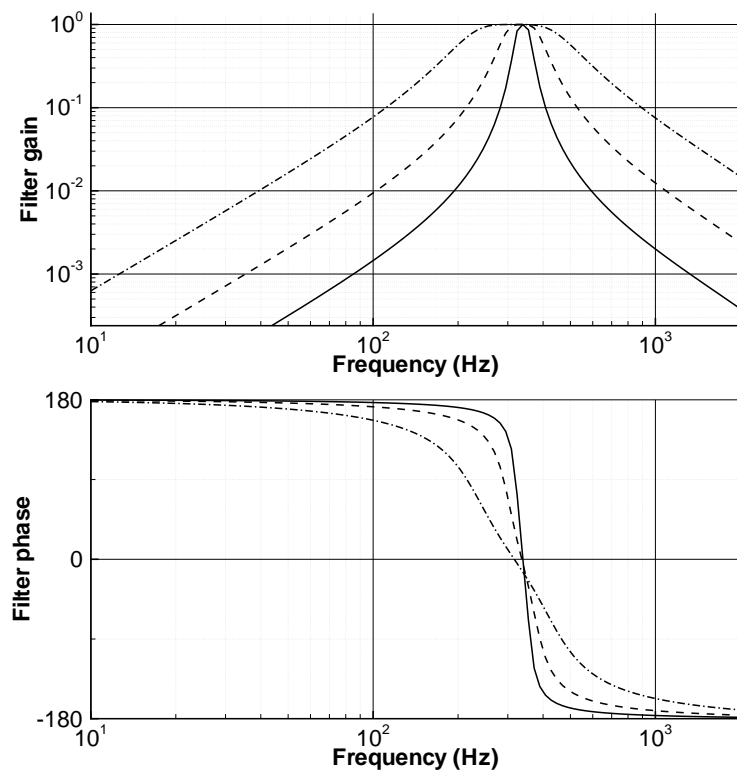


Figure 6.15: Bode plot of filters used in digital controllers: filter 1 (—); filter 2 (---); filter 3 (—·—).

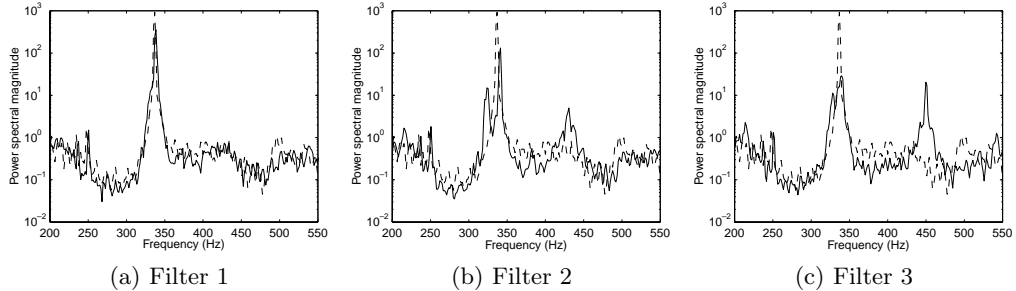


Figure 6.16: Power spectrum with 3 different digital filters, tuning gain and phase manually for best suppression: control off (---); control on (—).

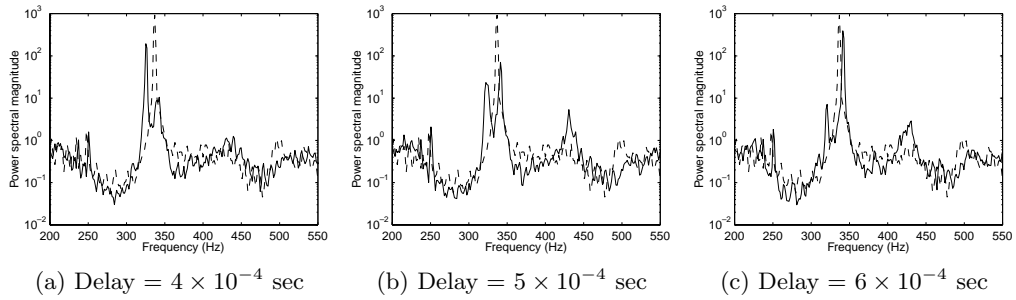


Figure 6.17: Power spectra with digital controllers, showing sidebands: control off (---); control on, using filter 2 (—).

did with the analog controllers. The frequency of this peak shifts with different controllers: with filter 2, the peak is at 430 Hz; with filter 3, 449 Hz.

Note that, especially evident in figure 6.16b, the main cavity frequency is sometimes split into two sidebands when the control is turned on. This effect is explored further in figure 6.17, where filter 2 was used, and the time delay was adjusted. The main resonant frequency at 337 Hz is almost completely attenuated, but sidebands appear very close in frequency, at about 320 Hz and 341 Hz. As the time delay is changed, the relative strength of the sidebands changes, and the frequency changes slightly—the lower frequency shifts from 320 to 325 Hz in figures (a)–(c). We discuss these sidebands further in the next section.

6.4.3 Performance limitations

The experimental results of the previous section are somewhat discouraging: whenever significant attenuation of the main cavity frequency was achieved, new oscillations appeared at different frequencies. These new peaks of the closed-loop system are of two types: a broad peak occurred at a frequency quite different from the main cavity frequency (e.g., at about 430 Hz in figure 6.17); in addition, narrow

peaks very close to the original cavity frequency occurred, which we refer to as sidebands.

A similar appearance of sidebands has been observed in recent experiments on control of combustion instabilities, discussed by Banaszuk et al. [2001]. These combustion instabilities are similar to cavity instabilities in many ways: both systems exhibit self-sustained oscillations caused by flow-acoustic interactions. Time delays are inherent in both systems, because of the nature of the acoustic feedback. In both systems, the amplitude of oscillations is determined by a nonlinear saturation mechanism (though this mechanism is much better understood in the combustion problem).

The appearance of these sidebands may be understood from a purely linear point of view, employing the well-known “area rule,” which establishes performance limitations for feedback systems. The area rule determines constraints on the *sensitivity function*

$$S = \frac{1}{1 - PC} \quad (6.7)$$

for linear systems of the form 6.5. The area rule applies to systems whose relative degree is at least 2 (relative degree is the degree of the denominator of a transfer function minus the degree of the numerator), and states that

$$\int_0^\infty \log_{10} |S(i\omega)| d\omega = \pi \log_{10} e \sum \operatorname{Re} p_i, \quad (6.8)$$

where p_i are the unstable poles of the transfer function PC . Thus, if disturbances are attenuated over some frequency range, they must be amplified over some other frequency range, and if the plant is unstable (so that there are unstable poles p_i) then this effect is exacerbated. Furthermore, this effect is particularly apparent for narrow bandwidth controllers. As $PC \rightarrow 0$, $S \rightarrow 1$, so $\log_{10} |S| \rightarrow 0$. Thus, all of the disturbance amplification must occur within the narrow bandwidth of the controller, and the more narrow the bandwidth, the greater the amount of the disturbance amplification.

It is likely that this effect explains the sidebands evident in figure 6.17. Though the models developed in section 6.2 do not represent the experiment closely enough to verify this effect quantitatively (our models even predict more than one frequency of oscillation, while the experiment shows only one mode), more refined models may well be able to explain these phenomena. It is likely that more accurate models may be obtained by using experiments to identify the individual transfer functions represented in figure 6.4, but we leave this for future work.

Chapter 7

Conclusions

This chapter contains a summary of the contributions of this thesis, along with some suggestions for future study.

7.1 Summary

We have performed an extensive set of Direct Numerical Simulations (DNS) for the two-dimensional, compressible flow past a rectangular cavity. These simulations reveal two distinct modes of self-sustained oscillation: a shear-layer mode, which is the mode originally described by Rossiter [1964], and a wake mode, which was first classified by Gharib & Roshko [1987]. In wake mode, the frequency of oscillation is independent of Mach number, indicating that acoustics no longer play an important role in the underlying feedback mechanism that leads to self-sustained oscillations. Transition to wake mode appears to occur when the amplitude of oscillations exceeds a certain threshold. In wake mode, there is significant backflow in the cavity, and it is possible that this creates a region of absolute instability in the shear layer, which may provide the feedback mechanism necessary for self-sustained oscillations.

The technique of Proper Orthogonal Decomposition (POD) and Galerkin projection is well known, and has been used to study a number of incompressible flows [Aubry et al., 1988]. We have extended this technique to compressible flows. Using a simplified form of the Navier-Stokes equations, valid for cold flows at moderate Mach number, we have obtained Galerkin projections which are quadratic, and are easily computed. We have introduced a family of inner products which may be used for computing vector-valued POD modes for compressible flows, where both the kinematic and thermodynamic variables contribute to the total energy.

We have applied these model-reduction techniques to the flow past a cavity, using data from our numerical simulations to obtain POD modes. We compare models obtained from separate sets of scalar-valued POD modes, and a single set of vector-valued POD modes, obtaining reduced-order systems with between 2 and 60 states. All of the models capture the dynamics well for short times (a few periods of the oscillation), and in general the models based on scalar-valued modes diverge for long times, and are even unstable, while the models using vector-valued modes

have much better long-time behavior.

Finally, we have described a conceptual modeling approach, where we model the individual components of the cavity physics separately. This approach leads to linear models to which standard tools from control theory apply, and we use the Linear Quadratic Gaussian (LQG) technique to design a controller which stabilizes cavity oscillations.

7.2 Suggestions for future work

For the POD/Galerkin models developed in this thesis to be useful for bifurcation analysis, the models must first be validated over the parameter range considered. To obtain low-order models valid over a range of parameters, one might use POD modes obtained from an ensemble of snapshots taken from several different runs, and validate the resulting models by comparing to direct numerical simulations at different parameter values. The resulting low-order models could then be used to study bifurcations—for instance, the onset of cavity oscillations qualitatively resembles a supercritical Hopf bifurcation, and the POD/Galerkin models could be used to provide a more quantitative understanding of this transition process.

Similarly, for these models to be useful for control analysis or synthesis, they must include the effects of actuation. One may introduce actuator effects using, for instance, body force terms in the equations of motion, but the resulting low-order models also need to be validated in the presence of actuation.

Finally, the experimental results presented in the previous chapter are very recent, and need to be studied in greater detail. In particular, the experimental results may be used to identify the different components of the linear models described in the last chapter, obtaining transfer functions directly from experimental data. The resulting models should represent the experiment much more faithfully than the simplified analytical models presented, and could be used to explain the effects observed, leading to a better understanding of the flow physics, and ultimately guiding the design of more effective control techniques.

Bibliography

ABRAHAM, R., MARSDEN, J. E., & RATIU, T. S. [1988] *Manifolds, Tensor Analysis, and Applications*. No. 75 in Applied Mathematical Sciences. Springer-Verlag, second edn.

AHUJA, K. K. & MENDOZA, J. [1995] Effects of cavity dimensions, boundary layer, and temperature on cavity noise with emphasis on benchmark data to validate computational aeroacoustic codes. Final Report Contract NAS1-19061, Task 13, NASA Contractor Report.

AUBRY, N., HOLMES, P., LUMLEY, J. L., & STONE, E. [1988] The dynamics of coherent structures in the wall region of a turbulent boundary layer. *J. Fluid Mech.* **192**, 115–173.

BANASZUK, A., MEHTA, P. G., JACOBSON, C. A., & KHIBNIK, A. I. [2001] Limits of achievable performance of controlled combustion processes. *IEEE Trans. Automat. Contr.* (submitted).

BATCHELOR, G. K. [1967] *An Introduction to Fluid Dynamics*. Cambridge University Press.

BLAKE, W. K. & POWELL, A. [1986] The development of contemporary views of flow-tone generation. In *Recent Advances in Aeroacoustics*, pp. 247–345. Springer-Verlag.

BROWN, G. B. [1937] The vortex motion causing edge tones. *Proc. Phys. Soc. (London)* **49**, 493–507.

BROWN, G. L. & ROSHKO, A. [1974] On density effects and large structure in turbulent mixing layers. *J. Fluid Mech.* **64**, 775–816.

CAIN, A. B., BOWER, W. W., MCCOTTER, F., & ROMER, W. W. [1996] Modeling and prediction of weapons bay acoustic amplitude and frequency. Tech. rep., VEDA Inc.

CATTAFESTA, III, L. N., GARG, S., CHOUDHARI, M., & LI, F. [1997] Active control of flow-induced cavity resonance. AIAA Paper 97-1804.

CATTAFESTA, III, L. N., GARG, S., KEGERISE, M. S., & JONES, G. S. [1998] Experiments on compressible flow-induced cavity oscillations. AIAA Paper 98-2912.

CATTAFESTA, III, L. N., SHUKLA, D., GARG, S., & ROSS, J. A. [1999] Development of an adaptive weapons-bay suppression system. AIAA Paper 99-1901.

CODDINGTON, E. A. & LEVINSON, N. [1955] *Theory of Ordinary Differential Equations*. McGraw-Hill.

COLONIUS, T. [2001] An overview of simulation, modeling, and active control of flow/acoustic resonance in open cavities. AIAA Paper 2001-0076.

COLONIUS, T., LELE, S. K., & MOIN, P. [1993] Boundary conditions for direct computation of aerodynamic sound. *AIAA J.* **31** (9), 1574–1582.

COLONIUS, T., LELE, S. K., & MOIN, P. [1997] Sound generation in a mixing layer. *J. Fluid Mech.* **330**, 375–409.

COLONIUS, T., MOHSENI, K., FREUND, J. B., LELE, S. K., & MOIN, P. [1998] Evaluation of noise radiation mechanisms in a turbulent jet. Stanford University, Center for Turbulence Research, Proceedings of the Summer Program.

CRIGHTON, D. G. [1975] Basic principles of aerodynamic noise generation. *Prog. Aerosp. Sci.* **16** (1), 31–96.

CRIGHTON, D. G. [1992] The jet edge-tone feedback cycle; linear theory for the operating stages. *J. Fluid Mech.* **234**, 361–391.

CRIGHTON, D. G. & GASTER, M. [1976] Stability of slowly diverging jet flow. *J. Fluid Mech.* **77**, 397–413.

DRAZIN, P. G. & REID, W. H. [1981] *Hydrodynamic Stability*. Cambridge University Press.

FLETCHER, C. A. J. [1991] *Computational Techniques for Fluid Dynamics*, vol. 1. Springer-Verlag, second edn.

FOX, J. [1965] Flow regimes in transverse rectangular cavities. In *Proceedings of the 1965 Heat Transfer and Fluid Mechanics Institute*. Stanford University Press.

FOX, J. [1968] A criterion for the transition between flow regimes in turbulent cavity flow. *AIAA J.* **4** (2), 364–365.

FREUND, J. B. [1997] Proposed inflow/outflow boundary condition for direct computation of aerodynamic sound. *AIAA J.* **35** (4), 740–742.

GHARIB, M. [1987] Response of the cavity shear layer oscillations to external forcing. *AIAA J.* **25** (1), 43–47.

GHARIB, M. & ROSHKO, A. [1987] The effect of flow oscillations on cavity drag. *J. Fluid Mech.* **177**, 501–530.

GROSCH, C. E. & SALWEN, H. [1978] The continuous spectrum of the Orr-Sommerfeld equation. Part 1. The spectrum and the eigenfunctions. *J. Fluid Mech.* **87**, 33–54.

VON HELMHOLTZ, H. [1868] On discontinuous movements of fluids. *Phil. Mag.* **36**, 337–346.

HOLMES, P., LUMLEY, J. L., & BERKOOZ, G. [1996] *Turbulence, Coherent Structures, Dynamical Systems and Symmetry*. Cambridge University Press.

HOWARD, L. N. [1961] Note on a paper of John W. Miles. *J. Fluid Mech.* **10**, 509–512.

HOWARD, L. N. [1964] The number of unstable modes in hydrodynamic stability problems. *J. Méc.* **3** (4), 433–443.

HOWE, M. S. [1997] Edge, cavity and aperture tones at very low mach numbers. *J. Fluid Mech.* **330**, 61–84.

HUERRE, P. & MONKEWITZ, P. A. [1985] Absolute and convective instabilities in free shear layers. *J. Fluid Mech.* **159**, 151–168.

HUERRE, P. & MONKEWITZ, P. A. [1990] Local and global instabilities in spatially developing flows. *Ann. Rev. Fluid Mech.* **22**, 473–537.

KELVIN, LORD [1871] Hydrokinetic solutions and observations. *Phil. Mag.* **42**, 362–377.

KERSCHEN, E. J. [1996] The acoustic field generated by interaction of a shear-layer instability with the downstream lip of a cavity. Tech. rep., Flow Dynamics Research, Tucson, AZ.

KHALIL, H. K. [1996] *Nonlinear Systems*. Prentice-Hall, second edn.

KHIBNIK, A. I., NARAYANAN, S., JACOBSON, C. A., & LUST, K. [1998] Analysis of low dimensional dynamics of flow separation. *Notes in Computational Fluid Dynamics submitted*.

KNISELY, C. & ROCKWELL, D. [1982] Self-sustained low-frequency components in an impinging shear layer. *J. Fluid Mech.* **116**, 157–186.

KRIESELS, P. C., PETERS, M. C. A. M., HIRSCHBERG, A., WIJNANDS, P. J., IAFRATI, A., RICCARDI, G., PIVA, R., & BRUGGEMAN, J. C. [1995] High amplitude vortex-induced pulsations in a gas transport system. *J. Sound Vib.* **184** (2), 343–368.

KRISHNAMURTY, K. [1956] Sound radiation from surface cutouts in high speed flow. Ph.D. thesis, California Institute of Technology.

KROTHAPALLI, A. [2001] Personal communication.

LELE, S. K. [1992] Compact finite difference schemes with spectral-like resolution. *J. Comput. Phys.* **103** (1), 16–42.

LOÈVE, M. [1978] *Probability Theory II*. No. 46 in Graduate Texts in Mathematics. Springer-Verlag, fourth edn.

LUENBERGER, D. G. [1997] *Optimization by Vector Space Methods*. John Wiley and Sons.

LUMLEY, J. L. [1970] *Stochastic Tools in Turbulence*. Academic Press.

MICHALKE, A. [1984] Survey on jet instability theory. *Prog. Aerosp. Sci.* **21**, 159–199.

MONKEWITZ, P. A. & NGUYEN, L. N. [1987] Absolute instability in the near-wake of two-dimensional bluff bodies. *J. Fluids Struct.* **1**, 165–184.

MORRIS, P. J., GIRIDHARAN, M. G., & LILLEY, G. M. [1990] On the turbulent mixing of compressible free shear layers. *Proc. R. Soc. Lond. A* **431**, 219–243.

POINSOT, T. & LELE, S. K. [1992] Boundary conditions for direct simulation of compressible viscous flows. *J. Comput. Phys.* **101**, 104–129.

POWELL, A. [1953] On edge tones and associated phenomena. *Acustica* **3**, 233–243.

POWELL, A. [1961] On the edgetone. *J. Acoust. Soc. Amer.* **33** (4), 395–409.

RAYLEIGH, LORD [1880] On the stability, or instability, of certain fluid motions. *Proc. London Math. Soc.* **11**, 57–70. Also in *Scientific Papers*, Cambridge, 1899.

RAYLEIGH, LORD [1945] *The Theory of Sound*, vol. 2. Dover.

REMPFER, D. [2000] On low-dimensional Galerkin models for fluid flow. *Theor. Comput. Fluid Dyn.* **14** (2), 75–88.

RIESZ, F. & SZ.-NAGY, B. [1990] *Functional Analysis*. Dover.

ROCKWELL, D. & NAUDASCHER, E. [1978] Review—self-sustaining oscillations of flow past cavities. *J. Fluids Eng.* **100**, 152–165.

ROCKWELL, D. & SCHACHENMANN, A. [1982] Self-generation of organized waves in an impinging turbulent jet at low Mach number. *J. Fluid Mech.* **117**, 425–441.

ROSHKO, A. [1955] Some measurements of flow in a rectangular cutout. NACA TN 3488.

ROSSITER, J. E. [1964] Wind-tunnel experiments on the flow over rectangular cavities at subsonic and transonic speeds. Aeronautical Research Council Reports and Memoranda, No. 3438.

ROWLEY, C. W. & COLONIUS, T. [2000] Discretely nonreflecting boundary conditions for linear hyperbolic systems. *J. Comput. Phys.* **157**, 500–538.

ROWLEY, C. W. & MARSDEN, J. E. [2000] Reconstruction equations and the Karhunen-Loëve expansion for systems with symmetry. *Phys. D* **142**, 1–19.

SALWEN, H. & GROSCH, C. E. [1981] The continuous spectrum of the Orr-Sommerfeld equation. Part 2. Eigenfunction expansions. *J. Fluid Mech.* **104**, 445–465.

SANDHAM, N. D. & REYNOLDS, W. C. [1989] A numerical investigation of the compressible mixing layer. Tech. Rep. TF-45, Stanford University.

SARNO, R. L. & FRANKE, M. E. [1994] Suppression of flow-induced pressure oscillations in cavities. *J. Aircraft* **31** (1), 90–96.

SAROHIA, V. [1975] Experimental and analytical investigation of oscillations in flows over cavities. Ph.D. thesis, California Institute of Technology.

SAROHIA, V. & MASSIER, P. F. [1977] Control of cavity noise. *J. Aircraft* **14** (9), 833–837.

SATTINGER, D. H. [1967] On the Rayleigh problem in hydrodynamic stability. *SIAM J. Appl. Math.* **15** (2), 419–425.

SHAW, L. [1998] Active control for cavity acoustics. AIAA Paper 98-2347.

SHAW, L. & NORTHCRAFT, S. [1999] Closed loop active control for cavity acoustics. AIAA Paper 99-1902.

SIROVICH, L. [1987] Turbulence and the dynamics of coherent structures, parts I–III. *Q. Appl. Math.* **XLV** (3), 561–590.

STAKGOLD, I. [2000] *Boundary Value Problems of Mathematical Physics*. No. 29 in Classics in Applied Mathematics. SIAM.

STANEK, M. J., RAMAN, G., KIBENS, V., ROSS, J. A., ODEDRA, J., & PETO, J. W. [2000] Control of cavity resonance through very high frequency forcing. AIAA Paper 2000-1905.

TAM, C. K. W. & BLOCK, P. J. W. [1978] On the tones and pressure oscillations induced by flow over rectangular cavities. *J. Fluid Mech.* **89** (2), 373–399.

TAM, C. K. W. & MORRIS, P. J. [1980] The radiation of sound by the instability waves of a compressible plane turbulent shear layer. *J. Fluid Mech.* **98** (2), 349–381.

THOMPSON, K. W. [1987] Time dependent boundary conditions for hyperbolic systems. *J. Comput. Phys.* **68**, 1–24.

UKEILEY, L., SEINER, J., SINHA, N., & ARUNAJATESAN, S. [2000] Low-dimensional description of cavity flows. *Bull. Amer. Phys. Soc.* **45** (9), 138.

VAKILI, A. D. & GAUTHER, C. [1991] Control of cavity flow by upstream mass injection. AIAA Paper 91-1645.

WHITE, F. M. [1991] *Viscous Fluid Flow*. McGraw-Hill, second edn.

WILLIAMS, D. R. & FABRIS, D. [2000a] Closed-loop control in cavities with unsteady bleed forcing. AIAA Paper 2000-0470.

WILLIAMS, D. R. & FABRIS, D. [2000b] Experiments on controlling multiple acoustic modes in cavities. AIAA Paper 2000-1903.

WOOLLEY, J. P. & KARAMCHETI, K. [1974] Role of jet stability in edgetone generation. *AIAA J.* **12**, 1456–1458.